



PORE-NETWORK MODELING OF REACTIVE TRANSPORT AND MINERAL
DISSOLUTION IN POROUS MEDIA

Bárbara de Farias Esteves

Tese de Doutorado apresentada ao Programa de Pós-graduação em Engenharia Química, COPPE, da Universidade Federal do Rio de Janeiro, como parte dos requisitos necessários à obtenção do título de Doutor em Engenharia Química.

Orientadores: Paulo Laranjeira da Cunha
Lage
Paulo Couto
Anthony Robert Kavscek

Rio de Janeiro
Março de 2021

PORE-NETWORK MODELING OF REACTIVE TRANSPORT AND MINERAL
DISSOLUTION IN POROUS MEDIA

Bárbara de Farias Esteves

TESE SUBMETIDA AO CORPO DOCENTE DO INSTITUTO ALBERTO LUIZ
COIMBRA DE PÓS-GRADUAÇÃO E PESQUISA DE ENGENHARIA DA
UNIVERSIDADE FEDERAL DO RIO DE JANEIRO COMO PARTE DOS
REQUISITOS NECESSÁRIOS PARA A OBTENÇÃO DO GRAU DE DOUTOR
EM CIÊNCIAS EM ENGENHARIA QUÍMICA.

Orientadores: Paulo Laranjeira da Cunha Lage

Paulo Couto

Anthony Robert Kovscek

Aprovada por: Prof. Paulo Laranjeira da Cunha Lage

Prof. Paulo Couto

Prof. Anthony Robert Kovscek

Prof. Argimiro Resende Secchi

Prof. Luiz Fernando Lopes Rodrigues Silva

Prof. Amir Raouf

RIO DE JANEIRO, RJ – BRASIL

MARÇO DE 2021

Esteves, Bárbara de Farias

Pore-network modeling of reactive transport and mineral dissolution in porous media/Bárbara de Farias

Esteves. – Rio de Janeiro: UFRJ/COPPE, 2021.

XXV, 130 p.: il.; 29,7cm.

Orientadores: Paulo Laranjeira da Cunha Lage

Paulo Couto

Anthony Robert Kavscek

Tese (doutorado) – UFRJ/COPPE/Programa de Engenharia Química, 2021.

Referências Bibliográficas: p. 114 – 122.

1. Pore-network modeling. 2. Reactive transport.
3. Mineral dissolution. 4. Pore-scale modeling. 5.
Pore-merging. I. Lage, Paulo Laranjeira da Cunha
et al. II. Universidade Federal do Rio de Janeiro, COPPE,
Programa de Engenharia Química. III. Título.

Acknowledgments

I would like to express my most sincere gratitude to my advisors, Professors Paulo Lage, Paulo Couto, and Anthony Kovscek. I will always admire all the guidance, support, and patience that I received from Prof. Paulo Lage. His strong knowledge and continuous support enabled me to conclude this wonderful journey that was my PhD study. Prof. Paulo Couto taught me the concepts of Reservoir Engineering and how I could use my Chemical Engineering knowledge to understand practical aspects of multiple interesting problems in the oil industry. Prof. Anthony Kovscek gave me the opportunity to be a part of his research group and be one of his lucky students. He is a unique advisor and human being, for whom I have the highest level of admiration. His endless efforts in keeping his students active, united, and motivated in developing high quality research, inspired me to always do my best.

I would like to acknowledge Professors Argimiro R. Secchi, Luiz Fernando L. R. Silva, and Amir Raouf for kindly agreeing to participate in my PhD defense as committee members. I deeply appreciate all their comments and suggestions regarding my dissertation.

I gratefully acknowledge all the support that I received from the PEQ and ERE staffs. I am especially grateful to Vera, Luciana, Diane, Joanna, Sandy, Arlene, and LyriSSa who have always been so helpful and friendly. They made this journey much easier and supported me throughout my study.

I am also very thankful to my friends and colleagues that spent their time teaching me about tools and methodologies that I needed for my research. I would like to thank Mateus, Ataíde, Neyher, JABS, Débora, Tahyná, Fernandinha, Maira, and Luiz who have been always available to help.

I would like to thank SUPRI-A and LRAP research groups for providing me

with the best academic environments for the development of this research.

I express my gratitude to all SUPRI-A members, especially my Microfluidics group partner Negar Nazari, and former students Salem Aldousary and Wonjin Yun. I feel so lucky that I had the opportunity to be a part of this great group and to meet such special people and friends. I will miss you A LOT!

I would like to thank Coordenação de Aperfeiçoamento de Pessoal de Nível Superior (CAPES), Conselho Nacional de Desenvolvimento Científico e Tecnológico (CNPq), Shell, and Stanford Center for Carbon Storage (SCCS) for the financial support.

I want to thank Gerson and Nina, my friends and yoga instructors, for sharing their experience in the last year through incredible online yoga classes and providing me a break during a workday.

Finally, I want to thank my family, who have over the years supported and guided me in my endeavors. My parents have devoted their life to provide the best conditions for my brother and I to grow. Who I am today reflects their hard work and their priority for our education. My mom and my brother lived with me through every steps of this journey, and my dad was always present in my heart and in my mind. Ricardo, my husband, made his dream of studying at Stanford University to be one of my most enriching life experiences. More than the best life partner, he has shown to be the best pandemic partner one could ever have! Our partnership and union just got stronger, and my love and admiration for him just got bigger.

Resumo da Tese apresentada à COPPE/UFRJ como parte dos requisitos necessários para a obtenção do grau de Doutor em Ciências (D.Sc.)

MODELAGEM DO TRANSPORTE REATIVO E DA DISSOLUÇÃO MINERAL
EM MEIOS POROSOS USANDO REDES DE POROS

Bárbara de Farias Esteves

Março/2021

Orientadores: Paulo Laranjeira da Cunha Lage

Paulo Couto

Anthony Robert Kavscek

Programa: Engenharia Química

Esta tese apresenta uma nova abordagem usando redes de poros com evolução topológica para modelar o transporte reativo monofásico e a dissolução mineral em meios porosos. A abordagem acopla o transporte e a cinética da reação usando um modelo de rede de poros que implementa uma única reação química heterogênea que descreve a dissolução da calcita por soluções ácidas. A geometria da rede é atualizada com base no processo de dissolução que ocorre na superfície do mineral. O campo de velocidade também é atualizado devido a esses novos tamanhos de poros e gargantas. Neste trabalho, uma nova metodologia para descrever a junção de poros e gargantas resultante da dissolução mineral é introduzida para garantir a conservação das principais variáveis de interesse durante o processo de junção. As áreas reativas e as condutâncias são acuradamente conservadas através da definição de fatores de correção e propriedades efetivas. Uma ampla gama de redes de poros é usada para estudar o problema do transporte reativo. Os principais resultados incluem o mapeamento e a exploração de diferentes regimes de dissolução através de curvas de evolução da porosidade-permeabilidade, perfis de concentração de ácido na rede de poros, e o uso de critérios estatísticos para diferenciar regimes.

Abstract of Thesis presented to COPPE/UFRJ as a partial fulfillment of the requirements for the degree of Doctor of Science (D.Sc.)

PORE-NETWORK MODELING OF REACTIVE TRANSPORT AND MINERAL DISSOLUTION IN POROUS MEDIA

Bárbara de Farias Esteves

March/2021

Advisors: Paulo Laranjeira da Cunha Lage

Paulo Couto

Anthony Robert Kovscek

Department: Chemical Engineering

This thesis proposes and demonstrates a new pore-network modeling approach including topology evolution to simulate single-phase reactive transport and mineral dissolution in porous media. The approach couples transport and reaction kinetics using a pore-network model that implements a single heterogeneous chemical reaction describing the dissolution of calcite by acidic solutions. The network geometry is updated based on the dissolution process happening at the mineral surface that enlarges pores and throats. Importantly, a new algorithm to describe the merging of pores and throats resulting from solid dissolution is introduced to guarantee conservation of the main variables of interest during the merging process. Surface areas and throat conductances are accurately conserved upon merging using a novel application of correction factors and effective properties. The fluid flow field is also updated due to the new pore-network configuration. A wide range of pore-networks are used to study the reactive transport problem. The main results include the mapping and exploration of different dissolution regimes through porosity-permeability evolution curves, acid concentration profiles in the pore network, and the use of statistical criteria to differentiate regimes.

Contents

Acknowledgments	iv
List of Figures	xi
List of Tables	xviii
1 Introduction	1
1.1 Objectives	4
1.2 Thesis outline	5
2 Literature Review	7
2.1 Reactive transport problem and applications	7
2.1.1 CO ₂ injection for storage and EOR	8
2.1.2 Acidizing for stimulation	10
2.2 Reactive transport and dissolution regimes	11
2.2.1 Behavior diagrams	11
2.2.2 Porosity-permeability relationship	13
2.3 Pore-scale modeling of reactive transport	15
2.3.1 Pore-network modeling	17
2.3.1.1 History and applications	18
2.3.1.2 Pore-network construction	19
2.3.1.3 Pore-network modeling of reactive transport	20
2.3.1.3.1 Merging techniques	22
3 Construction of behavior diagrams and the novel quantitative criteria	25
3.1 Objectives and contributions	25
3.2 Methodology	26

3.2.1	Pore-network models construction	26
3.2.2	Pressure field	27
3.2.3	Concentration field	28
3.2.4	Dissolution reactions	31
3.2.5	Geometry update	32
3.2.6	Implementation	35
3.2.7	Dimensionless numbers	37
3.2.8	Statistics and regimes classification	38
3.3	Results and discussion	39
3.3.1	Identification of the dissolution regimes	40
3.3.2	Behavior diagrams construction	47
3.3.3	Verification in a 40×40 network	50
3.3.4	3D domain verification	52
3.3.5	Implementation on networks derived from carbonate data	56
3.3.6	Analysis of porosity-permeability curves	57
3.4	Summary	57
4	The novel merging approach	60
4.1	Objectives and contributions	60
4.2	Methodology	61
4.2.1	Pore-network models construction	61
4.2.2	Pressure field	62
4.2.3	Concentration field	63
4.2.4	Kinetics of dissolution	65
4.2.5	Volume evolution and geometry update	65
	4.2.5.1 Algorithm for the geometry update	73
4.2.6	The new merging approach	75
	4.2.6.1 Algorithm of the novel merging approach	82
4.2.7	Dimensionless numbers	83
4.2.8	Quantitative criteria: a more robust approach	83
4.3	Results and discussion	85
4.3.1	Effects of using correction factors	86
4.3.2	Application in two-dimensional networks	87

4.3.2.1	Demonstration of the evolution of the correction factors	95
4.3.3	Application in a regular three-dimensional network	98
4.3.4	Application in a random three-dimensional network	101
4.3.5	Special case of a network generated using a carbonate topology	104
4.3.6	Statistical parameters analysis	107
4.4	Summary	109
5	Conclusions	110
5.1	Future Work	111
	References	114
	Appendices	122
A	Mass balance derivations	123
A.1	Mass balance for pores	123
A.2	Mass balance for throats	126
B	Mass balance errors	128

List of Figures

1.1	Schematic of the main dissolution regimes, where blue represents the acidic fluid and brown the porous medium. (a) Formation of preferential pathways. (b) Surface dissolution regime. (c) Uniform dissolution regime.	1
2.1	Energy-related CO_2 emissions predictions for the entire Earth. Adapted from IEA [31].	8
2.2	Schematic of the porosity-permeability relationships for the main dissolution regimes. Preferential pathways regime (in blue) has the largest increase of permeability, surface dissolution regime (in green) has the largest increase of the porosity, and uniform dissolution regime (in red) presents intermediate behavior.	13
3.1	Scheme of throat ij and the connected pores i and j relevant to the mass balance inside throats.	30
3.2	Pore and throat sizes of the cubic network composed of 10×10 pores.	41
3.3	Evolution of the acid concentration as a function of PVI for pores and throats considering their x and y positions in the 10×10 network in the uniform dissolution I regime ($Pe = 0.00094$ and $Da = 0.00094$).	41

3.4	Simulation results from uniform dissolution II regime ($Pe = 0.00094$ and $Da = 0.0094$): (a) Evolution of the surface area as a function of PVI for pores and throats considering their x and y positions in the 10×10 network; and (b) Evolution of the volumetric flow rate as a function of PVI for throats considering their x and y positions in the 10×10 network.	42
3.5	Evolution of the surface area as a function of PVI for pores and throats considering their x and y positions in the 10×10 network at the transition zone ($Pe = 94$ and $Da = 0.094$).	43
3.6	Simulation results from surface dissolution regime ($Pe = 0.00094$ and $Da = 0.47$): (a) Final acid concentration profile (flow is from the top to the bottom); and (b) Evolution of the surface area as a function of PVI for pores and throats considering their x and y positions in the 10×10 network.	44
3.7	Evolution of the acid concentration as a function of PVI for pores and throats considering their x and y positions in the 10×10 network at the mixed zone ($Pe = 0.0094$ and $Da = 0.47$).	45
3.8	Simulation results from preferential pathway regime ($Pe = 94$ and $Da = 0.47$) in the 10×10 network: Final acid concentration profile (flow is from the top to the bottom). Note that pathways do not span the length of the domain.	46
3.9	Evolution of the porosity-permeability relationship results from 10×10 network simulations.	47
3.10	Behavior diagrams constructed from 10×10 network simulations: (a) Pe - Da ; and (b) Pe - $PeDa$	48
3.11	Behavior diagrams constructed from 10×40 network simulations: (a) Pe - Da ; and (b) Pe - $PeDa$	50

3.12	Final acid concentration profile in the 40×40 network (flow is from the top to the bottom): (a) Uniform dissolution ($Pe = 0.094$ and $Da = 0.0007$); (b) Surface dissolution ($Pe = 0.00094$ and $Da = 0.45$); and (c) Preferential pathways ($Pe = 94$ and $Da = 0.45$). Note that the color scale is different for each subfigure to feature differences among the regimes.	51
3.13	Porosity-permeability relationship results from 40×40 network simulations.	52
3.14	Scheme of the initial geometry for the network composed of $10 \times 10 \times 10$ pores.	53
3.15	Acid concentration for the network composed by $10 \times 10 \times 10$ pores: (a) Uniform Dissolution; (b) Surface Dissolution; and (c) Preferential Pathways.	54
3.16	Porosity-permeability relationship results from $10 \times 10 \times 10$ network simulations.	55
3.17	Final acid concentration profile for a uniform dissolution regime simulation in network derived from a carbonate rock sample. A narrow concentration scale is used to highlight the differences in concentration within the network.	56
4.1	Scheme of the boundary condition pores (in red). Pores in blue represent the porous medium under analysis. The properties of boundary pores do not change in time.	65
4.2	Scheme of the change in volume due to dissolution for pores and throats. δr_i^d and δr_{ij}^d represents the radius increase, respectively for pores and throats.	66
4.3	Scheme of the change in volume due to double dissolution ($\delta V_{i,ij}^{dd}$). Hatched area in red represents the contact area between pore i and connecting throats ij that is dissolved twice and δr_i^{dd} is the respective pore radius increase.	67

4.4	Scheme of the change in volume due to correction 1 ($\delta V_{i,ij}^{c1}$). Hatched area in green represents the contact area between pore i and connecting throats ij that needs to be relocated and δr_i^{c1} is the respective pore radius increase.	69
4.5	Scheme of the change in volume due to correction 1 ($\delta V_{i,ij}^{c2}$). Hatched area in blue represents the contact area between pore i and connecting throats ij that needs to be relocated and δr_i^{c2} is the respective pore radius increase.	70
4.6	Scheme of $\delta V_{i,ij}^t$. Scheme of the change in volume due to transfers ($\delta V_{i,ij}^t$). Hatched area in purple represents the porous area of throats ij that needs to be transferred to pore i and δr_i^t is the respective pore radius increase.	72
4.7	Flowchart with the main steps to obtain the total change in volume of pores and throats. The main steps include changes due to dissolution, double dissolution, corrections 1 and 2, and transfer of porous spaces.	72
4.8	The two original pores are replaced by one new pore, that has the same total volume, total mass of acid, and total effective surface area as the two original pores.	77
4.9	The volume, the mass of acid, the effective surface area, and the effective conductance are conserved for the new throat connecting the merged pore m and the connected pore k	79
4.10	The merging pores are connected to the same pore k . In this case, one new throat, with the same total volume, mass of acid, effective surface area, and effective conductance as the two original throats, is created.	80

4.11	Flowchart of the novel methodology for merging of pores and throats. In summary, for each time step, after solving the reactive transport problem and the geometry update, merging conditions are evaluated and if it is necessary, the merging method is performed. Geometry update is also necessary after performing a merging process, and, for this case, correction factors must be updated.	82
4.12	Permeability versus porosity curves obtained for simulations not considering the use of correction factors (red curve) and the use of correction factors (blue curve). The use of correction factors enables a continuous evolution of permeability and porosity of the network under dissolution conditions (see inset that is magnified). The deformation of the original pore spaces due to the merging hypothesis impacts significantly the behavior of the $K - \phi$ curves.	87
4.13	Acid concentration profile at the end of simulation for the 10x10 network. (a) Condition 1, characterized by a preferential pathways regime, after 111 PVI. (b) Condition 2, characterized by a surface dissolution regime, after 111 PVI. (c) Condition 3, characterized by a uniform dissolution regime, after 1323 PVI. (d) Conditions 4, characterized by a uniform dissolution regime, after 1323 PVI. . .	88
4.14	Permeability versus porosity curves obtained for simulations in the 10x10 network.	89
4.15	Acid concentration profile at the end of simulation for the 20x20 network. (a) Condition 1, characterized by a preferential pathways regime, after 88 PVI. (b) Condition 2, characterized by a surface dissolution regime, after 88 PVI. (c) Condition 3, characterized by a uniform dissolution regime, after 876 PVI. (d) Condition 4, characterized by a uniform dissolution regime, after 876 PVI. . . .	90
4.16	Flow rate profile for Condition 1, characterized by a preferential pathways regime, after 88 PVI in the 20x20 network.	91
4.17	Permeability versus porosity curves obtained for simulations in the 20x20 network.	91

4.18	Acid concentration profile at the end of simulation for the 40x40 network. (a) Case 1, characterized by a preferential pathways regime, after 94 PVI. (b) Condition 2, characterized by a surface dissolution regime, after 94 PVI. (c) Conditions 3, characterized by a uniform dissolution regime, after 450 PVI. (d) Condition 4, characterized by a uniform dissolution regime, after 450 PVI. . . .	92
4.19	Flow rate profile for Condition 1, characterized by a preferential pathways regime, after 94 PVI in the 40x40 network.	93
4.20	Permeability versus porosity curves obtained for simulations in the 40x40 network.	94
4.21	Final profile of the correction factor for the effective surface area of pores (ψ_i) considering Case 1, characterized by a preferential pathways dissolution regime. (a) Simulation in the 20x20 network after 111 PVI. (b) Simulation in the 40x40 network after 88 PVI. . .	96
4.22	Final profile of the correction factor for the effective surface area of throats (ψ_{ij}) considering Condition 1, characterized by a preferential pathways dissolution regime. (a) Simulation in the 20x20 network after 111 PVI. (b) Simulation in the 40x40 network after 88 PVI.	97
4.23	Final profile of the correction factor for the effective conductance of throats (ϵ_{ij}) considering Case 1, characterized by a preferential pathways dissolution regime. (a) Simulation in the 20x20 network after 111 PVI. (b) Simulation in the 40x40 network after 88 PVI. . .	98
4.24	Acid concentration profile at the end of simulation for the 10x10x10 network. (a) Condition 1, characterized by a preferential pathways regime, after 111 PVI. (b) Condition 2, characterized by a surface dissolution regime, after 111 PVI. (c) Condition 3, characterized by a uniform dissolution regime, after 1037 PVI. (d) Condition 4, characterized by a uniform dissolution regime, after 1037 PVI.	99
4.25	Permeability versus porosity curves obtained for simulations in the 10x10x10 network.	100

4.26	Acid concentration profile at the end of simulation for the three-dimension random network. (a) Condition 1, characterized by a preferential pathways regime, after 135 PVI. (b) Condition 2, characterized by a surface dissolution regime, after 135 PVI. (c) Condition 3, characterized by a uniform dissolution regime, after 1212 PVI. (d) Condition 4, characterized by a uniform dissolution regime, after 1212 PVI.	102
4.27	Permeability versus porosity curves obtained for simulations in the three-dimensional random network.	103
4.28	Acid concentration profile at the end of simulation for the carbonate-derives network. (a) Condition 1, characterized by a preferential pathways regime, after 186 PVI. (b) Condition 2, characterized by a surface dissolution regime, after 139 PVI. (c) Condition 3, characterized by a uniform dissolution regime, after 4182 PVI. (d) Condition 4, characterized by a uniform dissolution regime, after 2788 PVI.	105
4.29	Permeability versus porosity curves obtained for simulations in the carbonate-derived network.	106

List of Tables

3.1	Comparison among power-law exponents for the uniform dissolution regime.	58
4.1	Initial porosity (ϕ_0) and initial absolute permeability (K_0) of the networks used in this study	62
4.2	Simulation conditions explored based on the dimensionless numbers Pe , Da , and $PeDa$	86
4.3	Power-law exponents and coefficients of determination (R^2) obtained for the simulations in the two-dimensional networks.	94
4.4	Power-law exponents and coefficients of determination (R^2) obtained for the regular three-dimensional network.	101
4.5	Power-law exponents and coefficients of determination (R^2) obtained for the random three-dimensional network.	103
4.6	Power-law exponents and coefficients of determination (R^2) obtained for the carbonate-derived network.	107
4.7	Statistical parameter CV obtained for all the simulation conditions for the six networks explored.	108
4.8	Statistical parameter ΔC obtained for all the simulation conditions for the six networks explored.	108
B.1	Mass balance error (%) obtained in the simulations.	129
B.2	Time-step sizes (in seconds) used in the simulations.	130
B.3	Number of time steps used in the simulations.	130

Nomenclature

- A Cross-sectional area of the network
- $A_{(t)}$ Closed surface area of a control volume $V_{(t)}$ at instant t
- $A_{\psi,ij}$ Effective surface area of throat ij
- $A_{\psi,i}$ Effective surface area of pore i
- $A_{i,ij}$ Surface area of the semi-sphere formed by pore i and throat ij
- A_{in} Surface area at the inlet region
- A_{out} Surface area at the outlet region
- $A_{r,ij}$ Available reactive surface area of throat ij
- $A_{r,i}$ Reactive surface area of pore i
- $A_{r,mk}^{n+1}$ Reactive surface area of the new throat connecting the merged pore m and the connected pore k
- A_r Surface area available for reaction
- A_{ss} Specific surface area of the porous medium
- $C_{\alpha,ij}$ Mass concentration of species α in throat ij
- $C_{\alpha,in}$ Mass concentration of specie α in the inlet pore spaces
- $C_{\alpha,i}$ Mass concentration of species α in pore i
- $C_{\alpha,out}$ Mass concentration of specie α in the outlet pores

$c_{\epsilon,ij}$	Effective conductance of throat ij
c_{ij}	Conductance of throat ij
c_{mk}^{n+1}	Conductance of the new throat connecting the merged pore m and the connected pore k
CV	Averaged coefficient of variation
CV_{cs}	Coefficient of variation of cross section cs
d_{mk}	Interpore distance between the new merged pore m and the connected pore k
J_{α}	Mass diffusive flux
K	Absolute permeability of the network
k_r	Kinetic constant of the heterogeneous chemical reaction
l_{ij}	Length of throat ij
M	Molar mass
N	Number of pores and throats that are evaluated
$\hat{\mathbf{n}}$	Exterior normal to the boundary
P_i	Pressure in pore i
P_j	Pressure in pore j
$q_{i,out}$	Total volumetric flow rate that arrives in each outlet pore
q_{ij}	Volumetric flow rate through throat ij
r_i	Radius of pore i
$R_{\alpha,ij}$	Reaction rate of specie α due to heterogeneous chemical reaction in throat ij
$R_{\alpha,i}$	Reaction rate of specie α due to heterogeneous chemical reaction in pore i
r_{ij}	Radius of the cross section of throat ij

r_k^{n+1}	Radius of the pore k connected to the new merged pore m
r_{mk}^{n+1}	Radius of the new throat connecting the merged pore m and the connected pore k
r_m^{n+1}	Radius of the new merged pore m
s_α	Source term related to homogeneous chemical reactions
t	Time
\mathbf{v}	Average mass velocity of the fluid
\mathbf{v}_c	Velocity of the control volume
v_0	Initial inlet velocity
$V_{(t)}$	Control volume at instant t
V_{ij}	Volume of throat ij
V_i	Volume of pore i
\mathbf{x}	Position vector
z	Coordination number

Acronyms

2D	Two-dimensional
3D	Three-dimensional
CFD	Computational fluid dynamics
DBS	Darcy–Brinkman–Stokes
DNS	Direct numerical simulation
LBM	Lattice Boltzmann method
PNM	Pore-network modeling
PVI	Pore volumes of injectant

SPH Smoothed particle hydrodynamics

Dimensionless numbers

Da Damköhler (reaction rate/advection rate)

Pe Péclet (advection rate/diffusion rate)

$PeDa$ Péclet-Damköhler (reaction rate/diffusion rate)

Re Reynolds (inertial forces/viscous forces)

Greek symbols

β Stoichiometric coefficient in mass basis that relates the acid consumption with the consumption of the reactive mineral

ΔC Measure of the consumption of acid along the network

$\delta m_{i,ij}^t$ Mass of acid in the porous region previously belonged to throat ij transferred to pore i

δm_{ij}^t Total change in mass of acid due to porous space transfer from throat ij to pore i , for throat ij

δm_i^t Total change in mass of acid due to porous space transfer from throat ij to pore i , for pore i

ΔP Pressure difference through the network

δr_{ij}^d Change in radius of throat ij due to dissolution process

δr_i^d Change in radius of pore i due to dissolution process

δr_i^{c1} Change in radius of pore i due to correction 1

δr_i^{c2} Change in radius of pore i due to correction 2

δr_i^{dd} Change in radius of pore i due to double dissolution

δV_i^d Change in volume due to dissolution process in pore i

$\delta V_{i,ij}$ Volume double dissolved by throat ij and the connected pore i

- $\delta V_{i,ij}^{c1}$ Change in volume due to correction 1 in the region between pore i and throat ij
- $\delta V_{i,ij}^{c2}$ Change in volume due to correction 2 in the region between pore i and throat ij
- $\delta V_{i,ij}^{dd}$ Change in volume due to double dissolution in the region between pore i and throat ij
- $\delta V_{i,ij}^t$ Previous throat ij porous region transfer to pore i
- δV_{ij} Total change in volume of throat ij
- δV_{ij}^d Change in volume due to dissolution process in throat ij
- δV_{ij}^{c1} Total change in volume due to correction 1 for throat ij
- δV_{ij}^{c2} Total change in volume due to correction 2 for throat ij
- δV_{ij}^{dd} Total change in volume due to double dissolution for throat ij
- δV_{ij}^t Total change in volume due to porous space transfer from throat ij to pore i , for throat ij
- δV_i Total change in volume of pore i
- δV_i^{c1} Total change in volume due to correction 1 for pore i
- δV_i^{c2} Total change in volume due to correction 2 for pore i
- δV_i^{dd} Total change in volume due to double dissolution for pore i
- δV_i^t Total change in volume due to porous space transfer from throat ij to pore i , for pore i
- $\delta V_{j,ij}$ Volume double dissolved by throat ij and the connected pore j
- ϵ_{ij} Correction factor for the conductance of throat ij
- D_α Diffusion coefficient of species α
- μ Dynamic viscosity of the fluid

ψ_{ij}	Surface area correction factor of throat ij
ψ_i	Surface area correction factor of pore i
ψ_{mk}^{n+1}	Correction factor of the new throat connecting the merged pore m and the connected pore k
ρ_f	Fluid density
ρ_s	Density of the solid reactive mineral
σ	Standard deviation
σ_{cs}	Standard deviation of cross section cs

Subscripts

α	Chemical species α
ϵ	Effective property related to conductance
ψ	Effective property related to surface area
cs	Cross-sectional partition
i	Pore i
ij	Throat connecting pores i and j
j	Pore j
k	Pore k that is connected to the merged pore m
L	Length of the network
m	Merged pore
mk	Throat mk that connects merged pore m and pore k
ps	Pore space that belongs to a partition
s	Solid

Superscripts

- c1* Correction iteration 1
- c2* Correction iteration 2
- d* Mineral dissolution
- dd* Double dissolution
- n* Related to the present time step
- n + 1* After updating network geometry
- n + 1,** Related to the intermediate state after solving transport and before geometry update
- t* Transferred porous space

Chapter 1

Introduction

Reactive transport in porous media and mineral dissolution processes are of extreme interest for many subsurface applications, including carbon dioxide (CO_2) storage, Enhanced Oil Recovery (EOR), and acidizing for stimulation [1, 2, 3, 4]. Changes in porosity and permeability of porous media, as well as the observation of various dissolution patterns of the porous medium are consequences of these dynamic processes [5, 6].

Depending on the dominant transport mechanism and the reactivity of the mineral solid surface, different dissolution patterns are observed [7, 6]. Consequently, good understanding of the dissolution processes is imperative to assess long-term reservoir integrity properties for CO_2 storage and to design efficiently acidizing treatments [8, 9, 10]. Figure 1.1 presents a schematic of the main dissolution types that are discussed in more details in later sections.

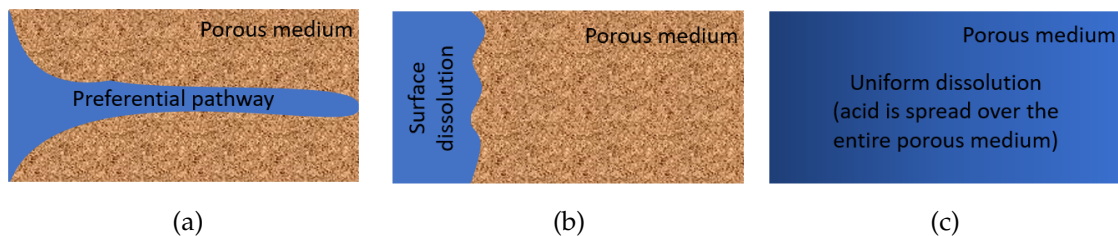


Figure 1.1: Schematic of the main dissolution regimes, where blue represents the acidic fluid and brown the porous medium. (a) Formation of preferential pathways. (b) Surface dissolution regime. (c) Uniform dissolution regime.

CO_2 injection for storage and EOR processes trigger the occurrence of chemical reactions that induce changes in mechanical properties of the rock, especially

in porous media rich in carbonate minerals [11, 8, 9]. For geological CO_2 storage such mineralogical alterations are a source of concern for the safety and efficiency of the technique because mineral dissolution may increase the chance for leakage and also CO_2 migration out of the storage formation [11, 8, 9]. As discussed by OTT and OEDAI [12], the consequences of these dynamics interactions are dependent on the transport regimes. Formation of preferential pathways bypasses rock matrix and leads to poor utilization of the pore space for the storage of CO_2 ; surface dissolution alters the mechanical integrity of the rock near the well, where most of the acid is consumed; and uniform dissolution might lead to subsidence due to weakening of mechanical properties of the reservoir.

Regarding acidizing for well stimulation, formation of preferential pathways increases the overall conductance through the reservoir and, consequently, the well productivity [13, 12]. Also, for a given volume of injected fluid, the deeper the wormhole penetration into the reservoir the better. Therefore, single dominant wormhole channels at intermediate injection rates are often desired and represent the most effective stimulation [14].

In this context, dimensionless numbers characterize reactive-transport regimes [15]. The use of dimensional analysis is a standard tool in transport phenomena that aims to derive the relevant dimensionless parameters that control the physics of a specific problem [16]. The Péclet number (Pe) is defined as the ratio of the advection rate to the rate of diffusion of a chemical species and the Damköhler number (Da) is defined as the ratio of the reaction rate to the advection rate. The Péclet-Damköhler number ($PeDa$) is the ratio of the reaction rate and the diffusive mass transfer rate.

Based on dimensionless numbers, behavior diagrams (or phase diagrams) are useful to define flow boundaries for different dissolution regimes [17, 7, 6, 18, 19]. Porosity-permeability relationships have also been used to understand and characterize different patterns of dissolution in porous media at the pore-scale [16, 5, 18, 6].

In this way, uniform dissolution (see Fig. 1.1c) is described as a reaction-limited process, where the reactive solute is spread over the whole porous medium and the dissolution is nearly uniform all over the available reactive

surface [16, 7].

For systems with greater reactivity, the dissolution pattern depends upon the dominant transport process. Surface dissolution (or compact dissolution) is characterized by the dominance of the diffusion mechanism over transport by advection and, consequently, dissolution mainly occurs in the inlet area of the porous medium [18, 7]. In this regime, a uniform concentration profile is observed along the cross-sections perpendicular to the flow. Figure 1.1b presents a schematic of this regime. Preferential pathways (or wormholing) are observed when the predominant mechanism is advection (see Fig. 1.1a). A mixed dissolution pattern is described by LIU and MOSTAGHIMI [18] as a transition zone between face dissolution and wormholing.

SOULAINÉ *et al.* [6] and GOLFIER *et al.* [7] differentiate wormholing using three different regimes. Conical wormholes are observed for larger injection rates, but still in a diffusion-dominated mechanism, where solute starts to penetrate into the porous medium and the uniform patterns along the vertical cross-sections are no longer observed. One dominant wormhole can be observed for intermediate flow rates, where the reactive solute penetrates preferentially into the biggest pore spaces to form flow channels and, consequently, the formation of a dominant wormhole. Ramified wormholes occur at large injection rates and are characterized by wormholes becoming more branched.

In order to investigate the dissolution processes in porous media, several numerical approaches, such as direct numerical simulation (DNS) that includes computational fluid dynamics (CFD) [6, 20], lattice Boltzmann method (LBM) [18], and smoothed particle hydrodynamics (SPH) [21], and approaches that considers a simplified conceptualization of the porous media, commonly associated with pore-network modeling (PNM), have been developed.

Pore network modeling is a technique that is widely used to represent natural porous media and complex pore geometries are represented using a simplified pore-and-throat type network [5]. Since the pioneering work of FATT [22], that studied two-phase flow and capillary pressure curves, pore-network models have been successfully applied in numerous research areas, including reactive transport and mineral dissolution problems [23, 5, 24, 25]. The compu-

tational efficiency of pore-network models are related to the simplicity of their geometry and because of this feature, pore-network modeling is considered applicable to much larger domains when compared to direct simulation methods [26, 27].

The inherent pore-scale heterogeneity of porous media and the complexity involved in the physics of transport and interactions in such complex systems are still a significant challenge to the development of representative models to the analysis and design of efficient and safe CO_2 injection processes.

Indeed, for a fuller understanding of larger scale effects of reactive transport and mineral dissolution process, the pore-scale issues in subsurface systems must be comprehended first. Pore-scale modeling allows the analysis of the fundamental mechanisms and processes at small scales that are essential to understand behaviors observed in larger scale problems [28, 26]. Therefore, modeling of the pore-scale phenomena involved in reactive flow through porous media is an important step towards understanding the changes in permeability and porosity as well as different dissolution patterns observed at larger scales relevant to geological sequestration of CO_2 and acidizing for well stimulation.

1.1 Objectives

The main objective of this research is to study the occurrence of different dissolution regimes in a porous medium subject to various flow and reactivity conditions during single-phase flow using pore-network modeling.

The specific objectives and main contributions of this work are stated below.

1. Develop a single-phase reactive transport and mineral dissolution formulation using pore-network modeling.
 - (a) Use of open source tools.

Open source tools provide algorithms that can be used as base for more specific and complex developments, saving time and energy of the developer to focus on the real problem of interest.
 - (b) Consider moving control volumes, represented by pores and throats.

This enables the algorithm to have maximum capability to develop

complicated dissolution patterns and to track more accurately the evolving of the permeability of the porous medium during the simulations.

2. Define qualitative and quantitative criteria to classify the dissolution regimes.
3. Construct behavior diagrams based on dimensionless numbers to summarize the observed dissolution regimes.
4. Develop a merging approach for pore and throats as they dissolve that maintains mass conservation, reflects geometric details accurately, and is useful to compute flow properties.
 - (a) Introduce the use of correction factors and effective properties, that aims to conserve throat conductances and reactive surface areas while the topology of the network evolves.

Once these objectives are met, the unique contribution of this study to the literature is to present a pore-network methodology to study single-phase reactive transport and mineral dissolution that is able to explore wide ranges of reactivity and flow conditions and are not limited to a fixed topology neither the simplified ball-and-stick geometry of the porous medium. Also, the use of statistical quantitative criteria brings a simple and more accurate way to identify the main dissolution regimes without only relying on qualitative criteria.

1.2 Thesis outline

This thesis is divided into five chapters, including the introduction and conclusion. The contents of all chapters are briefly described in this section. Chapter 3 is reproduced from a published article and the content of Chapter 4 was submitted to a peer-reviewed journal. The thesis outline is summarized as follows.

Chapter 1 is an introductory chapter that presents the research topic and the main objectives of this thesis.

Chapter 2 provides a review of the literature pertaining to the topics relevant to this thesis. First, the problem of reactive transport and mineral dissolution in the context of carbon dioxide (CO_2) injection for storage and for enhanced oil recovery (EOR), and acidizing for stimulation is discussed. Then, the dissolution regimes observed in porous media as well as the use of behavior diagrams and porosity-permeability relationships to classify and identify the boundaries between the various regimes are explored. The chapter closes with the pore-scale numerical approaches used to study reactive transport, mineral dissolution, and accompanying evolution of the morphology of pores and throats. The final focus is on pore-network modeling and pore-merging techniques.

Chapter 3 is devoted to the construction of a pore-network modeling approach to evaluate the effects of different transport mechanisms and mineral reactivity on dissolution regimes, as well as changes in porosity and permeability. A novel quantitative criterion approach is introduced to classify the reactive dissolution regime by interpreting acid distribution within pore space. Behavior diagrams based on dimensionless numbers are constructed aiming to map the different dissolution regimes and their boundaries.

The content of this chapter is reproduced from a manuscript published in *Advances in Water Resources* [29].

Chapter 4 is devoted to the development of a merging methodology, necessary to bring the reactive transport model to the physical problem and make possible the use of reactive transport simulations to evaluate dissolution regimes in more complex network topologies of rocks, such as carbonates, where the junction of two pores initially separated is likely to occur due to the pore-scale heterogeneity of these type of porous media and the relatively large amount of solid dissolved. The main contribution of this new method is to make relevant geometry and flow properties conservative before and after the merging of two overlapping pores.

The content of this chapter was submitted to *Advances in Water Resources*.

Chapter 5 presents the main highlights of this thesis and some suggestions for future studies enabled by this work.

Chapter 2

Literature Review

This chapter presents a literature review that explores the problem of reactive transport and mineral dissolution in the context of carbon dioxide (CO_2) injection for storage and for enhanced oil recovery (EOR), and acidizing for stimulation. The dissolution regimes observed in porous media as well as the use of behavior diagrams and porosity-permeability relationships to classify and identify the boundaries between the various regimes are also presented. The chapter closes with the pore-scale numerical approaches used to study reactive transport and mineral dissolution in porous media and focuses on pore-network modeling.

2.1 Reactive transport problem and applications

Reactive transport in porous media and mineral dissolution processes are of extreme interest for many subsurface applications, including CO_2 storage, Enhanced Oil Recovery (EOR), and acidizing for stimulation [1, 2, 3, 4]. Changes in porosity and permeability of porous media, as well as the observation of various dissolution patterns of the porous medium are consequences of these dynamic processes [5, 6] and directly influence the performance and success of each technique.

2.1.1 CO₂ injection for storage and EOR

Global electricity generation is expected to increase by 60% between the years of 2017 and 2040 and, despite the global efforts to advance renewable energy technologies, such as wind and solar power, fossil fuels are predicted to remain the major source for electricity generation [30] and transportation. Importantly, energy-related CO₂ emissions to the atmosphere, as presented in Fig. 2.1, negatively impact the Earth's climate and should be minimized.

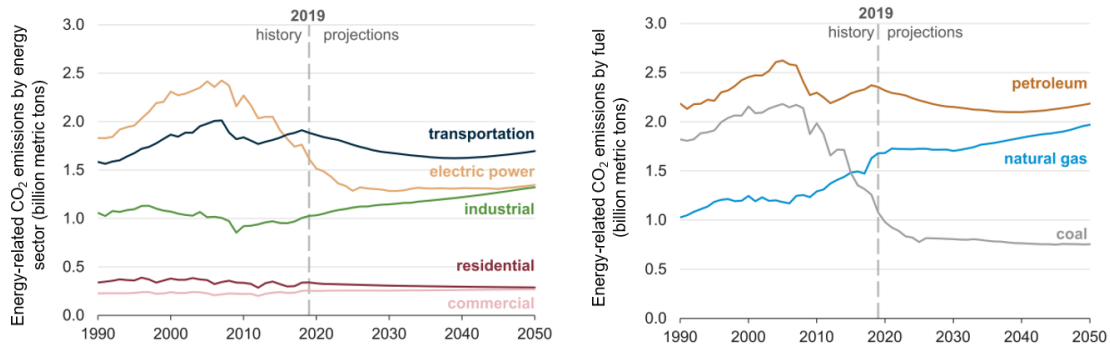


Figure 2.1: Energy-related CO₂ emissions predictions for the entire Earth. Adapted from IEA [31].

Indeed, one of the grand global challenges of our society is to supply efficiently energy demands while minimizing environmental impacts. Development of low energy processes for hydrocarbon recovery methods [32] and subsurface geological storage of carbon dioxide may help to reduce the damages induced by the growth of the energy supply chain.

In this way, the injection and long-term or permanent storage of CO₂ in the subsurface, besides representing an opportunity for enhanced oil recovery, is an opportunity for mitigating the build-up of green-house gases in the atmosphere [33].

With respect to CO₂ injection for storage and for EOR, rock mechanical changes may be induced by chemical reactions, especially in porous media with substantial carbonate minerals [11, 8, 9]. For geological CO₂ storage such mineralogical alterations may be of concern for the safety and efficiency of the technique because mineral dissolution may increase the chance for leakage and also CO₂ migration out of the storage formation [11, 8, 9].

Secure geological CO₂ storage in sedimentary basins considers that CO₂ must

be trapped under low permeability rock to avoid fast migration of CO_2 to the surface. In the case of oil and gas reservoirs, where the reservoir is sealed by a cap-rock, the CO_2 is expected to remain in storage for geological time periods. These type of reservoirs are likely to be the first target for CO_2 geological storage as they are known to be secure since they have held fluids securely over geological time. The storage capacity of such hydrocarbon reservoirs, however, is smaller compared to deep aquifers. Nevertheless, the production of oil and natural gas from sedimentary basins creates voidage in pore spaces that can be refilled with CO_2 , causing depleted reservoirs to be even more attractive for storage [33].

BEMER and LOMBARD [9] obtained experimental data related to porosity, permeability, and geomechanical properties from samples of various permeability levels, before and after CO_2 injection. The results showed the presence of mechanical weakening induced by chemical reactions. The observations are of great interest for CO_2 geological storage, because maintenance of rock mechanical integrity over a very long time range is required for the technical and economical success of this technique. Evaluation of the effective stress fields induced by rock mineral alterations due to exposure of sandstone samples for 1.5 years to a mixture of brine and super-critical CO_2 showed a significantly raised effective stress coefficient when compared to exposure of the rock just to brine [8].

Accounting for changes in porosity and permeability of porous media due to dissolution processes is essential to the modeling and the prediction of injectivity alterations and reservoir pressure field. These dynamic properties may be responsible for severe stress changes and, consequently, impact the integrity of the reservoir [11]. Furthermore, such mineralogical alterations that significantly affect the saline aquifer permeability, also reflect in the safety and efficiency of the sequestration process because they may result in leakage that harms the environment and human communities. Leakage also raises the possibility to increase gradual migration of the CO_2 plume to uncharacterised areas [8].

In summary, as discussed by OTT and OEDAI [12], the consequences of the interactions between CO_2 and the minerals present in the reservoir matrix are dependent on the transport regimes. Formation of preferential pathways by-

passes rock matrix and leads to poor utilization of the pore space for the storage of CO_2 . Surface dissolution alters the mechanical integrity of the rock near the well, where most of the acid is consumed. Uniform dissolution might lead to subsidence due to weakening of mechanical properties of the reservoir.

Modeling of the pore-scale phenomena involved in reactive flow through porous media is an important step towards understanding the changes in permeability and porosity as well different dissolution patterns observed at larger scales.

2.1.2 Acidizing for stimulation

Acidizing with hydrochloric acid (HCl) is the most common matrix stimulation treatment. The main goal is to increase the permeability near the wellbore and enhance the productivity of a tight or damaged well. Considering the near-wellbore feature, most of all the acid reacts within about 1 ft of the wellbore in sandstone formations and within a few inches to around 10 ft in carbonates [13].

Formation of preferential pathways increases the overall conductance through the reservoir and, consequently, the well productivity [13, 12]. Also, for a given volume of injected fluid, the deeper the wormhole penetration into the reservoir the better. Indeed, the optimum injection rate is related to a minimum volume of fluid required to obtain a given depth of wormhole penetration.

Single dominant wormhole channels are obtained at intermediate injection rates and represent the most effective way of matrix stimulation. An optimum Damkohler of approximately 0.29 is observed for this channel formation pattern [34]. In this way, a successful acidizing treatment requires maximum acid contact with all damaged areas (a good acid distribution), that is usually hindered by variations in the injectivity along the wellbore [13].

Considering that wormhole structure varies as a function of flow conditions and fluid-mineral properties, and dissolution of porous media can enhance the naturally present permeability contrasts along a wellbore, a fundamental understanding of the dissolution process is imperative to design efficiently acidizing treatments [10].

2.2 Reactive transport and dissolution regimes

Depending on the dominant transport mechanism and the reactivity of the mineral solid surface, different dissolution patterns within a porous medium are observed [7, 6]. Uniform dissolution [16, 7, 18, 6], compact or face or surface dissolution [16, 7, 18, 6], preferential pathways or wormholing, mixed dissolution [18], conical wormholes [7, 6], one-dominant wormhole [7, 6], and ramified wormholes [7, 6] are all examples of different dissolution regimes observed in the literature.

In this section, the dissolution regimes are characterized and discussed. Behavior diagrams and porosity-permeability relationships are introduced to explain better the features and boundaries of each of the regimes.

2.2.1 Behavior diagrams

The use of dimensional analysis is a standard tool in transport phenomena that aims to derive the relevant dimensionless parameters that control the physics of a specific problem [16].

Dimensionless numbers characterize reactive-transport regimes [15]. The Péclet number (Pe) is defined as the ratio of the advection rate to the rate of diffusion of a chemical species and the Damköhler number (Da) is defined as the ratio of the reaction rate to the advection rate. The Péclet-Damköhler number ($PeDa$) is the ratio of the reaction rate and the diffusive mass transfer rate. Based on dimensionless numbers, behavior diagrams, or phase diagrams, are useful to define flow boundaries for different dissolution regimes [17, 7, 6, 18, 19].

Uniform dissolution is described as a reaction-limited process, where the reactive solute is spread over the whole porous medium and the dissolution is nearly uniform all-over the available reactive surface [16, 7]. This regime is defined by BÉKRI *et al.* [16] for $PeDa < 1$ and by SOULAINÉ *et al.* [6] for $Da \leq 1$, while for LIU and MOSTAGHIMI [18] the boundaries of this regime depend on the correlation length of the porous medium. Note that characteristic lengths used to compute the dimensionless numbers are not the same, and consequently, boundaries between the different regimes are slightly different,

despite the agreement of the general features of the behavior diagrams. The exact equation of each cited value of dimensionless numbers can be found in the respective referenced literature.

For systems with greater reactivity, in the case of BÉKRI *et al.* [16] for $PeDa > 1$, the dissolution pattern depends upon the dominant transport process. Surface dissolution (or compact dissolution) is characterized by the domination of the diffusion mechanism over transport by advection and, consequently, dissolution mainly occurs in the inlet area of the porous medium [18, 7]. In this regime a uniform concentration profile is observed along the cross-sections perpendicular to the flow. SOULAINÉ *et al.* [6] observed this pattern for $Pe \leq 10^{-2}$ and $Da > 1$. Preferential pathways (or wormholing) are observed when the predominant mechanism is advection. For BÉKRI *et al.* [16] this regime is observed for $PeDa > 1$ and for SOULAINÉ *et al.* [6] for $Da > 1$.

A mixed dissolution pattern is described by LIU and MOSTAGHIMI [18] and KANG *et al.* [35] as a transition zone between face dissolution and wormholing.

SOULAINÉ *et al.* [6] and GOLFIER *et al.* [7] differentiate wormholing using three different regimes. Conical wormholes are observed for larger injection rates, but still in a diffusion-dominated mechanism, where solute starts to penetrate into the porous medium and the uniform patterns along the vertical cross-sections are no longer observed ($10^{-2} < Pe \leq 1$ and $Da > 1$ for SOULAINÉ *et al.* [6] and around $10^{-3} < Pe < 10^{-2}$ and $Da > 10^{-3}$ for GOLFIER *et al.* [7]). One dominant wormhole can be observed for intermediate flow rates ($1 < Pe \leq 10$ and $Da > 1$, according to SOULAINÉ *et al.* [6]) where the reactive solute penetrates preferentially into the biggest pore-spaces to form flow channels and, consequently, the formation of a dominant wormhole. Ramified wormholes occur at large injection rates, for $Pe > 10$ and $Da > 1$ [6], and are characterized by wormholes becoming more branched.

Importantly, to date, behavior diagrams have been explored based on qualitative features of the dissolution regimes observed in reactive transport experiments and simulations in porous media. Moreover, behavior diagrams constructed based on pore-network modeling simulations are not available in the literature.

2.2.2 Porosity-permeability relationship

Porosity-permeability relationships are a necessary tool for reservoir simulation [36, 6]. As stated by ALGIVE *et al.* [37], the determination of a porosity-permeability relationship is a key issue to improve predictivity of reactive transport simulation, including CO_2 injection applications for storage and EOR.

Porosity-permeability relationships have also been used to understand and characterize different patterns of dissolution in porous media at the pore-scale [36, 37, 5, 38, 35, 39, 18, 6]. Studies have demonstrated that the evolution of the curves of porosity-permeability depend on the dissolution regime obtained by reactive transport experiments and simulations. Figure 2.2 presents a schematic of the permeability versus porosity curves for the main dissolution regimes.

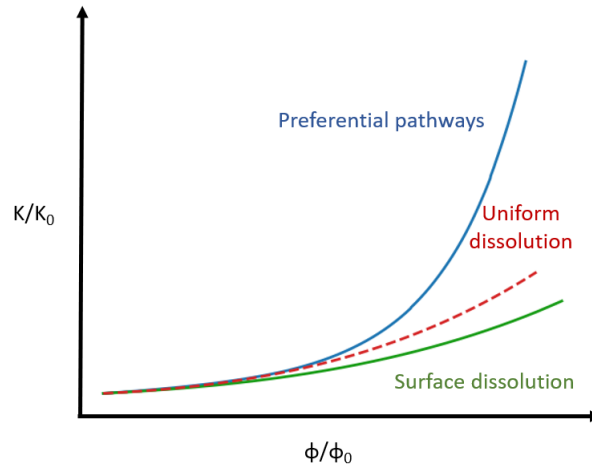


Figure 2.2: Schematic of the porosity-permeability relationships for the main dissolution regimes. Preferential pathways regime (in blue) has the largest increase of permeability, surface dissolution regime (in green) has the largest increase of the porosity, and uniform dissolution regime (in red) presents intermediate behavior.

BHAT and KOVSCEK [36] applied a pore-network model to gauge how evolving pore spaces due to silica dissolution affect porosity and permeability. They showed that permeability increases most dramatically for networks with large values of throat to pore aspect ratio. Also, they observed that for a moderate range of dissolution (10%) porosity-permeability relationship can be modeled as a simple power-law relation.

ALGIVE *et al.* [37] studied the impact of the different deposition regimes on the relationships between permeability and porosity through 2D pore-network

modeling simulations and experiments in glass micromodels. ALGIVE *et al.* [5] used the same pore-network approach to study dissolution and precipitation phenomena in more complex networks. Both studies explored the different patterns of dissolution and deposition by varying Pe and $PeDa$ numbers and evaluating the effects on porosity-permeability relationships.

VARLOTEAUX *et al.* [38] used a pore-network model extracted from microtomography images to investigate porosity–permeability evolution during reactive transport as a function of the dimensionless numbers Pe and $PeDa$. They identified three families of K - ϕ laws. Uniform dissolution ($PeDa \ll 1$), characterized by a linear pattern of the K - ϕ curve and explained by a uniform chemical disequilibrium over the whole network. Compact dissolution ($PeDa \gg 1$ and $Pe \ll 1$), where the observed permeability variations are relatively small compared to uniform dissolution. This is because diffusion is the limiting factor and disequilibrium is maintained in the greatest elements (pores) that do not contribute significantly to permeability increase. Finally, wormhole dissolution ($PeDa > 1$ and $Pe \gg 1$), characterized by reaction occurring along the main flow paths when the flow rate of the fluid and the reaction kinetic are high enough. Here, permeability variations are larger than for uniform dissolution. These three families of K - ϕ relationship were also observed by BEKRI *et al.* [39].

EGERMANN *et al.* [11] investigated the power-law exponent of the curves obtained by plotting $\log(K/K_0)$ versus $\log(\phi/\phi_0)$ from simulation results in regular pore-networks and core-flood experiments, and related the power-law exponent with the dissolution pattern. Reaction-limited regimes were identified between values of 1.5 and 6.9.

More recently, LIU and MOSTAGHIMI [18] explored a wider range of porosity change using a lattice Boltzmann approach for reactive transport and dissolution simulation. Porosity-permeability relationships were evaluated for a porosity increase of 30% and demonstrated agreement with the previously cited literature.

SOULAINÉ *et al.* [6] went further and presented porosity-permeability relationships for the five different regimes observed in their Darcy–Brinkman–Stokes formulation (DBS) formulation for reactive transport: uniform dissolution and

compact dissolution, previously discussed; and conical dissolution, dominant wormhole, and ramified wormholes. They observed that more important permeability variations involved large wormholes, such as those from conical dissolution and single dominant wormhole. This is explained by the injected fluid flowing preferentially along the new pathway created by the wormhole. As soon as the wormhole reached the outlet area, the flow resistance is controlled by the aperture of the wormhole in the vicinity of the outlet region.

Notably, evidence of porosity-permeability relationships being dependent on the heterogeneity of the porous media has also been shown. KANG *et al.* [35] presented a LBM pore-scale study of dissolution-induced changes in hydrologic properties of two porous media represented by a simple fracture and a more complex 2D porous medium. The permeability–porosity relationship was explored for a wide range of $PeDa$ and Da dimensionless numbers. It was also observed that the K - ϕ power law exponents also depend on the porous medium geometry. The clear effect of the Da on K - ϕ curves observed for the fracture system was not observed for the 2D porous medium and is deeply discussed in the text, relating this observation with the complex structure of the porous medium.

2.3 Pore-scale modeling of reactive transport

Pore-scale modeling provides a valuable opportunity to study the fundamental mechanisms and processes at small scales that are essential to understand behaviors observed in larger scale problems [28, 26]. High-performance computing resources allow researchers to perform detailed numerical experiments for a wide range of conditions that would be costly or even impossible to obtain by laboratory experiments considering the wide range of parameters and complexities of the porous media to be evaluated. With this, it becomes clear that pore-scale simulations are an important tool for the understanding of large-scale natural processes [40, 28, 41].

Several numerical approaches have been developed to investigate reactive transport and mineral dissolution in porous media. Direct numerical simulation (DNS) is applied directly on the complex pore geometry of the porous medium

and includes computational fluid dynamics (CFD), lattice Boltzmann method (LBM), and smoothed particle hydrodynamics (SPH). Approaches that consider a simplified conceptualization of the porous media are commonly associated with pore-network modeling (PNM).

Computational fluid dynamics applications to pore-scale simulations solve the mass and momentum conservation equations for laminar flow and transport using various numerical discretization methods, such as the finite volume method and the finite difference method, on a mesh that retains the full pore geometry to the limits of the grid resolution [27, 42]. Recent studies using CFD approaches include the work of SOULAINÉ *et al.* [6], that proposed a Darcy-Brinkman-Stokes (DBS) approach that was also compared with micro-model experiments simulating the dissolution of a calcite grain, and the work of OLIVEIRA *et al.* [20], that presents a model to simulate multiple species reactive transport on pore space images by solving the Navier–Stokes equations and the advection-diffusion equation for concentration on an unstructured grid using the finite volume method.

The lattice Boltzmann method is a particle-based numerical approach that easily represents transport phenomena in complex geometries using simple Cartesian grids [27]. LBM is fully parallel and it has been successfully explored for a variety of flow and transport problem in porous media. For example, LIU and MOSTAGHIMI [18] proposed a lattice Boltzmann method to explore the effects of different correlation lengths on dissolution patterns obtained through reactive transport simulations.

Smoothed particle hydrodynamics is a Lagrangian approach that applies a mesh-free discretization scheme for the solution of partial differential equations and has been shown to be a numerical method to study complex physic phenomena as reactive transport and precipitation in porous media [43]. TARTAKOVSKY *et al.* [21] present a review with the latest developments of the SPH applied to pore-scale flow and transport applications.

Direct numerical simulations demand high computational cost and, consequently, present a limitation of the size and scale that the problems can be explored [27]. Lagrangian particle methods are even more computationally de-

manding than grid-based methods, even though this point could be partially overcome by parallel computing techniques [21].

Pore-network modeling is a numerical approach that has been successfully used to study reactive transport and dissolution processes at the pore-scale and is very popular for its capacity of represent complex geometry of the porous media by a simplified pore-and-throat type network and, consequently, overcoming the limitations of a high-computation-demand numerical method. Pore-network modeling is the numerical approach chosen for the development of this thesis and it is discussed in detail in a later section.

More details of different pore-scale modeling techniques for fluid flow and solute transport can be found at MEAKIN and TARTAKOVSKY [40], MEHMANI and BALHOFF [26], YANG *et al.* [27], and OOSTROM *et al.* [42].

2.3.1 Pore-network modeling

Pore-network modeling is a technique that is widely used to represent natural porous media where complex pore geometries are represented using a simplified pore-and-throat type network [5]. Since the pioneering work of FATT [22], that studied two-phase flow and capillary pressure curves, pore-network models have been successfully applied in numerous research areas, including reactive transport and mineral dissolution problems [23, 5, 24, 29]. Note that a lot of the application of pore-network modeling to date has been to look at the effect of wettability and contact angle on relative permeability and capillary pressure [44, 45, 46, 47]. The computational efficiency of pore-network models are related to the simplicity of their geometry and because of this feature, pore-network modeling is considered applicable to much larger domains when compared to direct simulation methods [26, 27].

This section presents the history and applications of pore-network modeling and how pore-networks are constructed. Next, pore-network modeling applications in reactive transport and mineral dissolution problems are presented. Finally, strategies for merging of overlapping pores are discussed.

2.3.1.1 History and applications

Interest in pore-scale models, including PNM, had decreased by the early 1990s due to the necessity for more profound understanding of flow and transport phenomena in porous media by oil companies, not yet possible to investigate using such a fundamental approach [45]. However, significant improvements of model capabilities, advances in numerical methods, increase of computer speed, and the development of techniques to represent adequately the complex porous space and topology of porous media, made pore-network modeling a reliable method to predict a wide range of phenomena at the pore-scale.

For example, the first physically-based pore-scale model of wettability was proposed by KOVSCEK *et al.* [44] that develop a pore-level picture of how mixed wettability might form and evolve in reservoir rock initially filled with brine. In addition to the role of thin water-in-oil and oil-in-water emulsion films, their study incorporates cornered pores, pore convexity, contact angle pinning, and explicit pore-size distributions.

The development of three-phase flow modeling also has started to improve to extend understanding in wettability and relative permeability behaviors in more complex and realistic systems [48, 49]. Enhanced oil recovery processes usually involve the flow of three phases, where a gas phase (natural gas and CO_2 , for example) is injected into a reservoir containing water and oil phases. Mechanistic modeling of these processes offers an appealing alternative to empirical models and direct measurements, that are otherwise difficult and time-consuming to obtain [49, 45].

In summary, pore-network models are an efficient approach to account for various phenomena occurring at the pore scale and they have been widely used to study multiphase flow in porous media [45, 50, 44], biofilm growth [51], adsorption phenomena [52], membrane fuel cells [53, 54], and chemical and biological processes, including precipitation and dissolution processes that are discussed further in this section.

2.3.1.2 Pore-network construction

Pore-network models are commonly constructed based on an idealized description of the pore spaces, where pores are defined as the larger void spaces that are connected to each other by narrower void spaces called throats. In order to be considered a successful technique to simulate flow and transport in porous media, however, pore-network models should reproduce the main morphological and topological characteristics of the real porous medium for a given application [28]. Some of these properties include pore-size distribution, coordination number, connectivity, and conductance of the throats [23].

Importantly, one of the challenges in obtaining credible results is the identification of characteristics relevant to the modeled process in order to reduce the computational load by neglecting less relevant information [55, 41]. For example, while cornered pores are essential to construct a representative system to study multi-phase problems, this feature is not a restriction for single-phase problems. This is because angular corners retain the wetting phase while the non-wetting phase occupies the center of the porous element, and as a consequence two or more fluids are able to flow simultaneously through the same pore space [56, 57].

Considering this, three main approaches have been proposed to construct a pore network model representative of a porous medium [41]. The first approach is to construct a statistically equivalent network using distributions of relevant morphological and topological properties of a real porous medium. Statistical reconstruction methods are quite general. They require properties derived from two-dimensional (2D) images and, considering that thin sections are often readily available, a wide variety of porous media may be described effectively [58, 41]. Some of the studies that used this approach to explore reactive transport problems are LI *et al.* [23], ALGIVE *et al.* [37], RAOOF [28], KIM and LINDQUIST [59], and BEKRI *et al.* [39].

The second method is to construct a pore network model directly onto a specific void space of a porous medium. Various methods have been developed to extract the void spaces from three-dimensional images. The medial axis algorithm is one of the methodologies that transform the pore space images into a medial axis, constructing a topological skeleton along the middle of the

pore channels [60]. The maximal ball algorithm, conceptualized by SILIN and PATZEK [61] and further improved by AL-KHARUSI and BLUNT [62], aims to find the largest inscribed spheres centered on each voxel of the image that just touch the boundary, that represents the grain. The largest maximal balls that are surrounded by smaller balls define the pores. GOSTICK [63] used the technique of watershed segmentation to extract the pore-network model from high-porosity materials.

The third approach is based on the diagenesis of porous media, a geological process based on the explicit modeling of the geological rock forming processes, and it is called the grain-based approach. For carbonate rocks, however, this technique is not suitable as carbonate systems are not modeled [41]. More detailed information about the the main general approaches to construct representative pore-network models is found in XIONG *et al.* [41].

2.3.1.3 Pore-network modeling of reactive transport

HOEFNER and FOGLER [64] pioneered the use of pore network modeling to study dissolution of porous media and to evaluate qualitatively the formation of wormhole channels based on the Damköhler number. FREDD and FOGLER [34] went beyond and combined effects of transport and reaction to predict wormhole structure by using two-dimensional networks and also a three-dimensional physically representative network based on packed-bed representation of the porous medium. Note that in both studies, mixing occurs only in the pores and only throats are allowed to grow due to dissolution. BUDEK and SZYMCZAK [65], then, extended these works by introducing dynamically changing topology of the network as the dissolution proceeds. This is the first study that considers merging of pore spaces, allowing more realistic representation of the dissolving porous medium. It is noteworthy that their model pores are defined just as node points for pressure determination and during the pore-merging step, the reactive surface of the merged throat is conserved, but the volume is not.

Scaling and mineral spatial distributions effects in geochemical reaction rates were also studied by using pore-network modeling [23, 66]. Sandstone dissolution processes were simulated in individual pores that do not have prescribed

geometries; they are defined only in terms of surface area and volume. Also, throats are not defined and an effective resistance to flow and an effective cross-sectional area for diffusion are assigned to each pore-to-pore connection. Simulations were run in regular 3D networks and, importantly, geometry changes were not taken into account. Instead, changes in species concentration over time were used to evaluate the reactive transport. These works were extended to consider the use of computed tomography data to capture the mineral distribution in the samples [67] and to consider geometry and topology changes, associated with data from real rocks [59].

Permeability and porosity evolution due to dissolution and precipitation of carbonates using reactive transport modeling in pore networks were studied by NOGUES *et al.* [68]. The model predicted evolution of pore sizes and pore-to-pore conductivities, and the effects of different flow conditions on the evolving of petrophysical properties were explored. They showed that the use of a power-law with a single exponent parameter may not capture the correct relation between the evolving of porosity and permeability.

RAOOF *et al.* [24] introduced the application of governing mass balance equations for solute transport, considering pores and throats as control volumes. For this, a pore-network model was used to discretize the continuum porous structure as a network of pore bodies and pore throats, both with finite volumes, and with a wide range for the distribution of pore coordination numbers (1-26). Reactive transport in wellbore cement under CO_2 storage conditions was explored considering diffusion as the only transport mechanism. Notably, a pore-network modeling tool capable of simulating fluid flow and multi-component reactive transport under variably saturated conditions, PoreFlow, is introduced by RAOOF *et al.* [69]. The many modules available in this tool include a geochemical package [70], possibility for accounting the evolving of porosity and permeability, and a pore network generator [71], that has as one of the main features the possibility of throats be oriented in 13 different directions, allowing a maximum coordination number of 26.

ALGIVE *et al.* [37, 5] and BEKRI *et al.* [39] used pore-network models to investigate changes in petrophysical properties in the presence of reactive fluid based

on permeability-porosity relationships for different flow conditions and also investigated different dissolution regimes for the case of deposition in porous media. The approach of their studies considers that the system is not very far from chemical equilibrium and that the asymptotic regime has been reached. In this way, the solute concentration undergoes an exponential evolution with time and moment theory is applied to determine the macroscopic transport coefficients of the transport equation.

TANSEY and BALHOFF [25] studied dissolution of a porous medium due to a reactive single-phase transport in the mass-transfer-limited regime also using pore-network modeling. Simulations were conducted on random close-packed arrangements of spheres, where the mass balance equation was solved for pore-bodies only and no phase diagram was explored. Merging of pores was taken into account in their study.

More recently, DASHTIAN *et al.* [72] developed a general framework to simulate reactive transport in two- and three-dimensional porous media to evaluate the effects of throat dissolution on petrophysical properties. Their approach assumes that pores are volumeless, the pressure field is constant, and no topology changes occur.

2.3.1.3.1 Merging techniques

Dissolution of significant amounts of solid leading to merging of pores and throats to form vug-like pores is an open question in systems with significant mineral reactivity. The appropriate treatment of pore merging allows a better representation of the physical problem and makes possible the use of reactive transport simulations to evaluate dissolution regimes in more complex network topologies, derived from real porous media where the merging of pores is likely to occur due to the heterogeneous distribution of pore sizes within these type of porous media.

BUDEK and SZYMCZAK [65] performed the first pore-network study that considered a merging approach during reactive transport and mineral dissolution. The porous medium is represented by a two-dimensional triangular net-

work of cylindrical tubes. The points where the tubes meet are referred as nodes. In this way, pores are defined just as node points for pressure determination. Then, throats are tubes that enlarge during the dissolution process. Note that a single reaction is assumed to describe approximately the carbonate dissolution.

Their methodology for merging considers that, as the diameters of the eroding throats become comparable to the interpore distances, the throats are joined together. The assumption is that the new throat has the same diameter as the sum of the diameters of the original two throats. With this, the reactive surface area is conserved during the merging process, but the volume is not.

TANSEY and BALHOFF [25] developed a pore network model of heterogeneous reactive transport and matrix dissolution that considers a pore-merging criterion to improve the pore-scale physics of the network. Simulations were conducted on random close-pack arrangements of spheres and the transport equation assumes pores as the only control volumes. Throats represent the conductances throughout the network. This approach also assumes the tracking of only one chemical species and the reactive transport equation is solved explicitly.

During simulation, pores grow assuming a static geometry by preserving the relation between surface area and volume. Throat cross-section areas are updated based on the the new surface area of the connected pores. Throat conductances are then updated based on the new cross-sectional areas, also assuming a static geometry using a shape factor to map the throat shape onto a cylindrical tube and preserving initial relationships between throat cross section and conductivity.

The merging approach developed by TANSEY and BALHOFF [25] assumes that the two original pores are merged in one new pore when an overlap of pore bodies of around 10% is reached. The new merged pore's volume is equal to the combined volume of both original pores.

The use of a merging criterion was found to be quite important to capturing the formation of preferential pathways, because with no merging of overlapping pores, permeability could not increase past a small fraction of its potential, reaching a plateau, and no occurrence of wormholes [25].

Clearly, significant insights and improvements were made by these studies,

although some strong simplifications were assumed related to the evolution of geometry during dissolution and merging processes. Assuming static relations between surface areas and volumes may not be the best representation for all the different dissolution regimes. Depending on the fluid and reactivity conditions, dissolution can affect differently the porous spaces and change the relation between surface areas and volume, specially for pores that considers the contact area of all connected throats to determine the available surface area for reaction.

The conservation of geometry and flow properties during the application of a merging strategy is paramount to maintain a continuous evolution of the porous media due to the dissolution process. The structure of the network before and after the merge of two overlapping pores must represent better the real physical problem, rather than include more unrealistic simplifications.

Maintenance of the available reactive surface area and volume of the overlapping pores, as well as conductivity of the connected throats, are essential for an accurate evaluation of the dissolution regimes, because transport phenomena and reaction within the pore spaces are very dependent on these properties.

Note that, as well stated by TANSEY and BALHOFF [25], the merging of a huge amount of pores is unlikely to produce an accurate depiction of void space. Although considering a merging criterion brings more accuracy to the model, each merging introduces many simplifying assumptions for the geometry and location of the new merged pore, and the merging approach is not meant to extrapolate accurately *ad infinitum*.

Chapter 3

Construction of behavior diagrams and the novel quantitative criteria

The content of this chapter reproduces the work of ESTEVES *et al.* [29] published in the *Advances in Water Resources* journal.

In the remainder of this chapter, we first present the objectives and main contributions of this study. Then, the construction of the pore-network models is presented. Governing equations of the pore-network model that simulates reactive transport and mineral dissolution, as well as the computational implementation of these equations and the pore-networks selected for this study are described. Finally, we present the simulation results and discuss the regimes observed. We close with a summary of the main highlights of this work.

3.1 Objectives and contributions

The main objective of this study is to understand the occurrence of different dissolution regimes in a porous medium subject to various reactive flow conditions during single-phase flow relevant to geological sequestration of CO_2 using the pore-network modeling approach. Modeling of the pore-scale phenomena involved in reactive flow through porous media is an important step towards understanding the changes in permeability and porosity as well as the different dissolution patterns observed at larger scales.

The main contribution of this work is to identify different dissolution regimes

in a phase-diagram format, based on dimensionless numbers, using a complete pore-network model that takes into account species mass balance inside pore and throat volumes, as well as the evolution of pore-space geometry and network flow field during reactive transport simulations. Qualitative criteria are often used to evaluate different dissolution patterns, including evolution of acid concentration, network geometry, fluid volumetric flow rate and porosity-permeability relationship. Here, quantitative criteria based on standard deviation analysis are introduced to classify the regime by interpreting acid distribution within pore space.

3.2 Methodology

Methodology starts with the pore-network models construction. The governing equations of the reactive transport problem with dissolution of the porous medium are presented as follows: pressure field determination, mass balance equation, simplified kinetic approach, the geometry update, standard deviation criterion for interpreting acid distribution, and dimensionless numbers. All units of measurement used in this study are in accordance with the International System of Units (SI).

3.2.1 Pore-network models construction

Porous media are investigated using two- and three-dimensional (2D and 3D) cubic pore-network models. The pores are characterized as spherical and are connected to each other by cylindrical throats with circular cross-sections. The size of the pores respect a uniform distribution and the size of the throats are related to the size of the pores connected to them. Throat diameters were defined as 1/4 of the diameter of the smallest pore connected to a throat and inter-pore distances are equal. Pore walls are assumed to be composed of a single mineral such as calcite.

A more complex network derived from a real carbonate rock sample is also presented. This pore network, composed of 8508 pores and 10336 throats, is generated from micro-computed tomography (micro-CT) and was obtained from

a data set made available by Imperial College London in *Statoil* format [73].

Pore networks were constructed using OpenPNM, which is an open-source pore-network modeling package that is designed to be customized. Users can write their own pore-scale models or even use or edit some of the available routines [74]. Another feature of OpenPNM is the possibility to generate cubic and random networks, in the most varied pore and throat size distributions. It is also possible to import networks from different formats.

3.2.2 Pressure field

In order to obtain the pressure field of the network, we consider the pseudo steady-state flow of a single-phase incompressible fluid, in which the mass conservation for each pore is given by

$$\sum_{j=1}^z q_{ij} = 0 \quad \forall i, \quad (3.1)$$

where z is the coordination number, j represents the pore connected to pore i , and q_{ij} is the volumetric flow rate through throat ij . The volumetric flow rate through a pore-throat is determined by the pressure difference between the connected pores i and j ($P_i - P_j$) and the throat conductance (c_{ij}), as follows:

$$q_{ij} = c_{ij} (P_i - P_j). \quad (3.2)$$

The throat conductance is obtained by use of Poiseuille's law for laminar flow in a cylindrical tube:

$$c_{ij} = \frac{\pi r_{ij}^4}{8\mu l_{ij}}, \quad (3.3)$$

where r_{ij} is the radius of throat ij cross-section, μ is the dynamic viscosity of the fluid and l_{ij} is the length of the throat ij . Substituting Eqs. (3.2) and (3.3) into Eq. (3.1), a linear algebraic system for the unknown pressure field is solved for the pressure in each pore.

To determine the pseudo steady-state flow field of the network, constant volumetric flow rate at the inlet boundary and fixed pressure at the outlet boundary are imposed. Also, to determine the absolute permeability, fixed pressures are imposed at the inlet and outlet boundaries. All other boundaries are closed, therefore both systems result in a one-dimensional flow problem. Considering the last case, the total flow rate through the network (Q) is obtained after pressure field determination and Darcy's law is used to calculate the absolute permeability (K) of the system, as described below

$$K = \frac{\mu QL}{A\Delta P}, \quad (3.4)$$

where A is the cross-sectional area of the network and L is the length of the network.

3.2.3 Concentration field

The reactive transport and dissolution problem is described by the mass balance in all available pore spaces, pores and throats, and is deduced from the mass conservation equations of the chemical species [75]. Deduction of the mass balance equation for pores and throats are presented in Appendix A.

The transport of a chemical species occurs by advection and diffusion. For a control volume represented by pores, the mass balance equation for chemical species α in pore i is

$$\frac{d}{dt}(C_{\alpha,i}V_i) = \sum_{ij,in} C_{\alpha,ij}q_{ij} - C_{\alpha,i} \sum_{ij,out} q_{ij} + \sum_{ij} A_{ij}D_{\alpha} \left(\frac{C_{\alpha,ij} - C_{\alpha,i}}{0.5l_{ij} + r_i} \right) - R_{\alpha,i}A_{r,i}, \quad (3.5)$$

where t is the time, $C_{\alpha,i}$ is the mass concentration of species α in pore i , $C_{\alpha,ij}$ is the mass concentration of species α in throat ij , V_i is the volume of pore i , A_{ij} is the cross-sectional area of throat ij , \mathcal{D}_α is the diffusion coefficient of species α , r_i is the radius of pore i , $R_{\alpha,i}$ is the reaction rate of species α due to heterogeneous chemical reaction in pore i and $A_{r,i}$ is the reactive surface area of pore i . On the right-hand side, the first two terms take into account advective mass inflow rates, represented by the mass that arrives in pore i from connected throats ij , and advective mass outflow rate, represented by the mass that leaves pore i through throats ij ; the third term describes the mass change rate due to diffusion between pore i and all connected throats ij ; and the last term describes the mass change of species α due to heterogeneous chemical reaction that occurs in the available reactive surface area of pore i .

The mass balance equation for species α in throat ij is

$$\frac{d}{dt}(C_{\alpha,ij}V_{ij}) = (C_{\alpha,i} - C_{\alpha,ij})q_{ij} + A_{ij}\mathcal{D}_\alpha \left(\frac{C_{\alpha,i} - C_{\alpha,ij}}{0.5l_{ij} + r_i} \right) + A_{ij}\mathcal{D}_\alpha \left(\frac{C_{\alpha,j} - C_{\alpha,ij}}{0.5l_{ij} + r_j} \right) - R_{\alpha,ij}A_{r,ij}, \quad (3.6)$$

where $C_{\alpha,i}$ is the mass concentration of species α in the pore from where the flow is arriving in the throat ij (see Fig. 3.1) and $A_{r,ij}$ is the reactive surface area of throat ij . On the right-hand side of Eq. (3.6), the first term takes into account the mass change due to advection between the inlet and the outlet zones of throat ij , that are described by the mass of species α that arrives in throat ij from the connected pore i or j , depending on the flow direction. The inflow concentration is represented by $C_{\alpha,in}$, and the mass of α that leaves throat ij in the direction of the other connected pore is $C_{\alpha,ij}$. The second and third terms represent the mass change rate by diffusion phenomena between the throat ij and the connected pores i and j , respectively. The last term presents the mass change of species α due to heterogeneous chemical reaction that occurs in the available reactive

surface area of throat ij .

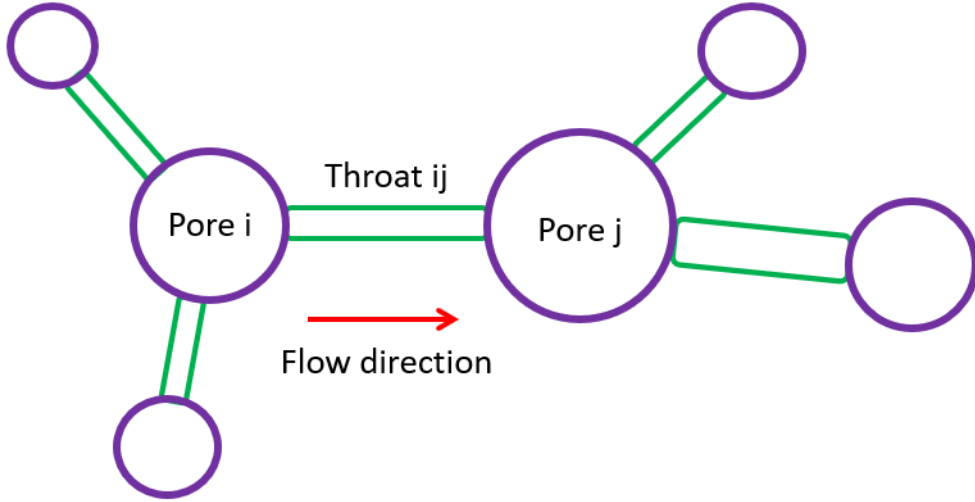


Figure 3.1: Scheme of throat ij and the connected pores i and j relevant to the mass balance inside throats.

In our approach, the concentration field is solved implicitly and the volume explicitly in a sequential algorithm. In other words, the system is solved for the new concentrations based on the previous geometry. The linear system for the unknown concentrations of species α is solved by the direct method `spsolve` from the SciPy library [76].

The domain initial condition and the inlet boundary condition are represented by a fixed value of species concentration, as presented below, respectively:

$$C_{\alpha,i} |_{t=0} \text{ and } C_{\alpha,ij} |_{t=0} = C_{\alpha,0} = \text{constant}, \quad (3.7)$$

$$C_{\alpha,in} |_{\forall t} = C_{\alpha,in} = \text{constant}, \quad (3.8)$$

where $C_{\alpha,in}$ is the mass concentration of species α in the inlet pore spaces (pores and throats).

The outflow boundary condition is used as the boundary condition for the

outlet pores. The solute flows out of the outlet pore at a rate that is the product of the total volumetric flow rate and the solute concentration in the outlet pore. This is implemented by adding a sink term in the mass balance equation for the outlet pores, as follows

$$c_{\alpha,out}q_{i,out} \big|_{\forall t}, \quad (3.9)$$

where $c_{\alpha,out}$ is the mass concentration of species α in the outlet pore *out* and $q_{i,out}$ is the total volumetric flow rate that arrives in each outlet pore *out*.

3.2.4 Dissolution reactions

During the dissolution process, porous medium geometry evolves with heterogeneous chemical reactions at the available reactive surfaces of pores and throats.

For simplicity, reactive surfaces are represented by the presence of only one mineral, that is dissolved by the presence of an acid species. This approach represents, in a simplified way, the acidization processes where hydrochloric acid (HCl) is injected in carbonate rocks, represented by calcite ($CaCO_3$), as follows



Because the acid is the only component in the aqueous phase that reacts with the solid mineral, it is the only chemical species concentration that needs to be tracked. If needed, the concentrations of the other species can be determined by stoichiometric relationships. Note that the rate-limiting reaction is the acid attack on calcite, and it is assumed that carbonate equilibria is totally shifted toward $CO_{2(aq)}$ due to the large acid concentration in the system. Thus, a single reaction rate is enough to represent our problem. This approach follows from the work of SOULAINÉ *et al.* [6] and others [65, 25]

3.2.5 Geometry update

As our solution involves geometry changes, at each time step during the simulations, volumes of pores and throats are changed. In this way, at each time step, with the solution of the concentration field based on mass balance, the change in volume of the pore spaces is obtained using the relation between the solid consumed on the reactive surface of each pore space and the density of the reactive mineral that composes the porous medium.

Considering a first-order reaction rate for the heterogeneous chemical reaction and a stoichiometric coefficient in mass basis that relates the consumption of the hydrochloric acid ($\alpha = a$) and the consumption of the reactive mineral, the change in volume of the solid as a function of time is given by:

$$\frac{\delta V_i^d}{\delta t} \simeq \frac{R_{a,i} A_{r,i}^n \beta}{\rho_s} = \frac{\left(k_r C_{a,i}^{n+1,*}\right) A_{r,i}^n \beta}{\rho_s}, \quad (3.11)$$

$$\frac{\delta V_{ij}^d}{\delta t} \simeq \frac{R_{a,ij} A_{r,ij}^n \beta}{\rho_s} = \frac{\left(k_r C_{a,ij}^{n+1,*}\right) A_{r,ij}^n \beta}{\rho_s}, \quad (3.12)$$

where β is the stoichiometric coefficient that relates the acid consumption to the consumed reactive mineral, ρ_s is the density of the solid reactive mineral, k_r is the kinetic constant of the heterogeneous chemical reaction, and δV_i^d and δV_{ij}^d are the change in volume of pores and throats due to mineral dissolution.

Based on the consumed volume, Eqs. (3.11) and (3.12), it is possible to relate these volume changes to the increase of pore radii (δr_i^d) of a sphere with radius r_i and to the estimation of the increase of throat radii (δr_{ij}^d) of a cylinder with radius r_{ij} and length l_{ij} , as presented below:

$$\delta r_i^d = \frac{\delta V_i^d}{4\pi r_i^2}, \quad (3.13)$$

$$\delta r_{ij}^d = \frac{\delta V_{ij}^d}{2\pi r_{ij} l_{ij}}. \quad (3.14)$$

At the junction of the throat with each pore, this procedure double counts the dissolution of the volumes presented below:

$$\delta V_{i,ij} = 2\pi r_{ij} \delta r_i \delta r_{ij}, \quad (3.15)$$

$$\delta V_{j,ij} = 2\pi r_{ij} \delta r_j \delta r_{ij}, \quad (3.16)$$

where $\delta V_{i,ij}$ and $\delta V_{j,ij}$ are the volumes doubly dissolved by throat ij and the connected pores i and j , respectively. Considering this information and the premise that double dissolution is maintained, the new pores and throats volumes are determined, respectively, by

$$V_i^{n+1} = V_i^n + \delta V_i^d + \sum_{ij} \delta V_{i,ij}, \quad (3.17)$$

$$V_{ij}^{n+1} = V_{ij}^n + \delta V_{ij}^d - \delta V_{i,ij} - \delta V_{j,ij}. \quad (3.18)$$

The pore volume is defined considering the volume of a sphere and, consequently, the updated radius of the pore is calculated as

$$r_i^{n+1} = \sqrt[3]{\frac{3V_i^{n+1}}{4\pi}}. \quad (3.19)$$

The change in pore radius, more precisely, the increase in pore radius as a conse-

quence of the dissolution process, affects the length of the throats of the network because the pore volume invades part of the volume that previously belonged to the connected throats. The change in throat length caused by the changes in connected pores radii is given by

$$l_{ij}^{n+1} = d_{ij} - r_i^{n+1} - r_j^{n+1}, \quad (3.20)$$

where d_{ij} is the distance between the centers of two connected pores i and j (interpore distance). The volume of the throats are obtained considering the control volume as a cylinder. Given the updated throat length, it is possible to determine the throat radius, using Eq. (3.21)

$$V_{ij}^{n+1} = \pi \left(r_{ij}^{n+1} \right)^2 l_{ij}^{n+1}. \quad (3.21)$$

New throat available reactive area and cross-sectional area are obtained, respectively, by

$$A_{r,ij}^{n+1} = 2\pi r_{ij}^{n+1} l_{ij}^{n+1}, \quad (3.22)$$

$$A_{ij}^{n+1} = \pi \left(r_{ij}^{n+1} \right)^2. \quad (3.23)$$

Considering the inlet and outlet areas of each pore defined by the sum of the spherical cap surfaces formed between the pore i and all connected throats ij (Eq. (3.24)), it is possible to determine the available reactive surface area of each pore, as presented below:

$$A_{i,ij}^{n+1} = 2\pi r_i^{n+1} \left[r_i^{n+1} - \sqrt{\left(r_i^{n+1} \right)^2 - \left(r_{ij}^{n+1} \right)^2} \right] \quad (3.24)$$

$$A_{r,i}^{n+1} = 4\pi \left(r_i^{n+1} \right)^2 - \sum_{ij} A_{i,ij}^{n+1}, \quad (3.25)$$

where $A_{i,ij}$ is the surface area of the semi-sphere formed by pore i and throat ij .

Finally, based on the updated mass of acid inside pores and throats, as described below

$$m_i^{n+1} = C_i^{n+1,*} V_i^n, \quad (3.26)$$

$$m_{ij}^{n+1} = C_{ij}^{n+1,*} V_{ij}^n, \quad (3.27)$$

the acid concentration is updated based on the new volumes obtained by the geometry update as

$$C_i^{n+1} = \frac{m_i^{n+1}}{V_i^{n+1}}, \quad (3.28)$$

$$C_{ij}^{n+1} = \frac{m_{ij}^{n+1}}{V_{ij}^{n+1}}. \quad (3.29)$$

The above procedure is repeated for each time step and, because of this, it is possible to evaluate the evolution of the permeability and also the pore space during the simulation of the reactive transport coupled with dissolution process.

3.2.6 Implementation

The base-algorithm from OpenPNM used for the implementation of the reactive transport and dissolution process was the 'TransientReactiveTransport' algorithm, designed to account for advection, diffusion, and reaction phenom-

ena considering just pores as control volumes and without considering geometry changes during simulations. In this way, the main improvements implemented by this work are related to considering pores and throats as control volumes and also considering geometry updates due to heterogeneous chemical reaction at each time step of the simulations.

The final and more complex algorithm follows the steps described below:

1. Network construction and geometry definition.
2. Fluid and solid properties definition.
3. Definition of flow and kinetic parameters.
4. Definition of initial and boundary conditions.
5. Determination of the network pressure field using Eq. (3.1) and its permeability by (3.4).
6. Set up the sparse linear system of equations constructed based on the pores and throats mass balances.
7. Solution of the sparse linear system.
8. Determination of the consumed volume of pores and throats using, respectively, Eqs. (3.11) and (3.12).
9. Determination of the double dissolved volumes using Eqs. (3.15) and (3.16).
10. Update the volume of pores and throats using Eqs. (3.17) and (3.18).
11. Geometry update:
 - (a) Determination of the new pore radii using Eq. (3.19).
 - (b) Determination of the new throat lengths using Eq. (3.20).
 - (c) Determination of the new throat radii using Eq. (3.21).
 - (d) Determination of the new reactive surface areas and cross-sectional areas of throats by using, respectively, Eqs. (3.22) and (3.23).

- (e) Determination of the new reactive surface area for pores using Eq. (3.25).
12. Update the hydraulic conductance, Eq. (3.3), considering the updated geometry.
 13. Update the new acid mass concentration using Eqs. (3.28) and (3.29)
 14. Return to step 5 and repeat until the algorithm reaches the final time step.

3.2.7 Dimensionless numbers

The use of dimensionless numbers in reactive transport aims to generalize predictions and results across a range of transport and reaction rate conditions. Problems involving reactive transport usually take into account Reynolds (Re), Péclet (Pe), Damköhler (Da) and Péclet-Damköhler ($PeDa$) numbers to characterize different dissolution patterns. The definitions used in this work are based on SOULAINÉ *et al.* [6] and calculated at the initial time. Reynolds number (Re) expresses the ratio of inertial effects to viscous forces and it determines the character of the flow (laminar, turbulent, and transient flows) and is given by

$$Re = \frac{\rho_f v_0 \sqrt{K}}{\mu_f}, \quad (3.30)$$

where ρ_f is the fluid density, v_0 is the interstitial velocity, \sqrt{K} is the square root of the permeability of the porous medium, and μ_f is the fluid dynamic viscosity.

The Péclet number (Pe) is defined as the ratio of the advection rate to the rate of diffusion of a chemical species, as

$$Pe = \frac{v_0 \sqrt{K}}{\mathcal{D}_\alpha}, \quad (3.31)$$

where \mathcal{D}_α is the diffusion coefficient of species α . The Péclet-Damköhler ($PeDa$) is defined as the ratio of the reaction rate and the diffusive mass transfer rate, as

$$PeDa = \frac{k_r}{A_{ss}\mathcal{D}_\alpha}, \quad (3.32)$$

where k_r is the constant of reaction and A_{ss} is the specific surface area of the porous medium, defined as the ratio of reactive surface area of all pores and throats to the total porous volume. Finally, the Damköhler number, Da , that represents the ratio of the reaction rate to the rate of advection, is defined as the ratio of the $PeDa$ and Pe numbers, as

$$Da = \frac{k_r}{v_0\sqrt{K}A_{ss}}. \quad (3.33)$$

3.2.8 Statistics and regimes classification

Statistical approaches are useful for extracting information from a given data set and to better understand observed patterns. In this way, the standard deviation of the logarithm of the acid concentration (σ) is used in this study as a quantitative criterion to define dissolution regimes. This parameter is a measure of the spread of a set of values, hence, the smaller the deviation the more homogeneous is the data set. Based on numerous observations of simulation results in cubic networks, and for the initial condition used in these tests ($c_{a,0} = 10 \text{ kg/m}^3$), the limit σ value to categorize a normalized data set as homogeneous was observed to be 1.

Therefore, two different measures are considered: the standard deviation of the acid concentration over all pores and throats of the network (σ_{net}) and the average of the standard deviations of each vertical cross-section of the network ($\overline{\sigma_{cross}}$). First, σ_{net} is evaluated. If $\sigma_{net} < 1$ the acid concentration is considered uniform through the network and the regime is classified as uniform. Other-

wise, the $\overline{\sigma_{cross}}$ is evaluated and if $\overline{\sigma_{cross}} < 1$ the acid concentration is considered to be uniform in each vertical cross-section of the network and the regime is classified as surface dissolution. Otherwise, the regime is classified as preferential pathways. The standard deviation criterion is obtained as

$$\sigma = \sqrt{\frac{1}{N} \sum_{n=1}^N \left(\log_{10} c_{A,n} - \overline{\log_{10} c_{A,n}} \right)^2}, \quad (3.34)$$

where N is the number of pores and throats that are evaluated and $\overline{\log_{10} c_{A,n}}$ is the mean value of the logarithm of acid concentration in the data set.

For the construction of the phase diagrams, the standard deviation analysis is evaluated for 100 networks with the same size distribution and considering the same flow and reactive parameters. In this way, it is possible for each dissolution regime to present the number of networks that respected the criterion proposed to identify the main patterns.

3.3 Results and discussion

Simulations of reactive transport are performed in different cubic networks to investigate dissolution regimes. The geometry of the simulation domains are based on the work of SONG *et al.* [77], who conducted dissolution experiments in a real rock micro-model directly etched in to a block of calcite, and of SOULAINÉ *et al.* [6], that conducted simulations of the dissolution process in a two-dimensional domain using a micro-continuum DBS approach. In this way, the networks used in this work consider a uniform distribution of the pore sizes, ranging from 300 μm to 900 μm .

A concentration of 10 kg/m^3 of acid is injected from the left-hand side of the network (one-dimensional flow in the positive x direction) at a constant volumetric flow rate corresponding to a $Re \approx 0.1$. Fluid and solid properties are set to $\mu_f = 10^{-3} Pa.s$, $\rho_f = 1000 kg/m^3$ and $\rho_{solid} = 2165 kg/m^3$. The stoichiometric coefficient that relates the consumed acid species with the consumed solid

reactive mineral is set to $\beta = 1$. All these properties are based on the work of SOULAINÉ *et al.* [6].

Simulations considered a range in Pe from 10^{-3} to 10^2 whereas the Da varied from 10^{-3} to 1. In order to obtain these wide ranges of dimensionless numbers, we considered diffusivity coefficients from 10^{-9} to as large as $10^{-4} \text{ m}^2\text{s}^{-1}$ and reaction rate constants from 10^{-6} to 10^{-3} m s^{-1} . Alternately, v_0 could have been varied to obtain the desired range of Pe and Da .

The final simulation time was set to 500 seconds and the time step size was fixed at 1 second. It is important to notice that simulations at the surface regime present a smaller simulation time than the other regimes, due to the limitation of the merging of pores and throats, not yet implemented at the time of this work. Also, Damköhler values were limited to avoid reactivity scenarios where the merging of pore spaces could happen. Likewise, greater reactivity might lead to the formation of a CO_2 phase due to the large amount of reaction product produced. Both of these were topics to be developed in future work. Importantly, the reactivities tested were sufficient to present behaviors of transport-limited processes. The results are discussed based on the pore volumes of injectant (PVI), defined by the ratio of the volumetric flow rate multiplied by the time upon the initial total porous medium volume.

Additionally, the last section presents extra simulations considering the carbonate network, including a comparison between our results and those available in the literature.

3.3.1 Identification of the dissolution regimes

A network composed of 10×10 pores is used to explore the different dissolution regimes and to construct phase diagrams based on the dimensionless numbers Pe , Da and $PeDa$. Figure 3.2 presents a scheme of the 10×10 network geometry. The simulation results show that, depending on the flow conditions and the mineral reactivity, different geometries and acid distributions can be observed after the dissolution process. These observations agree with previous literature [17, 7, 6, 18]. Three main dissolution patterns and two intermediate patterns are observed from reactive transport simulations: uniform dissolution,

surface dissolution, preferential pathways, transition zone, and mixed zone.

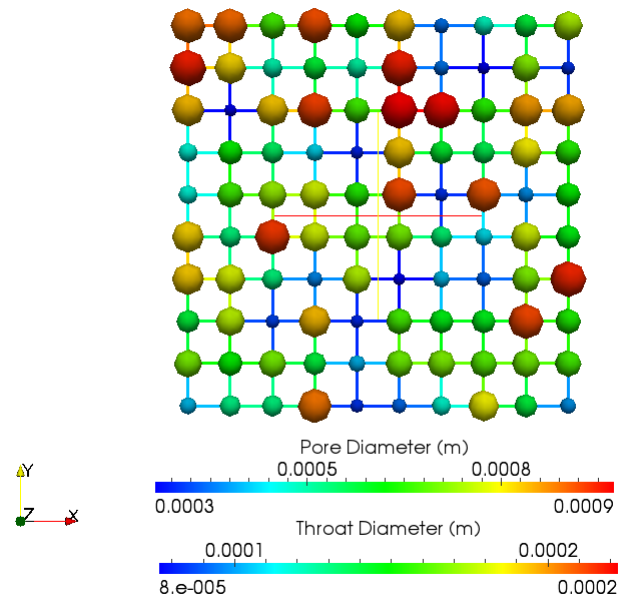


Figure 3.2: Pore and throat sizes of the cubic network composed of 10×10 pores.

The uniform dissolution pattern is related to significant acid penetration in the network. In this regime, the acid consumption rate is smaller than the transport by diffusion and advection, meaning that almost the entire pore space is filled with a uniform distribution of the acid (see Fig. 3.3).

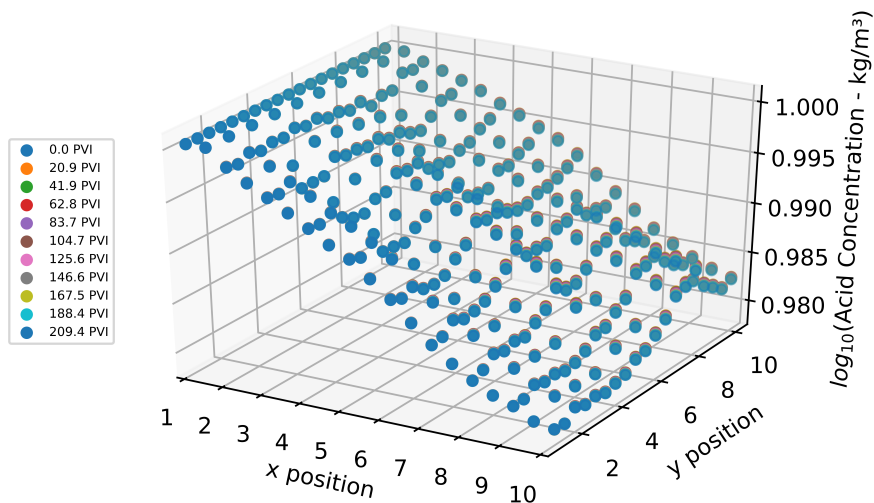


Figure 3.3: Evolution of the acid concentration as a function of PVI for pores and throats considering their x and y positions in the 10×10 network in the uniform dissolution I regime ($Pe = 0.00094$ and $Da = 0.00094$).

When a sufficiently large reactivity exists, the changes in pore-space geometry can be observed throughout the entire domain (see Fig. 3.4a). Otherwise, no

significant changes are observed throughout the network. This is a consequence of the availability of acid for all pore spaces of the network, that characterizes the reaction-limited feature of this dissolution regime. The volumetric flow rate starts to present changes for a $Da \approx 0.01$, that are more evident for throats with larger conductances (see Fig. 3.4b). The standard deviation based on acid concentration data from all pore spaces, σ_{net} , was determined for 100 networks and for 100% of the samples presented a value less than one, evidencing the uniform pattern of the regime.

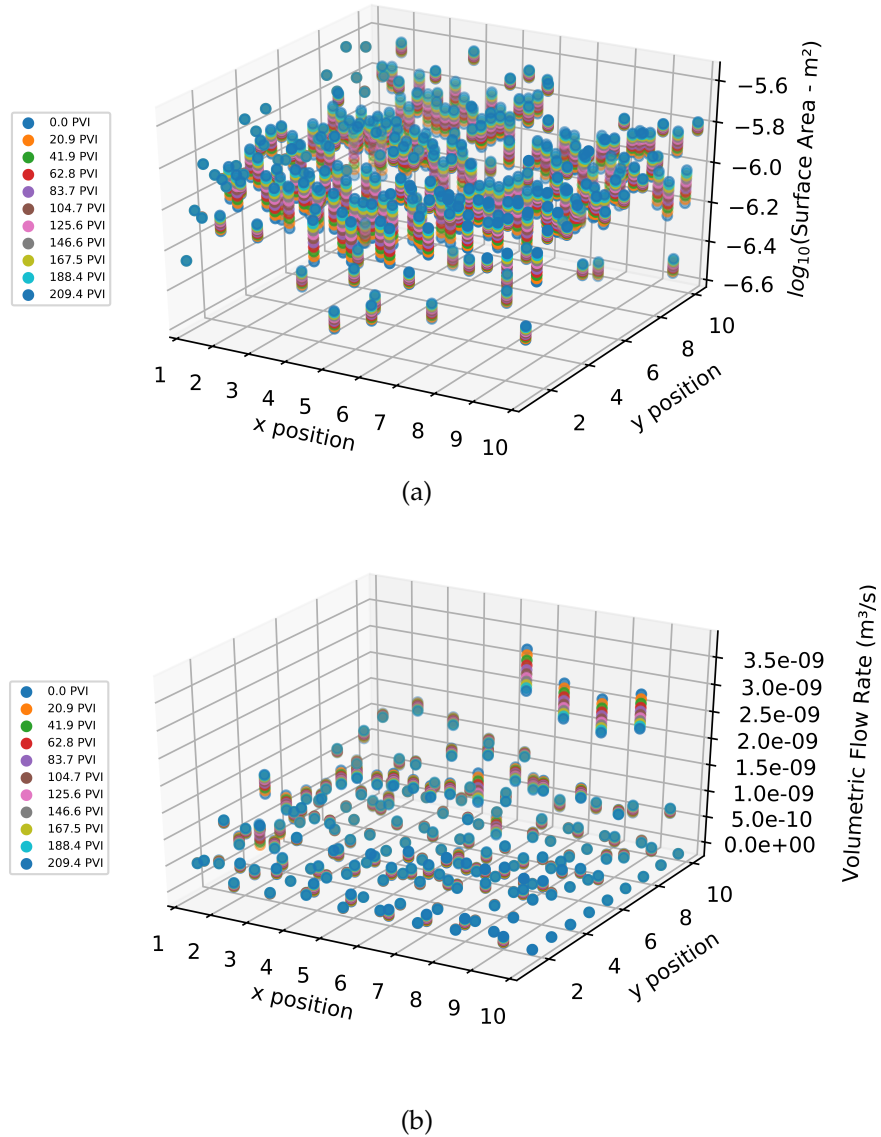


Figure 3.4: Simulation results from uniform dissolution II regime ($Pe = 0.00094$ and $Da = 0.0094$): (a) Evolution of the surface area as a function of PVI for pores and throats considering their x and y positions in the 10×10 network; and (b) Evolution of the volumetric flow rate as a function of PVI for throats considering their x and y positions in the 10×10 network.

The transition zone is characterized by the decrease of the acid penetration through the network and a concentration of the geometry changes in some portions of the domain due to the increase of the reactivity of the system as shown in Fig. 3.5. Regardless of the Péclet number in its Da range, this behavior is observed.

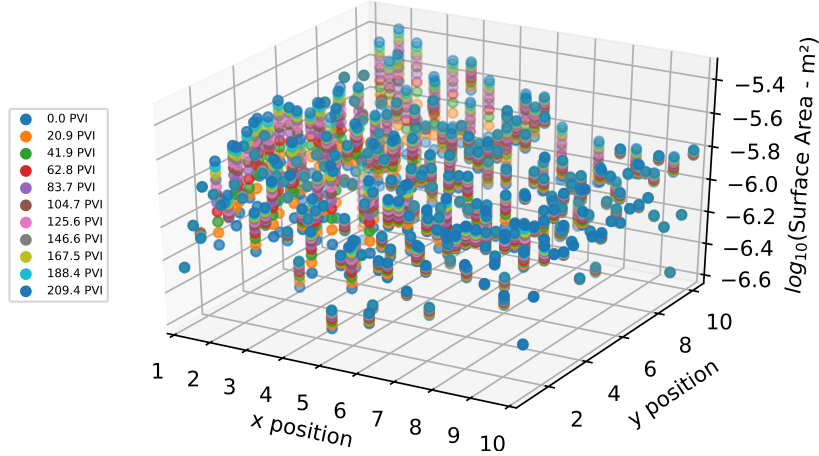
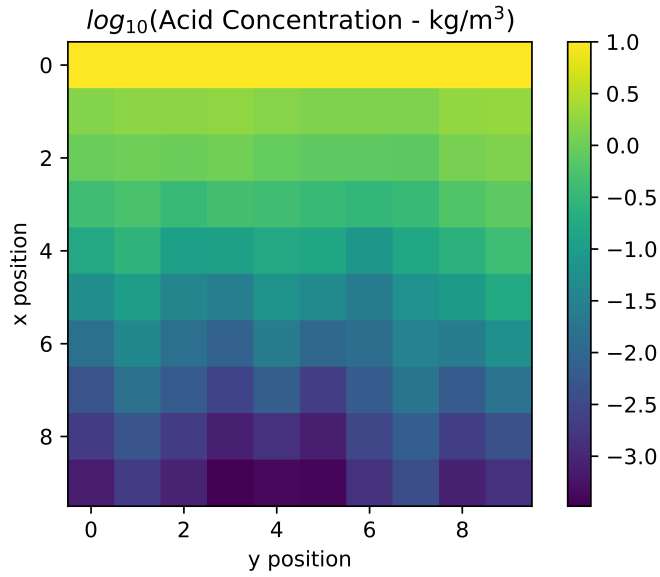
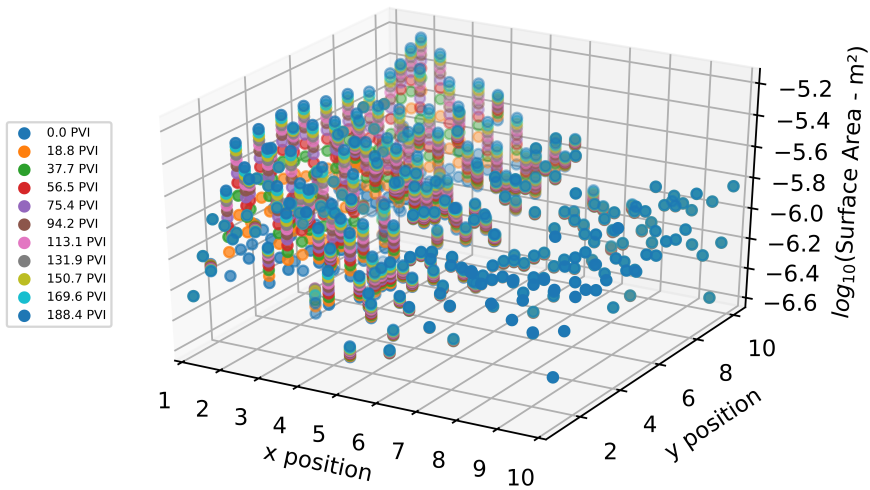


Figure 3.5: Evolution of the surface area as a function of PVI for pores and throats considering their x and y positions in the 10×10 network at the transition zone ($Pe = 94$ and $Da = 0.094$).

The surface dissolution pattern is characterized by an almost homogeneous acid concentration along the cross-sections perpendicular to the flow (see Fig. 3.6a). In this regime, the diffusion mechanism dominates over advective transport and reactivity of the acid is high, meaning that significant amounts of acid are consumed on the upstream pore spaces of the network thereby impairing the propagation of the acid through the entire porous medium. Because of this, the largest changes in geometry are observed for pores and throats located near the inlet area of the network (see Fig. 3.6b). The standard deviation analysis was evaluated and presented $\sigma_{net} > 1$ and $\overline{\sigma_{cross}} < 1$ for 100% of the samples. This confirms the uniform profile of acid concentration along cross-sections perpendicular to the flow.



(a)



(b)

Figure 3.6: Simulation results from surface dissolution regime ($Pe = 0.00094$ and $Da = 0.47$): (a) Final acid concentration profile (flow is from the top to the bottom); and (b) Evolution of the surface area as a function of PVI for pores and throats considering their x and y positions in the 10×10 network.

The mixed zone is characterized as a transition between surface dissolution and preferential pathways. In this regime, the homogeneity of acid concentration along vertical cross-sections starts to disappear, as well as other features of surface regime as shown in Fig. 3.7.

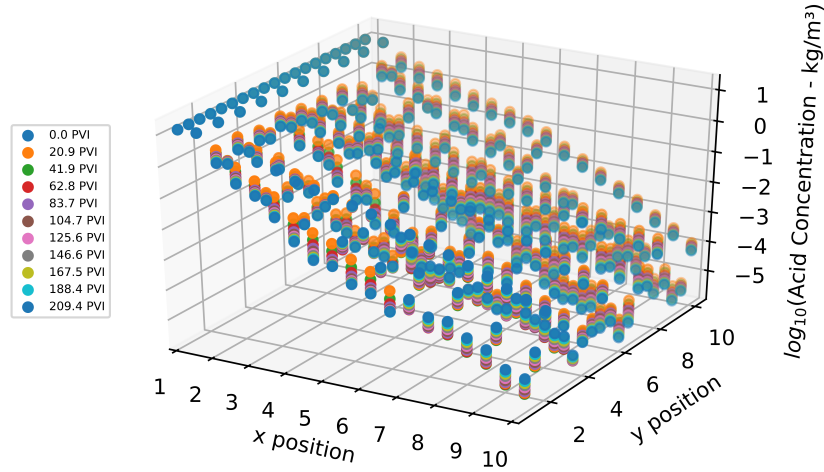


Figure 3.7: Evolution of the acid concentration as a function of PVI for pores and throats considering their x and y positions in the 10×10 network at the mixed zone ($Pe = 0.0094$ and $Da = 0.47$).

The preferential pathways are observed when advection is the strongest transport mechanism and the reactivity of the acid is high. Preferential pathways result from the heterogeneous geometry of the porous medium and consequent heterogeneous velocity profile. Because of this, more acid penetrates into the network through the more permeable pathways and no uniform patterns are observed (see Fig. 3.8). Furthermore, geometry changes in this regime are also more evident along the most permeable areas, as well as changes in volumetric flow rates. The standard deviation analysis presented $\sigma_{net} > 1$ for 100% of the samples and $\overline{\sigma_{cross}} > 1$ for 96% of the samples, evidencing the formation of preferential pathways through the domain.

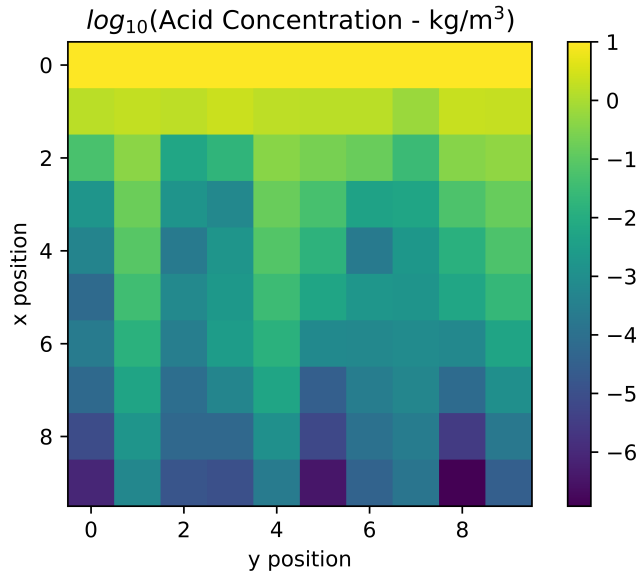


Figure 3.8: Simulation results from preferential pathway regime ($Pe = 94$ and $Da = 0.47$) in the 10×10 network: Final acid concentration profile (flow is from the top to the bottom). Note that pathways do not span the length of the domain.

Figure 3.9 presents the evolution of the relationship between normalized permeability and porosity for the three main dissolution regimes observed. For the uniform dissolution, a linear pattern is observed, independent of the mineral reactivity considered. This means that, besides the increase in porosity, absolute permeability of the porous medium also increases as a consequence of geometry changes in the entire network. A power law pattern is observed for the surface dissolution regime that can be interpreted as a restriction caused by the transport. Even with an increase of the porosity, the overall permeability does not increase at the same rate because the majority of the affected pores are in the inlet. A similar pattern is observed for preferential pathways, however with a smaller increase of the porosity when compared to the surface dissolution.

The difference in the increase of permeability for preferential pathways and surface dissolution regimes is explained by the extent of acid contact with solid throughout the entire network volume. After 209.4 PVI of injection, the pore spaces that have undergone dissolution by the presence of acid in the preferential pathways regime are less in volume than those affected in the surface dissolution regime (188.4 PVI), and also the uniform dissolution regime (209.4 PVI). That is, the fraction of the pore volume of the network that is affected by disso-

lution in the preferential pathways regime is less than the other two regimes and pathways do not span the sample. Figure 3.8, for example, is an image of the final acid concentration distribution in the preferential pathway regime. Note that the pathways do not span from the injection side to the production side.

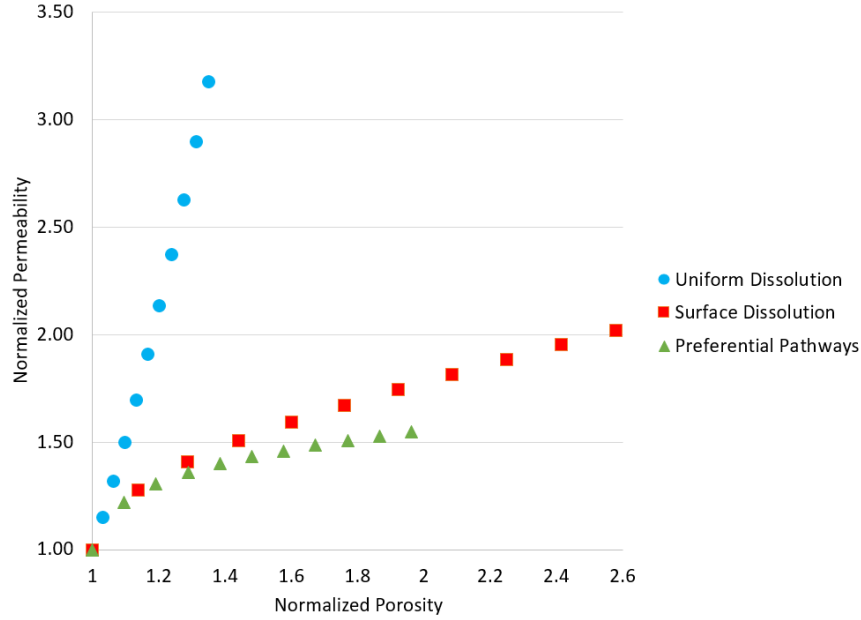
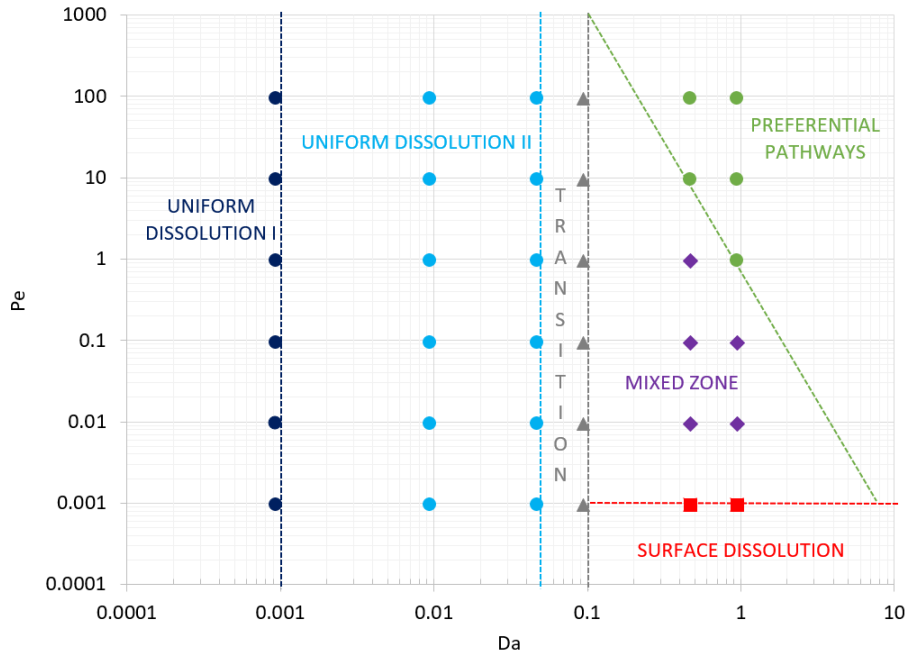


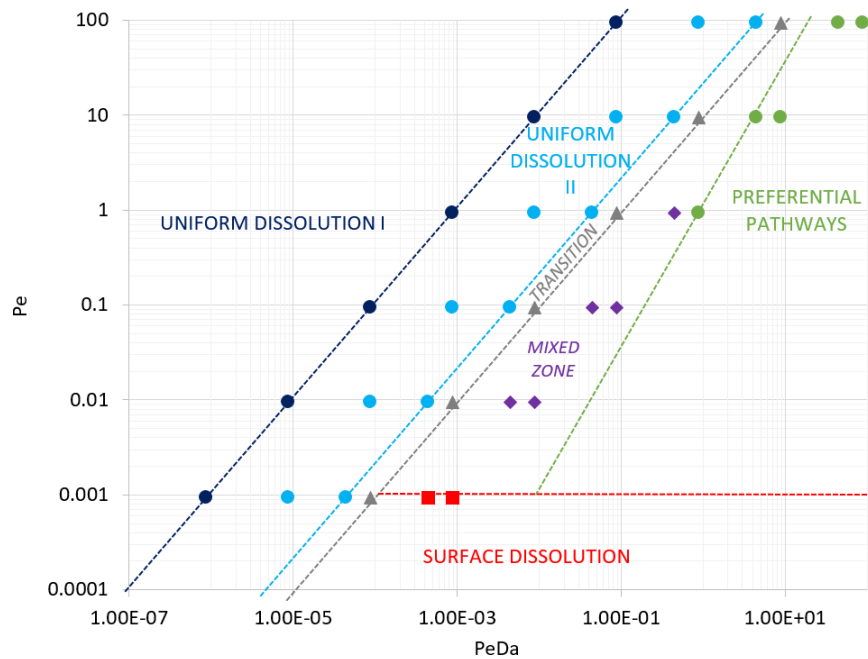
Figure 3.9: Evolution of the porosity-permeability relationship results from 10×10 network simulations.

3.3.2 Behavior diagrams construction

In order to summarize the different dissolution regimes observed in the reactive transport simulations conducted on the network composed by 10×10 pores, behavior diagrams are constructed based on the Pe , Da and $PeDa$ dimensionless numbers, as presented in Figures 3.10a and 3.10b. The main features of the diagrams agree well with literature results, especially when compared with the study of SOULAINÉ *et al.* [6] that presents a regime diagram based on Pe and Da , and the work of GOLFIER *et al.* [7] that present the regime diagrams based on Pe , Da and $PeDa$. Considering that the transition boundaries are based mostly on qualitative observation, some uncertainties are associated with these lines and discrepancies between the studies can be noticed.



(a)



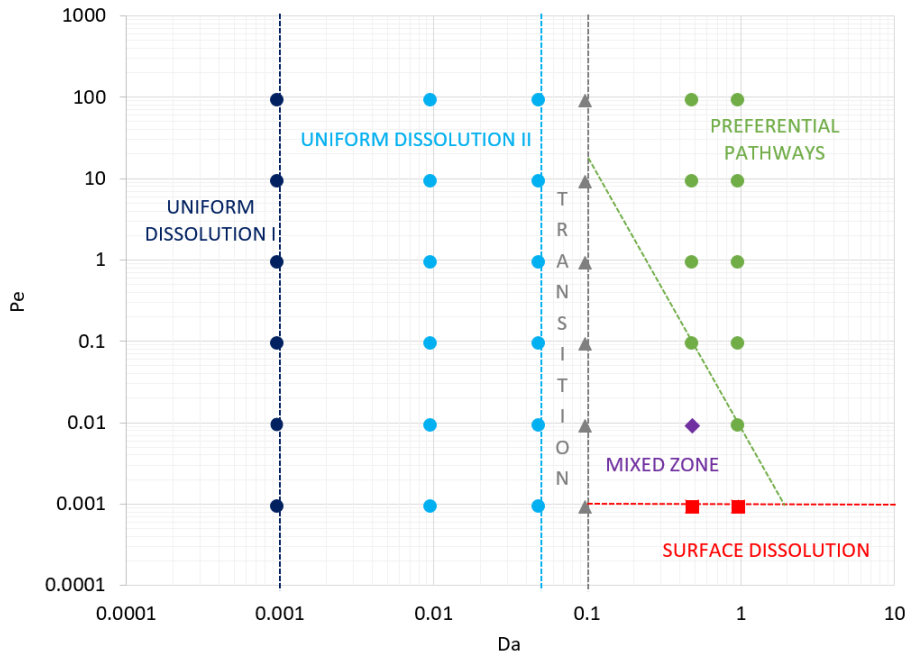
(b)

Figure 3.10: Behavior diagrams constructed from 10×10 network simulations: (a) Pe - Da ; and (b) Pe - $PeDa$.

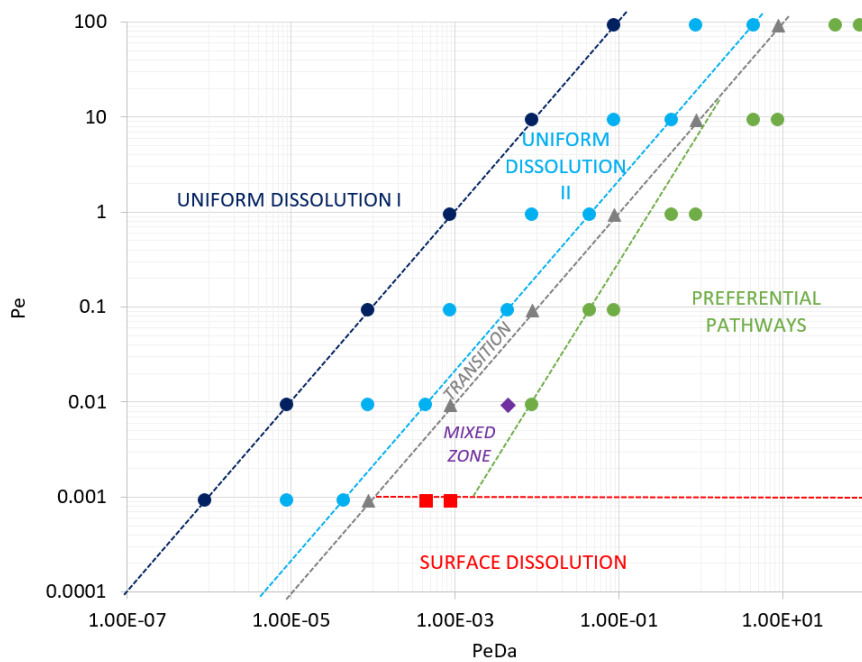
The pore network modeling used in this study is not capable yet to explore different preferential pathways regimes, as by previous studies [7, 6]. However, the main dissolution regimes are explored by using a different analysis tool, as presented in this section. Furthermore, because this model does not consider

merging of pores and throats, this limitation also may bring some difference in the analysis of the boundaries and regimes. It is also important to remember that dimensionless numbers are computed differently in each of the literature studies and this may explain these discrepancies. After all, it is important to highlight the applicability of pore network modeling as a tool to investigate dissolution regimes.

Concerning length scale effects, a network composed of 10×40 pores is used to investigate possible differences in the construction of behavior diagrams of different network sizes. From Figures 3.11a and 3.11b, it is possible to note that, besides all the agreements compared to the results from 10×10 network, a small discrepancy related to the mixed zone is observed. The transition pattern between surface dissolution and preferential pathways is reduced for the 10×40 network and is related to the increase of network heterogeneity, and consequently a faster transition between regimes with large mineral reactivity. Therefore, regardless of the difference in the mixed zone, one can conclude that the behavior diagrams are in good agreement considering networks with different sizes.



(a)



(b)

Figure 3.11: Behavior diagrams constructed from 10×40 network simulations: (a) Pe-Da; and (b) Pe-PeDa.

3.3.3 Verification in a 40×40 network

Considering here, a network with 40×40 pores, the main dissolution regimes are verified. Figure 3.12 presents the acid concentration profile for uniform, sur-

face dissolution, and preferential pathways regimes, respectively, after 50.6 PVI, 40.5 PVI and 50.6 PVI (Figs. 3.12a, 3.12b and 3.12c). The behaviors observed agree with the discussed features of each of the regimes: uniform dissolution presents a uniform concentration of acid through the entire domain, surface dissolution is characterized by a homogeneous concentration profile along the cross-sections perpendicular to the flow, and preferential pathways are highlighted by acid distribution through most permeable areas.

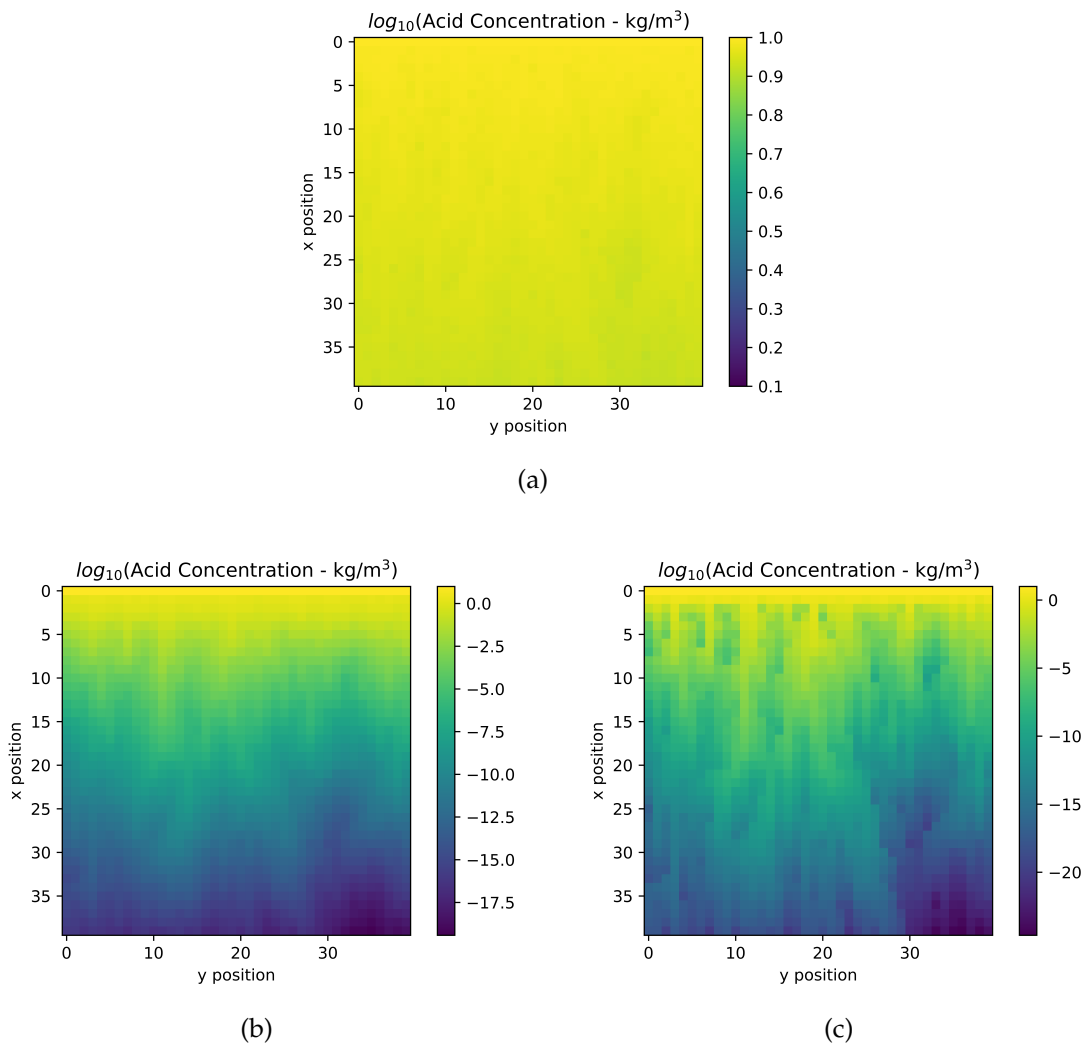


Figure 3.12: Final acid concentration profile in the 40×40 network (flow is from the top to the bottom): (a) Uniform dissolution ($Pe = 0.094$ and $Da = 0.0007$); (b) Surface dissolution ($Pe = 0.00094$ and $Da = 0.45$); and (c) Preferential pathways ($Pe = 94$ and $Da = 0.45$). Note that the color scale is different for each subfigure to feature differences among the regimes.

Additionally, Figure 3.13 presents the porosity-permeability relationship of these regimes. The linear pattern of the uniform distribution is apparent as

well as the power law pattern of surface dissolution and preferential pathways. It is important to observe here that surface dissolution again presents greater increase of permeability than preferential pathways due to the large dissolution rate for inlet pore spaces, even with the lack of pore merging. The importance of surface dissolution is also evidence of the role of diffusion. The standard deviations of these simulations were obtained and also agree with the regime specifications.

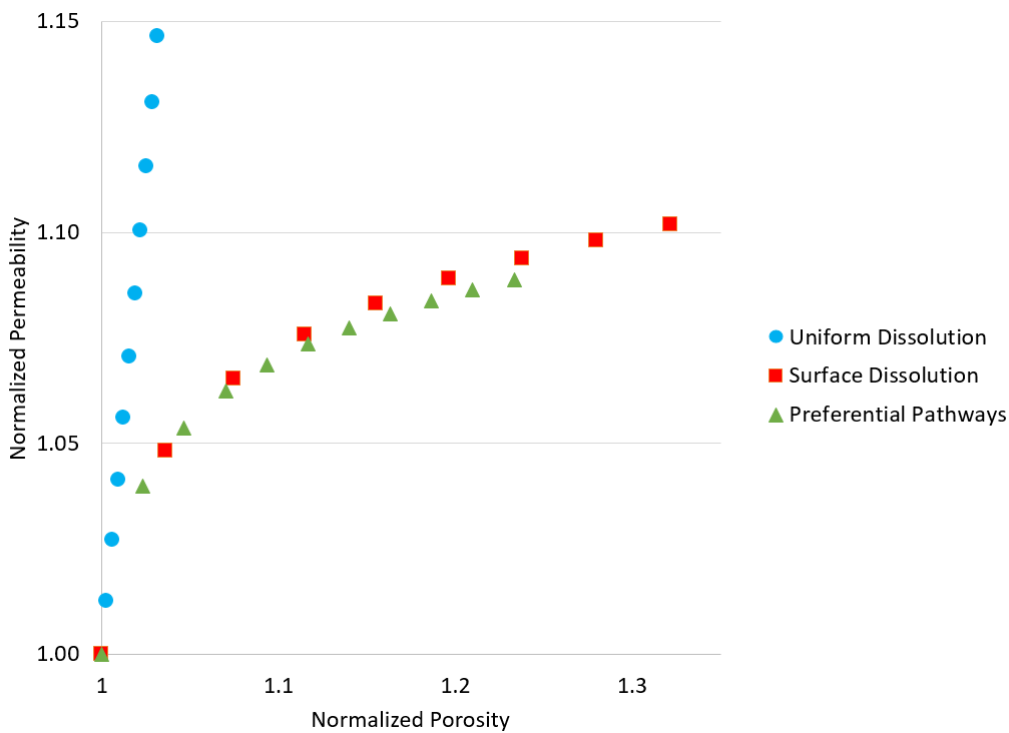


Figure 3.13: Porosity-permeability relationship results from 40×40 network simulations.

3.3.4 3D domain verification

A three dimensional domain is constructed to evaluate the generality of the features of the dissolution regimes obtained using 2D pore networks. Figure 3.14 presents the initial geometry for a network composed by $10 \times 10 \times 10$ pores.

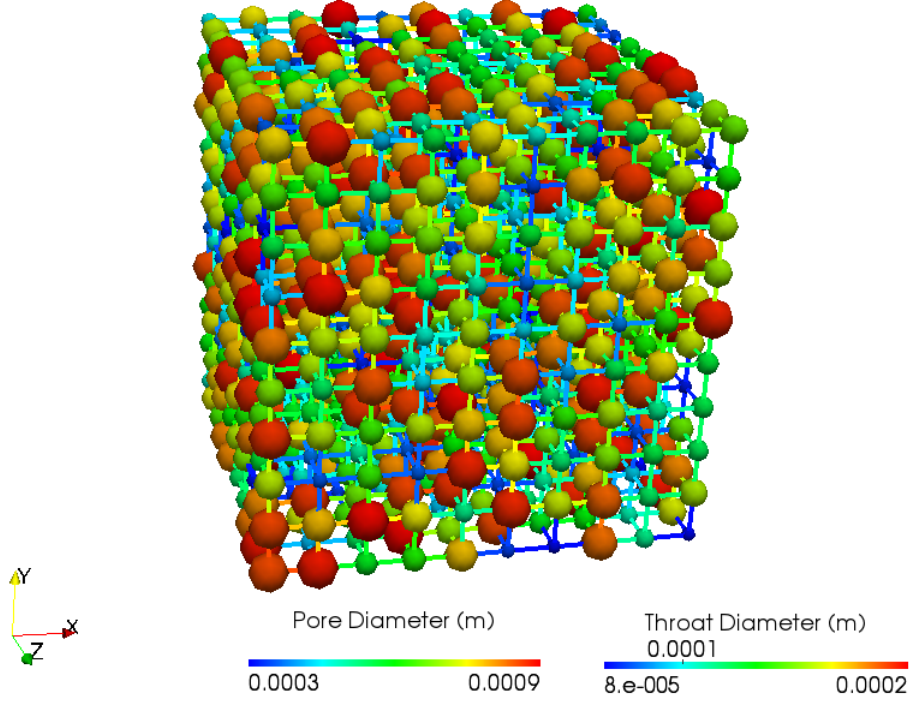
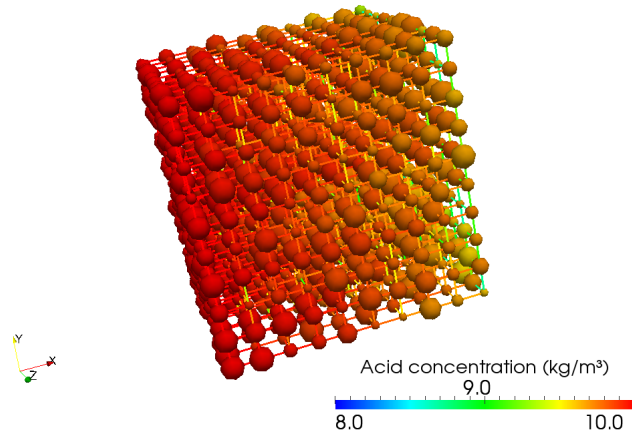
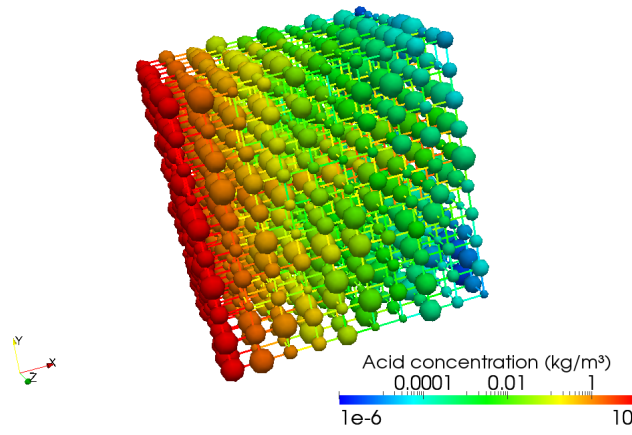


Figure 3.14: Scheme of the initial geometry for the network composed of $10 \times 10 \times 10$ pores.

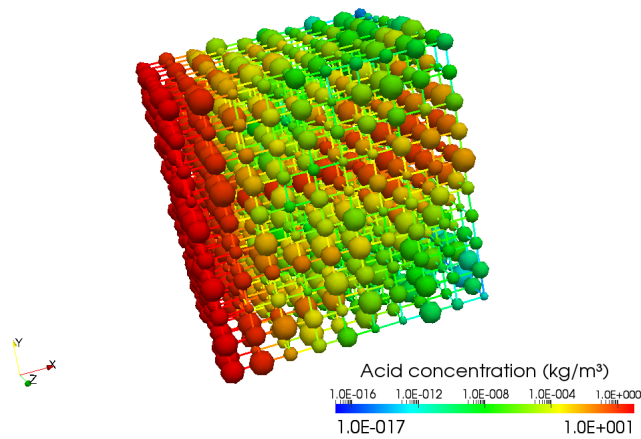
The acid concentration for uniform dissolution, surface dissolution and preferential pathways after 250.2 PVI, 150.1 PVI and 250.2 PVI, respectively, are presented in Figure 3.15. The features of each regime agree with discussions made considering 2D networks. The uniform dissolution (see Fig. 3.15a) presents a uniform distribution of the acid throughout the entire domain and shows a $\sigma_{net} = 0.01$ for the conditions assumed ($Pe = 0.095$, $Da = 0.0006$ and $PeDa = 6.06 \times 10^{-5}$). The surface dissolution (see Fig. 3.15b) presents a homogeneous distribution of the acid concentration along cross-sections perpendicular to the flow. The standard deviations of this regime and the dimensionless numbers result, respectively, in $\sigma_{net} = 1.56$ and $\overline{\sigma_{cross}} = 0.39$, and $Pe = 0.00095$, $Da = 0.57$ and $PeDa = 5.456 \times 10^{-4}$, that agree with the previous assumptions. The preferential pathways (see Fig. 3.15c) are well observed in the middle region of the network considering $Pe = 95$, $Da = 0.57$ and $PeDa = 5.456 \times 10^1$. The standard deviation of this condition is $\sigma_{net} = 3.52$ and $\overline{\sigma_{cross}} = 2.31$.



(a)



(b)



(c)

Figure 3.15: Acid concentration for the network composed by $10 \times 10 \times 10$ pores: (a) Uniform Dissolution; (b) Surface Dissolution; and (c) Preferential Pathways.

The porosity-permeability relationships for the three main dissolution

regimes are presented in Fig. 3.16. The uniform dissolution regime presents a linear pattern, as observed for 2D simulations. The surface dissolution result also replicates the results obtained for 2D domains, that present a more rapid increase of the porosity in comparison to the permeability as a result of the geometry changes in the inlet area of the networks. On the other hand, the preferential pathways presents a different pattern, where a power-law behavior is observed initially (at normalized porosity range of 1 – 1.2), followed by a pronounced increase of the permeability, that characterizes the formation of preferential pathways. This difference is related to the greater degree of freedom for 3D simulations that allows more propagation options for the fluid throughout the porous medium and increases the evidence of highly conductive channels formation. These different behaviors in 2D and 3D networks are expected, because the preferential pathways regime tends to create fractal structures [78, 79] that depend on the dimensionality of the enclosing domain.

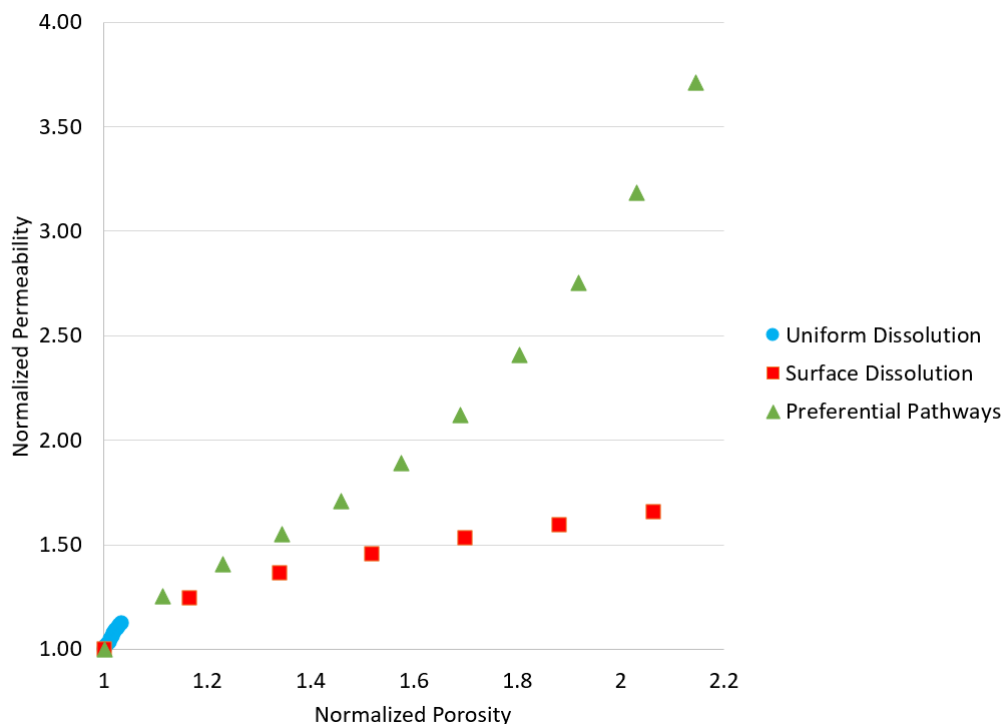


Figure 3.16: Porosity-permeability relationship results from $10 \times 10 \times 10$ network simulations.

3.3.5 Implementation on networks derived from carbonate data

The single-phase reactive transport approach developed in this work was also implemented using a pore network obtained from a carbonate rock. This pore network model is used to ensure the applicability of this methodology for more complex topologies. Here, the inlet acid concentration is set to 1 kg/m^3 and a reaction-limited scenario is presented, considering $Da = 0.001$. Greater reactivities cannot be considered without including the merging of pores and throats.

Figure 3.17 presents the final concentration profile of a uniform dissolution pattern simulation, that is in good agreement with the behaviors observed in cubic networks and presenting $\sigma_{net} = 0.003$.

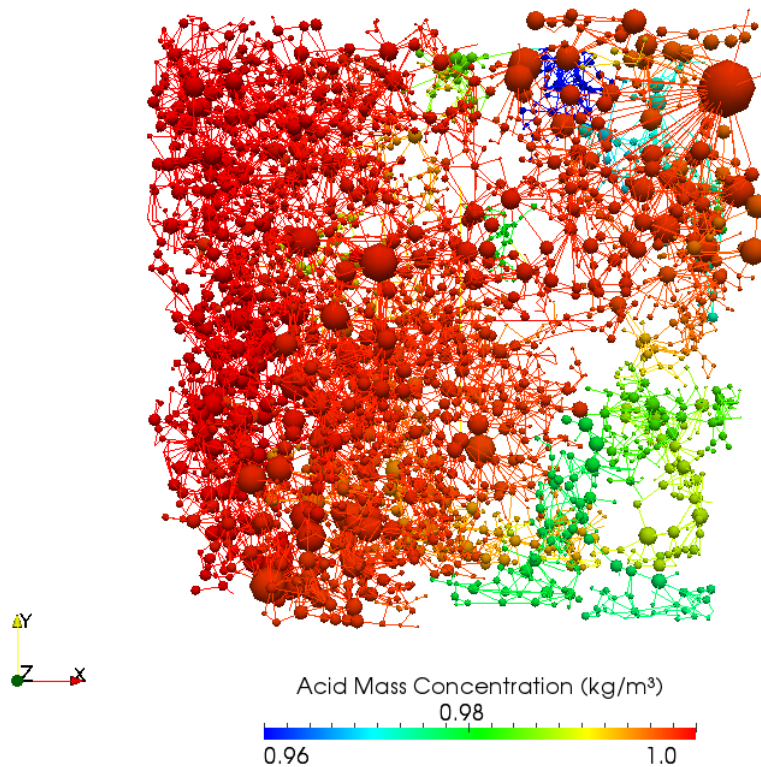


Figure 3.17: Final acid concentration profile for a uniform dissolution regime simulation in network derived from a carbonate rock sample. A narrow concentration scale is used to highlight the differences in concentration within the network.

3.3.6 Analysis of porosity-permeability curves

The results of porosity and permeability evolution from the simulation on the carbonate network are compared with regular cubic network results and literature data. The power-law exponent of the curves obtained by plotting $\log(K/K_0)$ versus $\log(\phi/\phi_0)$ are compared with values obtained by EGERMANN *et al.* [11] and BEKRI *et al.* [39]. Both worked with 3D regular pore networks constructed based on petrophysical laboratory data. EGERMANN *et al.* [11] also conducted core-flood experiments. The latter, related the power-law exponent with the dissolution pattern, where reaction-limited regimes were identified between values of 1.5 and 6.9 (identified in Table 3.1 by the subscripts *min* and *max*, respectively). Greater values were related to a convective-predominant regime described by changes only in throats geometry (value identified by the subscript *throats*).

Table 3.1 presents the power-law exponents and their references. It is noticed that simulations in the 2D and 3D pore networks previously discussed in this work, and from BEKRI *et al.* [39] obtained values in the range that represents uniform dissolution. For the carbonate simulation, the exponent is larger and is explained by the fact that the available surface areas obtained for this sample (see Eq. (3.25)) are much smaller due to the significant heterogeneity of the pore and throat sizes. Consequently, for this case, changes were observed mainly in the permeability due to dissolution of throats.

The implementation of merging of pores and throats would improve and facilitate the use of the approach presented in this study to evaluate dissolution regimes in more complex pore networks derived from real porous media. This will likely change the response of permeability and porosity for extreme cases, respectively represented by preferential pathways and surface dissolution regimes, and improve the representativeness of the model with respect to the physical processes being studied.

3.4 Summary

This work presents a pore-network modeling approach to evaluate the effects of different transport mechanisms and mineral reactivity on dissolution

Table 3.1: Comparison among power-law exponents for the uniform dissolution regime.

Reference	Exponent
EGERMANN <i>et al.</i> [11] _{throats}	31.0
Carbonate	24.3
EGERMANN <i>et al.</i> [11] _{max}	6.9
2D Regular Network (10 × 10)	4.0
3D Regular Network (10 × 10 × 10)	3.7
BEKRI <i>et al.</i> [39]	3.2
EGERMANN <i>et al.</i> [11] _{min}	1.7

regimes, as well as changes in porosity and permeability. The transport problem is implemented by considering the acid mass balance inside pores and throats. The changes in pore-space geometry due to dissolution are considered based on the rate of the heterogeneous chemical reaction happening at the solid surface. Péclet and Damköhler dimensionless numbers are used to construct behavior diagrams in order to characterize the different dissolution regimes.

The reactive transport simulations developed in this work exhibit results similar to those previously discussed in the literature based on direct simulations and experimental trials. In this work, five dissolution regimes were explored based on acid concentration, network geometry, volumetric flow rate, porosity-permeability relationship, and standard deviation analysis, that was successfully introduced as a quantitative criterion for the cases studied. These regimes include uniform dissolution ($Da < 0.05$), transition zone ($0.05 < Da < 0.1$), surface dissolution ($Da > 0.1$ and $Pe < 0.001$), mixed zone, and preferential pathways (in general, for $Da > 0.1$ and $Pe > 0.001$).

The results demonstrate the applicability of pore-network modeling as a tool to explore reactive transport and dissolution processes, as well as to predict changes in porosity and permeability. Results demonstrated the various dissolution regimes observed at larger scales. The use of a pore-network approach to

understand reactive transport during single-phase flow also offers new possibilities of investigation.

Merging of pores and throats to form vug-like pores is suggested as an improvement to better evaluate regimes with significant mineral reactivity. Incorporation of cornered pores with triangular geometry, that are the most common pore shape, allows the exploration of more complex systems based on multiphase reactive transport. In this way, multiphase systems are also suggested to be implemented to represent various subsurface and reservoir conditions.

Chapter 4

The novel merging approach

The content of this chapter was submitted to *Advances in Water Resources*.

In the remainder of this chapter, we first present the objectives and main contributions of this study. Then, the methodology of the proposed merging approach is described in detail. Finally, we present the simulation results. We close with a summary of the main highlights of this work.

4.1 Objectives and contributions

The main objective of this study is to develop an approach to the merging of dissolving pores that conserves important geometrical and transport properties. For this, we introduce the use of correction factors and effective properties.

The main contribution of this work is to extend and improve the method for reactive transport and mineral dissolution developed in previous work [29], thereby bringing the model closer to the physical problem and making possible the use of reactive transport simulations to evaluate dissolution regimes in more complex network topologies. There, the odds for the junction of two pore spaces initially separated increases due to the heterogeneous size distributions of these type of porous media.

4.2 Methodology

The methodology section first presents the pore-network models used for this study. Then, the equations for determining the pressure and concentration fields are detailed. The kinetics of dissolution and the evolution of the volumes and geometry of the network are described. Finally, the new merging approach for merging of dissolving pores are introduced. All units of measurement used in this study are in accordance with the International System of Units (SI).

4.2.1 Pore-network models construction

Porous media are investigated using two- and three-dimensional (2D and 3D) cubic pore-network models. Pore networks were constructed using OpenPNM, [74]. The pores are characterized as spherical and are connected to each other by cylindrical throats with circular cross-sections. Pore walls are assumed to be composed of a single mineral such as calcite. The pore coordination number is initially 4 and 6, respectively, in the regular two- and three-dimensional dimensional networks whereas it varies from 3.88 to 6.89 for the three-dimensional random networks.

The regular two- and three-dimensional networks were generated considering a random uniform distribution of pore sizes, in the range of $100 - 300\mu m$. Throat diameters have $1/8$ of the diameter of the smallest pore connected to it. The interpore distances are equal to $300\mu m$ and $320\mu m$ for the 2D and 3D networks, respectively.

The random three-dimensional pore network was generated by a method from OpenPNM [74] that creates a random network formed by Gabriel tessellation of arbitrary base points, that performs a Deluanay tessellation and removes connections that are not in accordance to the definition of the Gabriel graph [74]. The size of the pores are defined by a random value between 70% – 90% of the smallest connected throat interpore distance. Throat diameters have $1/8$ of the diameter of the smallest pore connected to it. The network has a total of 1000 pores, 3447 throats, and an average coordination number of 6.89.

A three-dimensional network was constructed based on the topology infor-

mation of a carbonate sample. The size of the pores are defined by a random value between 60% – 80% of the smallest connected throat interpore distance. Throat diameters have 1/8 of the diameter of the smallest pore connected to it. The network has a total of 2612 pores, 5071 throats, and an average coordination number of 3.88.

Table 4.1 presents the initial porosity (ϕ_0) and initial absolute permeability (K_0) of the networks used in this study.

Table 4.1: Initial porosity (ϕ_0) and initial absolute permeability (K_0) of the networks used in this study

Network	ϕ_0 (%)	K_0 (m^2)
10x10	20	2.7×10^{-13}
20x20	19	1.9×10^{-13}
40x40	20	1.8×10^{-13}
10x10x10	16	2.0×10^{-13}
Random	8	6.5×10^{-14}
Carbonate	8	3.7×10^{-16}

4.2.2 Pressure field

The pressure field is obtained in accordance with the methodology described in section 3.2.2 considering one modification: throat volumetric flow rates are obtained using the effective conductance instead of the conductance derived only by geometric data. Effective conductances assure that the relationship between flow rate through pores and the extent of dissolution is represented accurately. The effective conductance ($c_{\epsilon,ij}$) is described by

$$c_{\epsilon,ij} = \epsilon_{ij}c_{ij}, \quad (4.1)$$

where ϵ_{ij} is the conductance correction factor. The conductance correction factor is equal to 1 for all original throats, and the value is updated when the throat ij is involved in a merging process. Thus, for original throats, the effective conductance is always equals to the conductance. To conclude, the equation for the throat volumetric flow rate considering the effective conductance is obtained by

$$q_{ij} = c_{\epsilon,ij} (P_i - P_j). \quad (4.2)$$

4.2.3 Concentration field

The reactive transport and dissolution problem is described by the mass balance in all available pore spaces, pores and throats, and is deduced from the mass conservation equations of the chemical species [75]. The main difference between our old approach and this new approach is the use of effective surface areas instead of the reactive surface area obtained just by geometrical information.

The effective surface area is the geometrical reactive surface area corrected by a factor when merging happens within the pore space, as presented below:

$$A_{\psi,i} = \psi_i A_{r,i}, \quad (4.3)$$

$$A_{\psi,ij} = \psi_{ij} A_{r,ij}. \quad (4.4)$$

where $A_{\psi,i}$ is the effective surface area of pore i , $A_{\psi,ij}$ is the effective surface area of throat ij , ψ_i is the surface area correction factor of pore i and ψ_{ij} is the surface area correction factor of throat ij .

Considering this, original pores and throats have surface area correction factors equal to 1. The correction factor of a pore space is just updated if it is involved in a merging process. So, until a merging event happens, the effective surface area of a pore space is equal to its geometrical surface area, obtained by Eqs. (3.25) and (3.22), respectively for pores and throats.

Implementation of correction factors ensures that surface area and conductance evolve in a physically realistic manner. More details about the update of surface area correction factors are available in later sections.

Considering this, the transport of a chemical species occurs by advection and diffusion. The mass balance equation for chemical species α in pore i is

$$\begin{aligned} \frac{d}{dt}(C_{\alpha,i}V_i) = \sum_{ij,in} C_{\alpha,ij}q_{ij} - C_{\alpha,i} \sum_{ij,out} q_{ij} + \sum_{ij} A_{ij}\mathcal{D}_\alpha \left(\frac{C_{\alpha,ij} - C_{\alpha,i}}{0.5l_{ij} + r_i} \right) \\ - R_{\alpha,i}A_{\psi,i}. \end{aligned} \quad (4.5)$$

For control volumes represented by throats, the mass balance equation for species α in throat ij is

$$\begin{aligned} \frac{d}{dt}(C_{\alpha,ij}V_{ij}) = (C_{\alpha,i} - C_{\alpha,ij})q_{ij} + A_{ij}\mathcal{D}_\alpha \left(\frac{C_{\alpha,i} - C_{\alpha,ij}}{0.5l_{ij} + r_i} \right) + A_{ij}\mathcal{D}_\alpha \left(\frac{C_{\alpha,j} - C_{\alpha,ij}}{0.5l_{ij} + r_j} \right) \\ - R_{\alpha,ij}A_{\psi,ij}. \end{aligned} \quad (4.6)$$

In our approach, the concentration field is solved implicitly (implicit Euler method) and the volume explicitly in a sequential algorithm. In other words, the system is solved for the new concentrations based on the previous geometry, that is kept constant during the solution of Eqs. (4.5) and (4.6). The linear system for the unknown concentrations of species α is solved by the `spsolve` direct method from the SciPy library [76].

The domain initial condition and the boundary conditions are represented by Eqs. (3.7), (3.8) and (3.9), previously presented and discussed. In summary, the initial condition represents a constant concentration profile, the inlet condi-

tion is a constant concentration, and the outlet condition represents an outflow boundary condition. Figure 4.1 presents a scheme of the boundary pores (in red), that are added to the network to apply the boundary conditions. Pores in blue represent the porous medium in analysis.

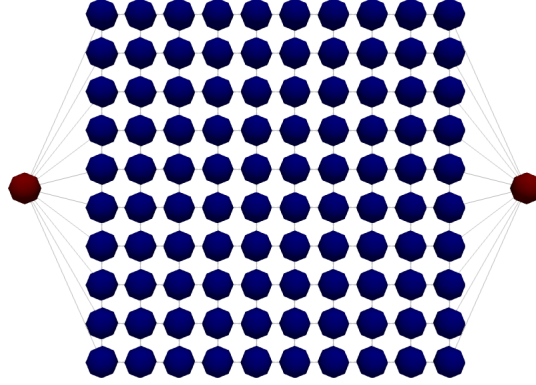


Figure 4.1: Scheme of the boundary condition pores (in red). Pores in blue represent the porous medium under analysis. The properties of boundary pores do not change in time.

4.2.4 Kinetics of dissolution

The kinetics of dissolution is described in section 3.2.4.

4.2.5 Volume evolution and geometry update

As our solution involves geometry changes at each time step during the simulations, control volumes of pores and throats are changed. In this way, after each time step, with the solution of the concentration field based on mass balance, the change in volume of the pore spaces is obtained by the relation between the solid consumed on the effective surface of each pore space and the density of the reactive mineral that composes the porous medium.

Considering a first-order reaction rate for the heterogeneous chemical reaction and a stoichiometric coefficient (β) that relates the consumption of the hydrochloric acid ($\alpha = a$) and the consumption of the reactive mineral, the change in volume due to the dissolution process is given by

$$\delta V_i^d \simeq \frac{R_{a,i} A_{\psi,i}^n \beta \delta t}{\rho_s} = \frac{(k_r C_{a,i}^{n+1,*}) A_{\psi,i}^n \beta \delta t}{\rho_s}, \quad (4.7)$$

$$\delta V_{ij}^d \simeq \frac{R_{a,ij} A_{\psi,ij}^n \beta \delta t}{\rho_s} = \frac{(k_r C_{a,ij}^{n+1,*}) A_{\psi,ij}^n \beta \delta t}{\rho_s}, \quad (4.8)$$

where δV_i^d is the change in volume due to dissolution process in pore i and δV_{ij}^d is the change in volume due to dissolution process in throat ij

Based on Eqs. (4.7) and (4.8), the change in radii of pores (δr_i^d) and throats (δr_{ij}^d) due to dissolution is defined (see Fig. 4.2), respectively, as

$$\delta r_i^d = \frac{\delta V_i^d}{A_{\psi,i}^n} = \frac{k_r C_{a,i}^{n+1,*} \beta dt}{\rho_s}, \quad (4.9)$$

$$\delta r_{ij}^d = \frac{\delta V_{ij}^d}{A_{\psi,ij}^n} = \frac{k_r C_{a,ij}^{n+1,*} \beta dt}{\rho_s}. \quad (4.10)$$

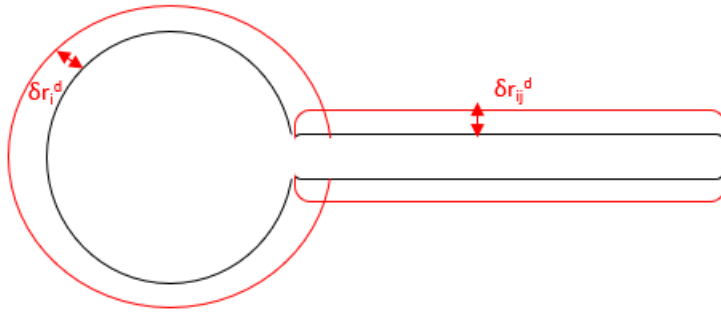


Figure 4.2: Scheme of the change in volume due to dissolution for pores and throats. δr_i^d and δr_{ij}^d represents the radius increase, respectively for pores and throats.

There are regions in the contact area between pore i and connecting throats ij that the same volume is dissolved twice: by the pore i and the throat ij , simultaneously (see Fig.4.3, hatched area in red). The consumed volume needs

to be counted twice to keep the mass conservative. For this, the volume related to this region, derived from the dissolution of throat ij , is transferred to the pore i . The change in volume due to double dissolution is then defined by

$$\delta V_{i,ij}^{dd} = \pi \left[\left(r_{ij}^n + \delta r_{ij}^d \right)^2 - \left(r_{ij}^n \right)^2 \right] \delta r_i^d. \quad (4.11)$$

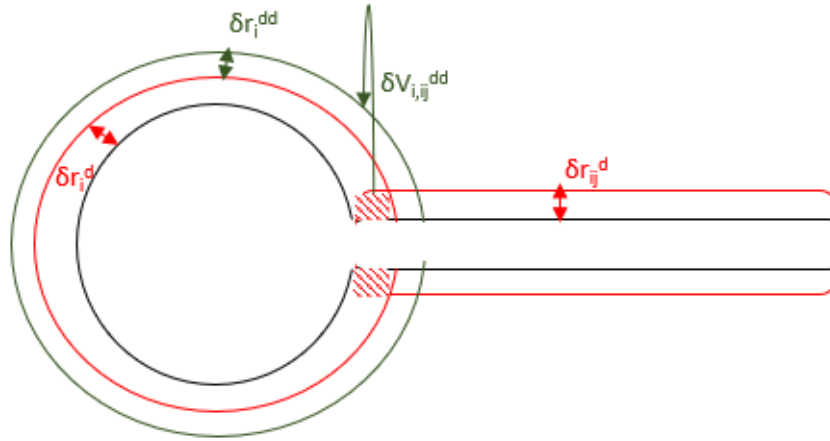


Figure 4.3: Scheme of the change in volume due to double dissolution ($\delta V_{i,ij}^{dd}$). Hatched area in red represents the contact area between pore i and connecting throats ij that is dissolved twice and δr_i^{dd} is the respective pore radius increase.

For throats, the double dissolution may consider the contact area between the two connected pores i and j (see Eq. (4.12)), and for pores, the double dissolution may account for the contact area between pore i and all connected throats ij (see Eq. (4.13)).

$$\delta V_{ij}^{dd} = \delta V_{i,ij}^{dd} + \delta V_{j,ij}^{dd}, \quad (4.12)$$

$$\delta V_i^{dd} = \sum_{ij} \delta V_{i,ij}^{dd}. \quad (4.13)$$

The change in radius of pore i due to the double dissolution is defined by

$$\delta r_i^{dd} = \frac{\delta V_i^{dd}}{A_{\psi,i}^n}. \quad (4.14)$$

The grain region that pore i invades due to the addition of the double dissolved volumes that is also invaded by the dissolution of throat ij (see Fig.4.4, hatched area in green) is also transferred to the pore. The volume related to this region are defined by Eq. (4.15). The total change in volume related to this step for throats and pores are defined, respectively in Eqs. (4.16) and (4.17).

$$\delta V_{ij}^{c1} = \pi \left[\left(r_{ij}^n + \delta r_{ij}^d \right)^2 - \left(r_{ij}^n \right)^2 \right] \delta r_i^{dd}. \quad (4.15)$$

$$\delta V_{ij}^{c1} = \delta V_{i,ij}^{c1} + \delta V_{j,ij}^{c1}. \quad (4.16)$$

$$\delta V_i^{c1} = \sum_{ij} \delta V_{i,ij}^{c1}. \quad (4.17)$$

The change in radius of pore i due to the this first correction step is defined by

$$\delta r_i^{c1} = \frac{\delta V_i^{c1}}{A_{\psi,i}^n}. \quad (4.18)$$

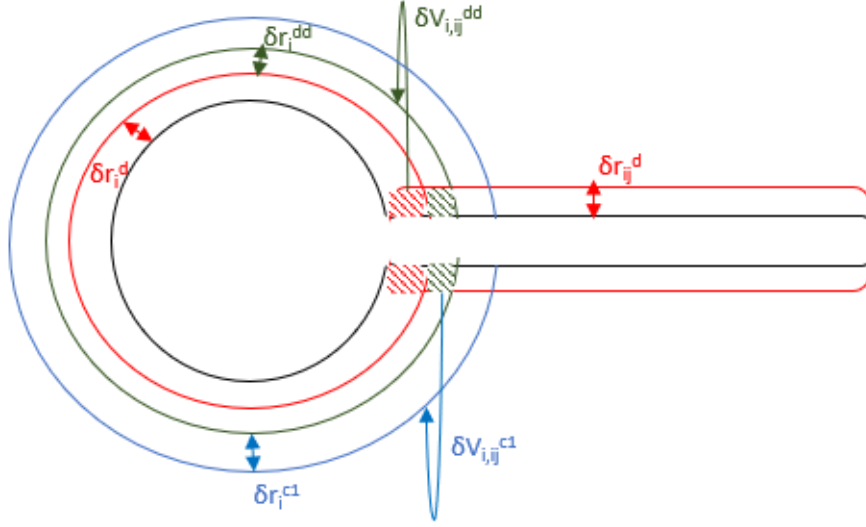


Figure 4.4: Scheme of the change in volume due to correction 1 ($\delta V_{i,ij}^{c1}$). Hatched area in green represents the contact area between pore i and connecting throats ij that needs to be relocated and δr_i^{c1} is the respective pore radius increase.

Again, the grain region that pore i invades due to the addition of the correction volume $\delta V_{i,ij}^{c1}$ that is also invaded by the dissolution of throat ij (see Fig.4.5, hatched area in blue) is transferred for the pore. The volume related to this region are defined by Eq. (4.19). The total change in volume related to this step for throats and pores are defined, respectively in Eqs. (4.20) and (4.21).

$$\delta V_{i,ij}^{c2} = \pi \left[\left(r_{ij}^n + \delta r_{ij}^d \right)^2 - \left(r_{ij}^n \right)^2 \right] \delta r_i^{c1}. \quad (4.19)$$

$$\delta V_{ij}^{c2} = \delta V_{i,ij}^{c2} + \delta V_{j,ij}^{c2}. \quad (4.20)$$

$$\delta V_i^{c2} = \sum_{ij} \delta V_{i,ij}^{c2}. \quad (4.21)$$

The change in radius of pore i due to the this second correction step is defined by

$$\delta r_i^{c2} = \frac{\delta V_i^{c2}}{A_{\psi,i}^n}. \quad (4.22)$$

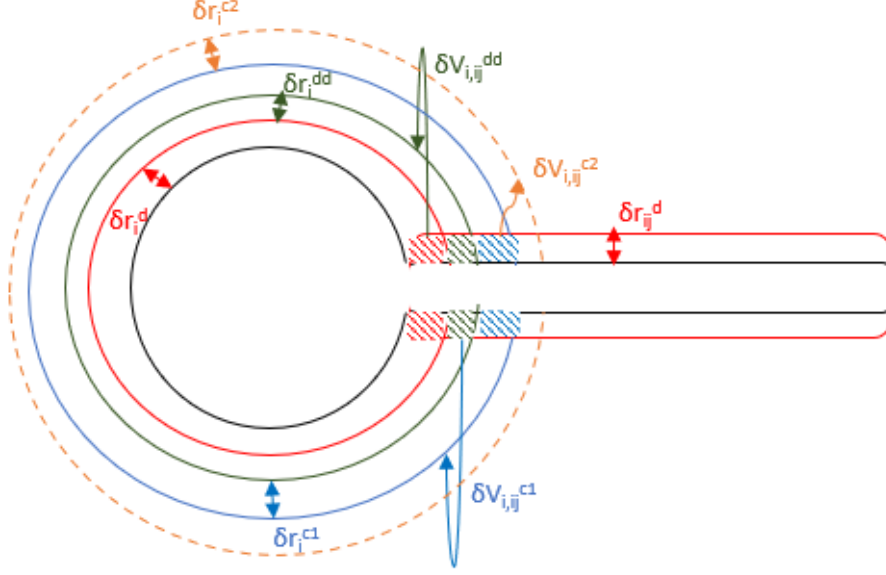


Figure 4.5: Scheme of the change in volume due to correction 1 ($\delta V_{i,j}^{c2}$). Hatched area in blue represents the contact area between pore i and connecting throats ij that needs to be relocated and δr_i^{c2} is the respective pore radius increase.

Formally, the transfer of volumes between pores and throats requires an iterative process to achieve a desired level of accuracy. Here, the correction step stops in the second correction because its magnitude is already rather small. For example, for a pore and a throat with diameters equal to 1 and 0.25, respectively, that both suffered a increase of 0.2, the relative error of the final volume of the pore after the second iteration compared to 10 more iterations is 0.00006%.

Finally, pore i invades a porous region previously belonged to throat ij (see Fig.4.6, hatched area in purple). For this case, not only the volume but also the mass of acid that previously belonged to throat ij needs to be transferred to pore i . Considering this, the transferred porous volume and mass of acid from throat ij to pore i are defined, respectively, by

$$\delta V_{i,j}^t = \left(\delta r_i^d + \delta r_i^{dd} + \delta r_i^{c1} + \delta r_i^{c2} \right) A_{i,j}^n, \quad (4.23)$$

$$\delta m_{i,ij}^t = C_{ij}^{n+1,*} \left(\delta r_i^d + \delta r_i^{dd} + \delta r_i^{c1} + \delta r_i^{c2} \right) A_{i,ij}^n. \quad (4.24)$$

The total change in volume related to this step for throats and pores are defined, respectively in Eqs. (4.25) and (4.26).

$$\delta V_{ij}^t = \delta V_{i,ij}^t + \delta V_{j,ij}^t. \quad (4.25)$$

$$\delta V_i^t = \sum_{ij} \delta V_{i,ij}^t. \quad (4.26)$$

The total change in mass of acid related to this step for throats and pores are defined, respectively in Eqs. (4.27) and (4.28).

$$\delta m_{ij}^t = \delta m_{i,ij}^t + \delta m_{j,ij}^t. \quad (4.27)$$

$$\delta m_i^t = \sum_{ij} \delta m_{i,ij}^t. \quad (4.28)$$

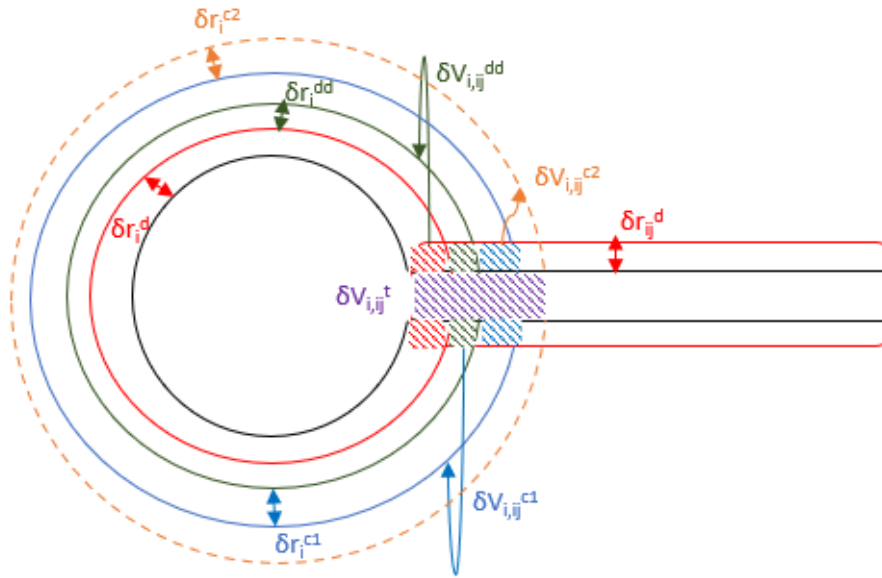


Figure 4.6: Scheme of $\delta V_{i,j}^t$. Scheme of the change in volume due to transfers ($\delta V_{i,j}^t$). Hatched area in purple represents the porous area of throats ij that needs to be transferred to pore i and δr_i^t is the respective pore radius increase.

Figure 4.7 presents a flowchart with the main steps necessary for the determination of the total change in volume of pores and throats at each time step of the simulations.

Some controls on the numerical scheme were implemented, as follows. The ratio of the change of throat radius due to dissolution (δr_{ij}^d) to the throat radius from the previous time step in all time steps was always kept smaller than 0.1, in order to keep a good approximation of the differentials. Also, the Courant numbers (defined as the ratio of the inlet velocity multiplied by the time step to the average length of throats) in all simulations ranged from 0.11 to 1.34. Importantly, all transport-limited conditions presented Courant numbers smaller than 1.

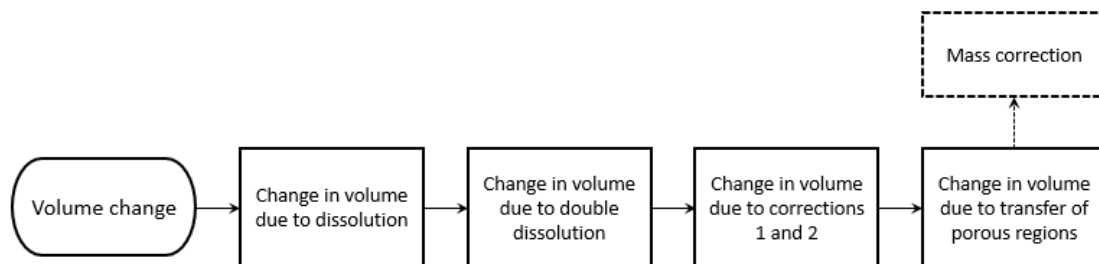


Figure 4.7: Flowchart with the main steps to obtain the total change in volume of pores and throats. The main steps include changes due to dissolution, double dissolution, corrections 1 and 2, and transfer of porous spaces.

The next section presents the algorithm with the total evolution of the volumes of pores and throats, and the geometry update.

4.2.5.1 Algorithm for the geometry update

The steps for the geometry update of pores and throats, considering the evolution of volumes described in the previous section, are described below.

1. Computation of the change in volume of pores and throats.
 - (a) Computation of the change in volume of pores and throats due to dissolution (δV_i^d and δV_{ij}^d) using Eqs. (4.7) and (4.8).
 - (b) Computation of the change in volume of pores and throats due to double dissolution (δV_i^{dd} and δV_{ij}^{dd}) using Eqs. (4.13) and (4.12).
 - (c) Computation of the change in volume of pores and throats due to the first correction step (δV_i^{c1} and δV_{ij}^{c1}) using Eqs. (4.17) and (4.16).
 - (d) Computation of the change in volume of pores and throats due to the second correction step (δV_i^{c2} and δV_{ij}^{c2}) using Eqs. (4.21) and (4.20).
 - (e) Computation of the change in volume of pores and throats due to the transfer of porous spaces (δV_i^t and δV_{ij}^t) using Eqs. (4.26) and (4.25).
2. Computation of the total change in volume of pores by

$$\delta V_i = \delta V_i^d + \delta V_i^{dd} + \delta V_i^{c1} + \delta V_i^{c2} + \delta V_i^t \quad (4.29)$$

3. Computation of the total change in volume of throats by

$$\delta V_{ij} = \delta V_{ij}^d - \delta V_{ij}^{dd} - \delta V_{ij}^{c1} - \delta V_{ij}^{c2} - \delta V_{ij}^t \quad (4.30)$$

4. Update of the new volume of pores and throats, respectively, by

$$V_i^{n+1} = V_i^n + \delta V_i, \quad (4.31)$$

$$V_{ij}^{n+1} = V_{ij}^n + \delta V_{ij}. \quad (4.32)$$

5. Computation of the change in mass of acid of pores and throats due to the transfer of porous spaces (δm_i^t and δm_{ij}^t) using Eqs. (4.28) and (4.27).

6. Computation of the total change in mass of acid inside of pores and throats by

$$m_i^{n+1} = \left(C_i^{n+1,*} V_i^n \right) + \delta m_i^t, \quad (4.33)$$

$$m_{ij}^{n+1} = \left(C_{ij}^{n+1,*} V_{ij}^n \right) - \delta m_{ij}^t. \quad (4.34)$$

7. Calculation of the new pore radii considering pores as spheres, by

$$r_i^{n+1} = \sqrt[3]{\frac{3V_i^{n+1}}{4\pi}}. \quad (4.35)$$

8. Correction of the new length of throats, by

$$l_{ij}^{n+1} = d_{ij} - r_i^{n+1} - r_j^{n+1}. \quad (4.36)$$

9. Calculation of the new throat radii, by

$$r_{ij}^{n+1} = \sqrt[2]{\frac{V_{ij}^{n+1}}{\pi l_{ij}^{n+1}}}. \quad (4.37)$$

10. Update of the reactive surface area and cross-sectional area of throats, respectively, using Eqs. (3.22) and (3.23).
11. Update of the reactive surface area of pores using Eq. (3.25).
12. Update of the effective surface area of pores and throats using Eqs. (4.3) and (4.4).
13. Update of the conductance of throats using (3.3).
14. Update of the effective conductance of throats using Eq. (4.1).
15. Update of the acid concentration based on the new volumes obtained by the geometry update, as

$$C_i^{n+1} = \frac{m_i^{n+1}}{V_i^{n+1}}, \quad (4.38)$$

$$C_{ij}^{n+1} = \frac{m_{ij}^{n+1}}{V_{ij}^{n+1}}. \quad (4.39)$$

The above procedure is repeated for each time step and, because of this, it is possible to evaluate the evolution of the permeability and also the pore-space during the simulation of the reactive transport coupled with dissolution process.

4.2.6 The new merging approach

This section presents the methodology developed to consider merging of pores and throats during reactive transport simulations when pore surfaces dissolve. The novel merging approach methodology, introduces the use of correc-

tion factors to conserve effective surface areas and conductance of throats during the merging process.

In this way, the strategy for merging of pores and throats presented here aims to conserve not only the volume and the mass balance of the system, before and after the application of the merging method, but also the reactive surface area and the conductance of throats. These are key parameters for the reactive transport problem that depends strongly on flow properties (conductance of throats) and features related to the reactivity of the system (reactive surface area).

The idea is to consider an effective surface area and an effective conductance as the parameters necessary to solve the reactive transport problem. In other words, the idea is to replace the area and conductance originally obtained by an effective surface area and conductance that considers approximately the deformation of the pore spaces upon merging.

For this, correction factors are introduced to conserve the effective surface area and effective conductance during the merging process. Therefore, ψ is introduced as the correction factor for surface areas and ϵ is introduced as the correction factor for conductance.

Effective surface area of pores and throats were defined previously in this section by Eqs. (4.3) and (4.4). Effective conductance of throats are defined by Eq. (4.1).

Considering this, original pores and throats have correction factors equal to 1. So, the effective surface areas and effective conductances have the same value as the surface areas and conductances of the pores spaces.

New merged pores as well as pores and throats connected to the new merged pores have correction factors different from one to account for the geometric deformations arising from the assumptions of the merge method and, in this way, conserve the effective surface areas and effective conductances during the merging process.

Here, the merging method is performed when two connected pores reach each other. Also, when a throat diameter reaches the same value of the diameter of a connected pore, the merging method is called to merge the pores connected

to this throat.

The main steps of this novel merging methodology are then described. The method is explained considering the case of the overlapping pores, but it is similar for the case of throats with larger diameters than the connected pores.

During the merging process, when the merging condition is satisfied, the two original pores are replaced by one new pore with volume, mass of acid, and effective surface area equal to the sum of the corresponding properties of the two original pores (see Fig. 4.8).

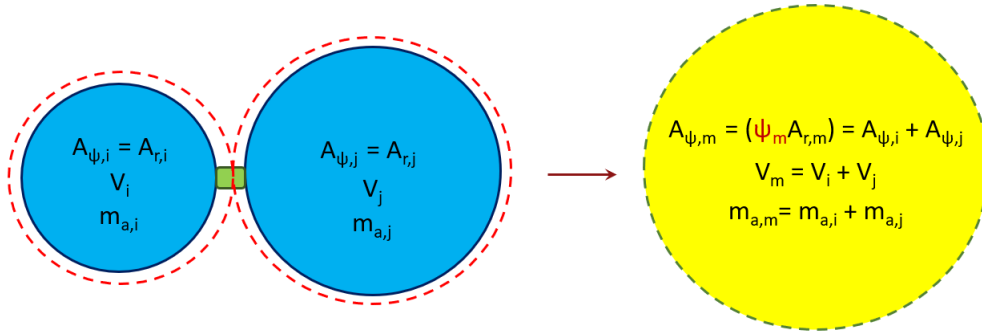


Figure 4.8: The two original pores are replaced by one new pore, that has the same total volume, total mass of acid, and total effective surface area as the two original pores.

The new merged pore is located in the volume-weighted average of the coordinates of the connecting pores, as presented below

$$\mathbf{x}_m = \frac{V_i \mathbf{x}_i + V_j \mathbf{x}_j}{V_m}, \quad (4.40)$$

where \mathbf{x}_m , \mathbf{x}_i , and \mathbf{x}_j are the position vectors of the merged pore m and the merging pores i and j , respectively.

The new radius of the merged pore r_m^{n+1} is obtained by

$$r_m^{n+1} = \sqrt[3]{\frac{3V_m^{n+1}}{4\pi}}. \quad (4.41)$$

The length of the throats connected to the the new merged pores (l_{mk}^{n+1}) are

updated due to the new location of the merged pore by

$$l_{mk}^{n+1} = d_{mk} - r_m^{n+1} - r_k^{n+1}. \quad (4.42)$$

where d_{mk} is the interpore distance between the newly merged pore m and the connected pore k , as follows

$$d_{mk}^{n+1} = | \mathbf{x}_m - \mathbf{x}_k |, \quad (4.43)$$

where \mathbf{x}_m and \mathbf{x}_k are the position vectors of pores m and k .

There are two different procedures in generating the throats connected to the newly merged pore. The first one applies to throats that connected pores i and j to a third pore that is not simultaneously connected to pores i and j . In this case, the throat properties just have to be updated. Otherwise, throat merging is carried out.

For the first procedure, the throats connected to the merged pore have the same volume, mass of acid, effective surface area, and effective conductance as before the merging process. In this way, the radii of the throats connected to the newly merged pore are updated considering their current volume and the new length, by

$$r_{mk}^{n+1} = \sqrt[2]{\frac{V_{mk}^{n+1}}{\pi l_{mk}^{n+1}}}. \quad (4.44)$$

The deformation of the throats during the merging process change the reactive surface area and conductance (see Fig. 4.9). The new surface area and conductance of the throats involved in the merging process, are determined, respectively by

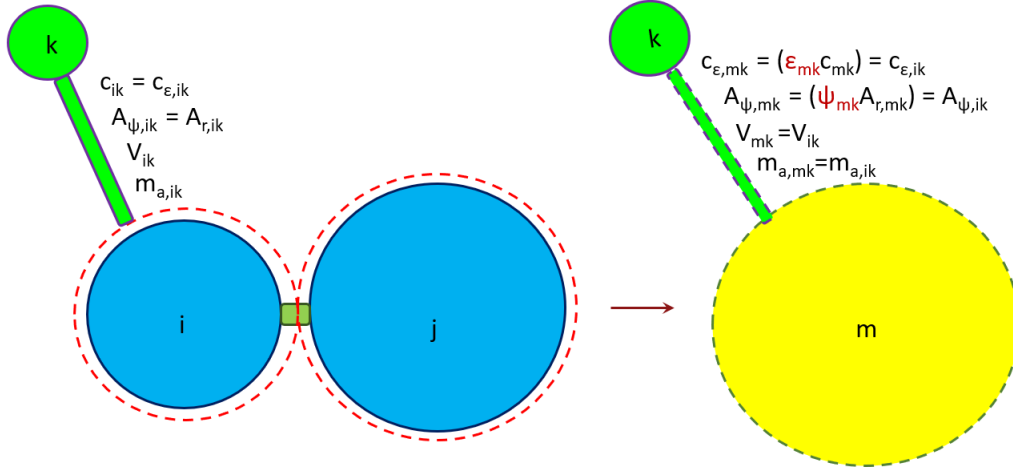


Figure 4.9: The volume, the mass of acid, the effective surface area, and the effective conductance are conserved for the new throat connecting the merged pore m and the connected pore k .

$$A_{r,mk}^{n+1} = 2\pi r_{mk}^{n+1} l_{mk}^{n+1}, \quad (4.45)$$

$$c_{mk}^{n+1} = \frac{\pi (r_{mk}^{n+1})^4}{8\mu_{mk}^{n+1}}. \quad (4.46)$$

At this stage, the correction factors for the surface area (ψ_{mk}) and for the conductance (ϵ_{mk}) are updated to maintain the correct effective surface areas and effective conductances of the throats during the merging process, by

$$\psi_{mk}^{n+1} = \frac{A_{\psi,ik}^{n+1}}{A_{r,mk}^{n+1}}, \quad (4.47)$$

$$\epsilon_{mk}^{n+1} = \frac{c_{\epsilon,ik}^{n+1}}{c_{mk}^{n+1}}. \quad (4.48)$$

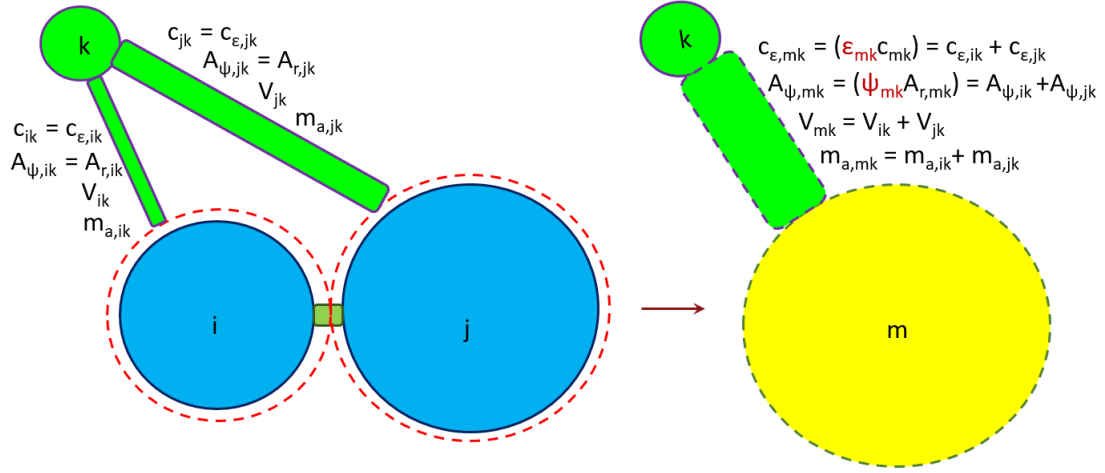


Figure 4.10: The merging pores are connected to the same pore k . In this case, one new throat, with the same total volume, mass of acid, effective surface area, and effective conductance as the two original throats, is created.

If the original pores were connected to the same pore, one new merged throat replaces the two original throats. So, the merged throat connected to the merged pore keeps the sum of the volume, mass of acid, effective surface area, and conductance of the replaced throats (see Fig. 4.10). The new throat length, radius, effective surface area, and effective conductance are also computed from Eqs. (4.42), (4.44), (4.45), and (4.46). Consequently, the correction factors are defined as

$$\psi_{mk}^{n+1} = \frac{A_{\psi,ik}^{n+1} + A_{\psi,jk}^{n+1}}{A_{r,mk}^{n+1}}, \quad (4.49)$$

$$\epsilon_{mk}^{n+1} = \frac{c_{\epsilon,ik}^{n+1} + c_{\epsilon,jk}^{n+1}}{c_{mk}^{n+1}}. \quad (4.50)$$

Finally, the reactive surface area of the new merged pore is updated considering its radius (r_m^{n+1}) and the new radii of the connected throats, using Eq. 3.25. Then, the correction factor to keep constant the effective surface area during the merging process is obtained by

$$\psi_m^{n+1} = \frac{A_{\psi,i}^{n+1} + A_{\psi,j}^{n+1}}{A_{r,m}^{n+1}}. \quad (4.51)$$

Note that the pores connected to the new merged pore also need their effective surface areas updated due to the changes in the radii of the connected throats during the merging process.

The merging approach presented here uses the merging method available at OpenPNM [74] to update the topology of the network. The method creates a new pore to replace the two original pores that are merging, deletes all throats connected to the two original pores, and creates new throats connecting the new merged pore to the pores previously connected to the original merging pores. Considering this, data from all pores and throats involved in the merging process are identified before calling the merge method from OpenPNM and relocated to new pores and throats after the use of the method.

Figure 4.11 presents a flowchart with the main steps of the novel merging methodology.

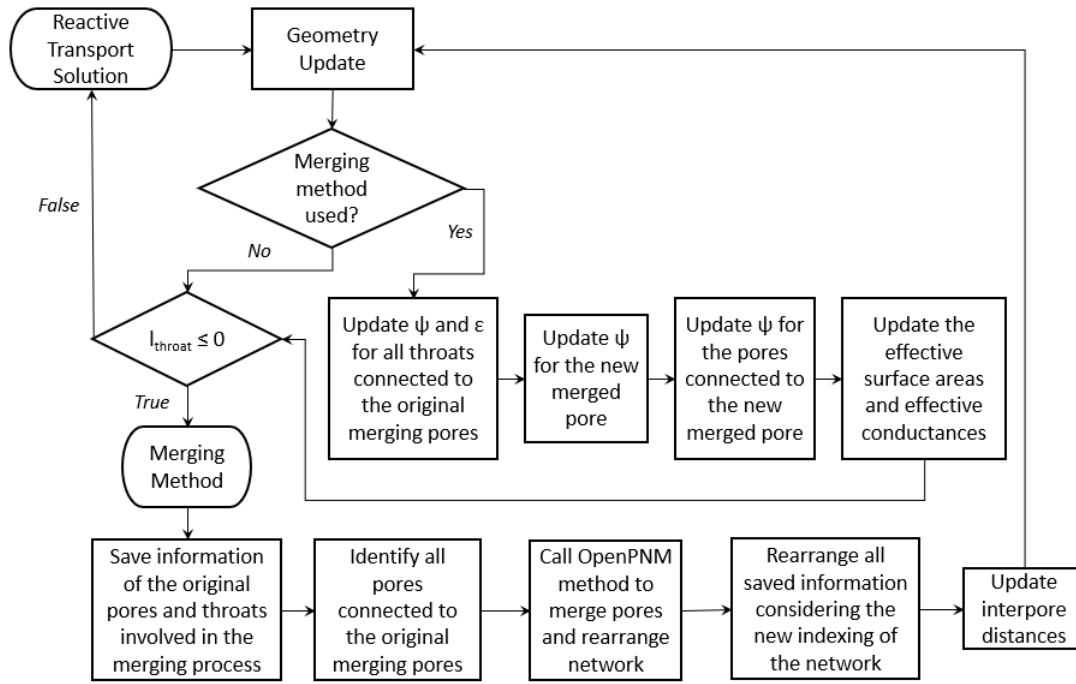


Figure 4.11: Flowchart of the novel methodology for merging of pores and throats. In summary, for each time step, after solving the reactive transport problem and the geometry update, merging conditions are evaluated and if it is necessary, the merging method is performed. Geometry update is also necessary after performing a merging process, and, for this case, correction factors must be updated.

4.2.6.1 Algorithm of the novel merging approach

The steps of the novel merging approach are described below:

1. Merging condition is satisfied.
2. Save geometric data of all original pores and throats involved in the merging process.
3. Call OpenPNM method for merging of pores and throats.

Note that this method deletes the two original merging pores and all connected throats, and after that creates a new merged pore and new connections between the new pore and the previous connected pores. This new pore spaces do not have any geometric information or any data from mass balance.

4. Update the radius of the new merged pore and all connected pores using Eq. 4.41.

5. Update the length of the new throats using Eq. 4.42.
6. New connected throat radii are obtained by Eq. 4.44, the surface areas are obtained by Eq. 4.45 and the conductances are obtained by Eq. 4.46.
7. Correction factors for the effective surface area and conductance of the connected throats are updated, respectively, using Eq. 4.47 and Eq. 4.48. If a new throat replaced two original throats, use Eqs.4.49 and 4.50.
8. Correction factors for the effective surface area of the new merged pore and connected pores are updated using Eq. 4.51
9. Effective surface area of pores and throats are updated using Eqs. 4.3 and 4.4.
10. Effective conductance of throats are updated using Eq. 4.1.

Remember that the correction factors are updated just after a change in the topology of the network, and that the effective properties are used during the entire simulation for flow and mass balance equations. Thus, for each time step, after the geometry update of the pore spaces, effective properties are determined using the actual correction factors.

4.2.7 Dimensionless numbers

The dimensionless numbers are described in section 3.2.4.

4.2.8 Quantitative criteria: a more robust approach

ESTEVEZ *et al.* [29] introduced the use of statistical approaches to classify the dissolution regimes. Here, a novel approach more generic and considering dimensionless parameters is proposed.

The network is partitioned in N_{cs} volumes in the flow direction. Each pore space that has its center within a partition volume it is said to belong to this partition. Thus, some statistical quantities can be calculated for each cross-sectional partition.

The coefficient of variation (CV) is a unit-free measure of the dispersion of a data set that uses the standard deviation and the mean values [80]. The CV is used to evaluate the variation of the acid concentration profile within the network. Considering the definition of standard deviation (see Eq. (4.53)), the CV is determined for each network cross-section partition (CV_{cs}) by Eq. (4.54), where N_{ps} is the total number of pores and throats (identified by the subscript ps , derived from pore space) belonging to partition cs , σ_{cs} is the standard deviation of cross section cs , $C_{a,ps}$ is the acid concentration of the pore space ps , and $\overline{C_{a,cs}}$ is the average concentration of acid of all pore spaces within cross section cs (see Eq. (4.52)). The CV for each simulation condition is defined then by Eq. (4.55), where $\overline{CV_{cs}}$ is the average of all CV_{cs} .

$$\overline{C_{a,cs}} = \frac{1}{N_{ps}} \sum_{ps=1}^{N_{ps}} C_{a,ps}. \quad (4.52)$$

$$\sigma_{cs} = \sqrt{\frac{1}{N_{ps}} \sum_{ps=1}^{N_{ps}} (C_{a,ps} - \overline{C_{a,cs}})^2}. \quad (4.53)$$

$$CV_{cs} = \frac{\sigma_{cs}}{\overline{C_{a,cs}}}. \quad (4.54)$$

$$CV = \overline{CV_{cs}} = \frac{1}{N_{cs}} \sum_{cs=1}^{N_{cs}} CV_{cs} \quad (4.55)$$

The measure of the extension of the acid along the network in the flow direction is characterized by the parameter ΔC , that is defined by Eq. (4.56), where $C_{a,in}$ is the inlet acid concentration and $C_{a,out}$ is the acid concentration in the outlet pore.

$$\Delta C = \left| \frac{C_{a,in} - C_{a,out}}{C_{a,out}} \right| \quad (4.56)$$

Hence, these two parameters, CV and ΔC are used to identify the dissolution regimes. The preferential pathways dissolution regime, characterized by the formation of very conductive channels where acid flows preferentially, is identified by a large CV . This means that acid concentration of pores and throats within the same cross section varies significantly. The surface dissolution regime is characterized by a more homogeneous spread of the acid along the cross sections perpendicular to the flow and is identified by a small CV (small dispersion of the values of acid concentration in each cross section) and a high ΔC . The high ΔC identifies the consumption of the acid along the network due to the large reactivity of this dissolution regime. Finally, uniform dissolution is described by small values of CV and ΔC , that identify a regime that the acid concentration is homogeneous within the cross sections and the consumption is nearly uniform in the entire domain due to the small reactivity of this dissolution regime.

4.3 Results and discussion

Simulations of reactive transport and mineral dissolution are performed in different networks to show the applicability of the methodology for a wide range of systems.

A concentration of 10 kg/m^3 of acid is injected from the left-hand side of the network (one-dimensional flow in the positive x direction) at a constant volumetric flow rate corresponding to a $Re \approx 0.1$. Fluid and solid properties are set to $\mu_f = 10^{-3} \text{ Pa.s}$, $\rho_f = 1000 \text{ kg/m}^3$ and $\rho_{solid} = 2165 \text{ kg/m}^3$. The stoichiometric coefficient that relates the consumed acid species with the consumed solid reactive mineral is set to $\beta = 1.37$, based on molar masses (M) and stoichiometric coefficients of Eq. (3.10) ($M_{CaCO_3}/2M_{HCl}$). An analysis of the mass balance errors in the simulations are presented in Appendix B.

Simulation conditions were explored based on the dimensionless numbers Pe , Da , and $PeDa$. Reaction rate constant and diffusivity were adjusted to reach

the desired conditions.

Table 4.2: Simulation conditions explored based on the dimensionless numbers Pe , Da , and $PeDa$.

Condition	Expected regime	Pe	Da	$PeDa$
1	Preferential pathways	100	2	200
2	Surface dissolution	10^{-5}	2	2×10^{-5}
3	Uniform dissolution	100	0.05	5
4	Uniform dissolution	10^{-5}	0.05	5×10^{-7}

4.3.1 Effects of using correction factors

The objective of this section is to show the importance of the use of correction factors in stick-and-ball pore network models. One of the main important pieces of information transferred from pore-scale to larger scales is the permeability versus porosity curves. This type of curve is a constitutive relationship for reservoir simulations that relates the evolving permeability based on the increase of the porosity of the porous medium.

Figure 4.12 presents an example of the permeability versus porosity curves obtained for simulations not considering the use of the correction factors (in red) and considering the use of correction factors (in blue) in a 40x40 network. The use of correction factors enables a continuous curve of the evolution of permeability and porosity of the network under dissolution condition. The deformation of the original pore spaces due to the merging hypothesis shows to impact significantly the behavior of the $K - \phi$ curve. This means that, the new methodology proposed here helps in the construction of a more accurate physical description of the evolving of a porous medium under reactive transport and mineral dissolution processes and generates more reliable input information for

larger scale simulations.

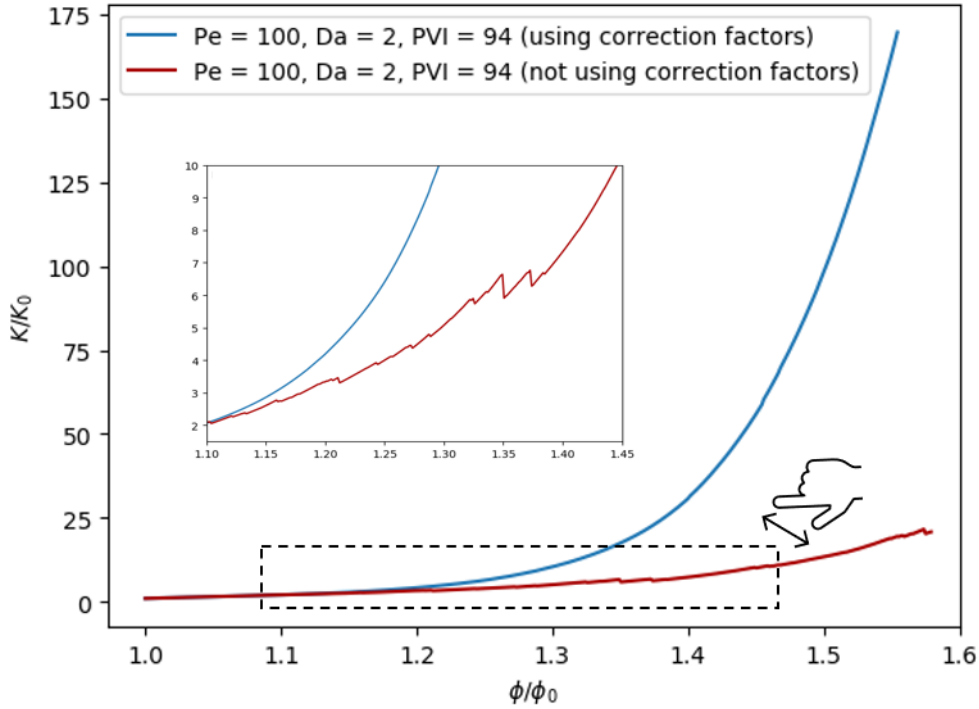


Figure 4.12: Permeability versus porosity curves obtained for simulations not considering the use of correction factors (red curve) and the use of correction factors (blue curve). The use of correction factors enables a continuous evolution of permeability and porosity of the network under dissolution conditions (see inset that is magnified). The deformation of the original pore spaces due to the merging hypothesis impacts significantly the behavior of the $K - \phi$ curves.

4.3.2 Application in two-dimensional networks

This section aims to show the applicability of the methodology for two-dimensional networks.

Figure 4.13 presents the acid concentration profile at the end of simulations in the 10x10 network. The expected dissolution regime for each simulation case is observed. Preferential pathways are observed in the upper region of the network for Condition 1 (see Fig. 4.13a). Surface dissolution is characterized by a homogeneous high acid consumption along the network for Condition 2 (see Fig. 4.13b). Uniform dissolution regime is observed for Conditions 3 and 4 (see Fig 4.13c and 4.13d) by a uniform and large spread of the acid throughout the entire network.

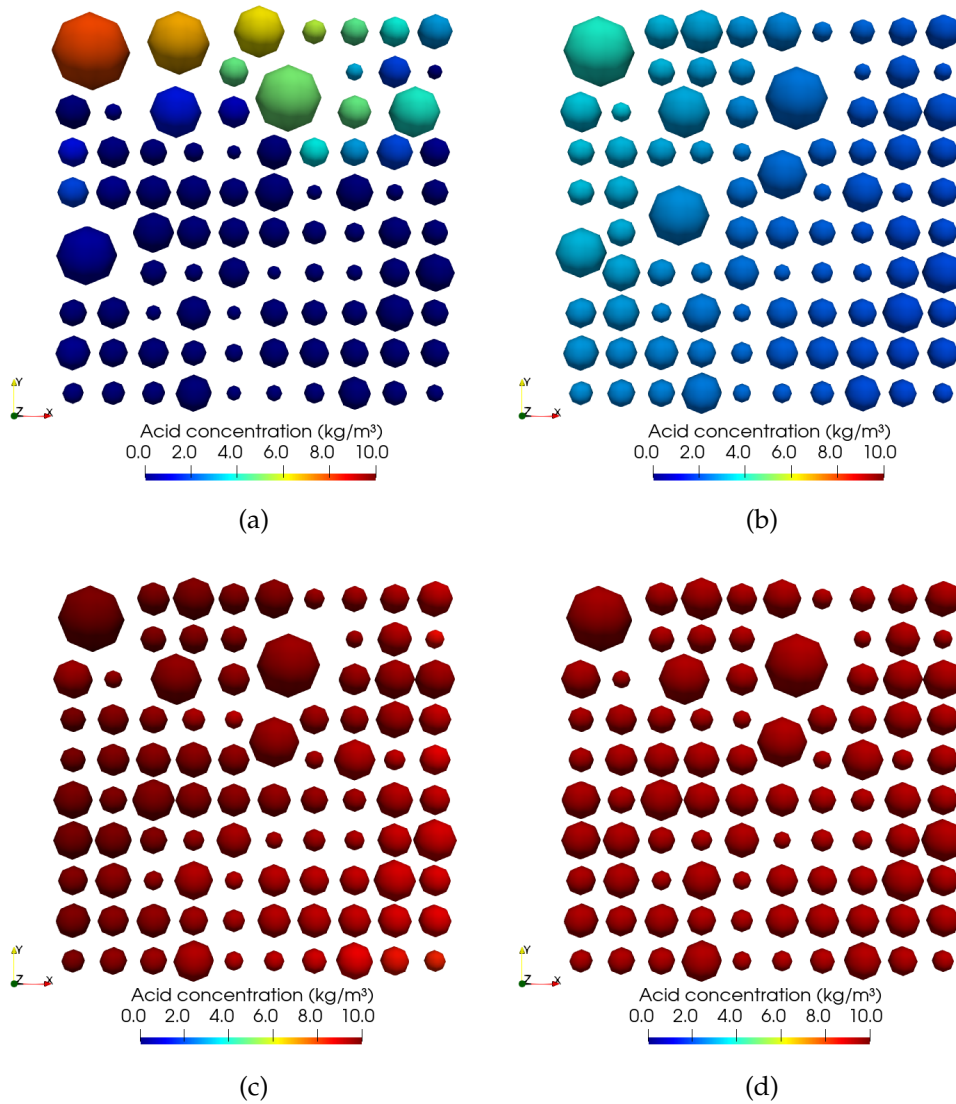


Figure 4.13: Acid concentration profile at the end of simulation for the 10x10 network. (a) Condition 1, characterized by a preferential pathways regime, after 111 PVI. (b) Condition 2, characterized by a surface dissolution regime, after 111 PVI. (c) Condition 3, characterized by a uniform dissolution regime, after 1323 PVI. (d) Conditions 4, characterized by a uniform dissolution regime, after 1323 PVI.

Figure 4.14 presents the permeability versus porosity curves obtained for simulations in the 10x10 network. The preferential pathways regime presents the largest increase of the permeability (blue curve) while the surface dissolution presents the largest increase of porosity (orange curve). Uniform dissolution curves (green and red curves) present intermediate behavior. The observed behaviors are expected as previously described in the literature, but note that, the increases observed in Fig. 4.14 are reaching values larger than 100 times of the

initial permeability of the network. These results are just possible because of the ability of the algorithm to merge pores and calculate conductance smoothly and accurately during the dissolution of the porous medium, enabling a more accurate representation of what happens in real porous media using a simplified stick-and-ball pore-network model.

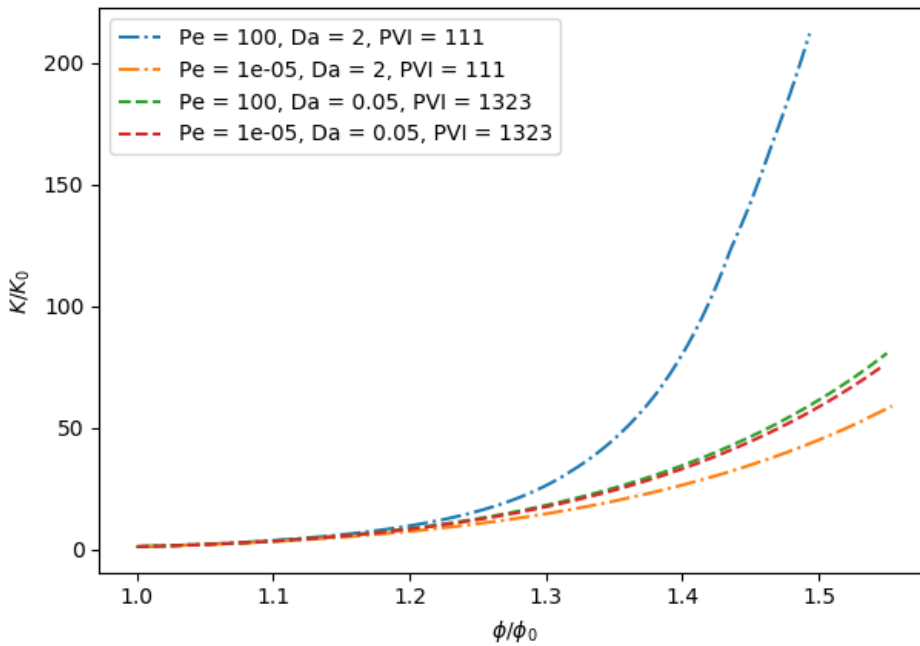


Figure 4.14: Permeability versus porosity curves obtained for simulations in the 10x10 network.

Figure 4.15 presents the acid concentration profile at the end of simulations in the 20x20 network. The idea here is to demonstrate that the behaviors expected for each simulation case are also reproduced in larger networks. Moreover, in larger domain sizes, the characteristic behavior of the dissolution regimes are highlighted. Figure 4.15a, for example, shows clear formation of a preferential pathway in the upper side of the network in contrast to the middle and lower regions of network that presents small amount of acid.

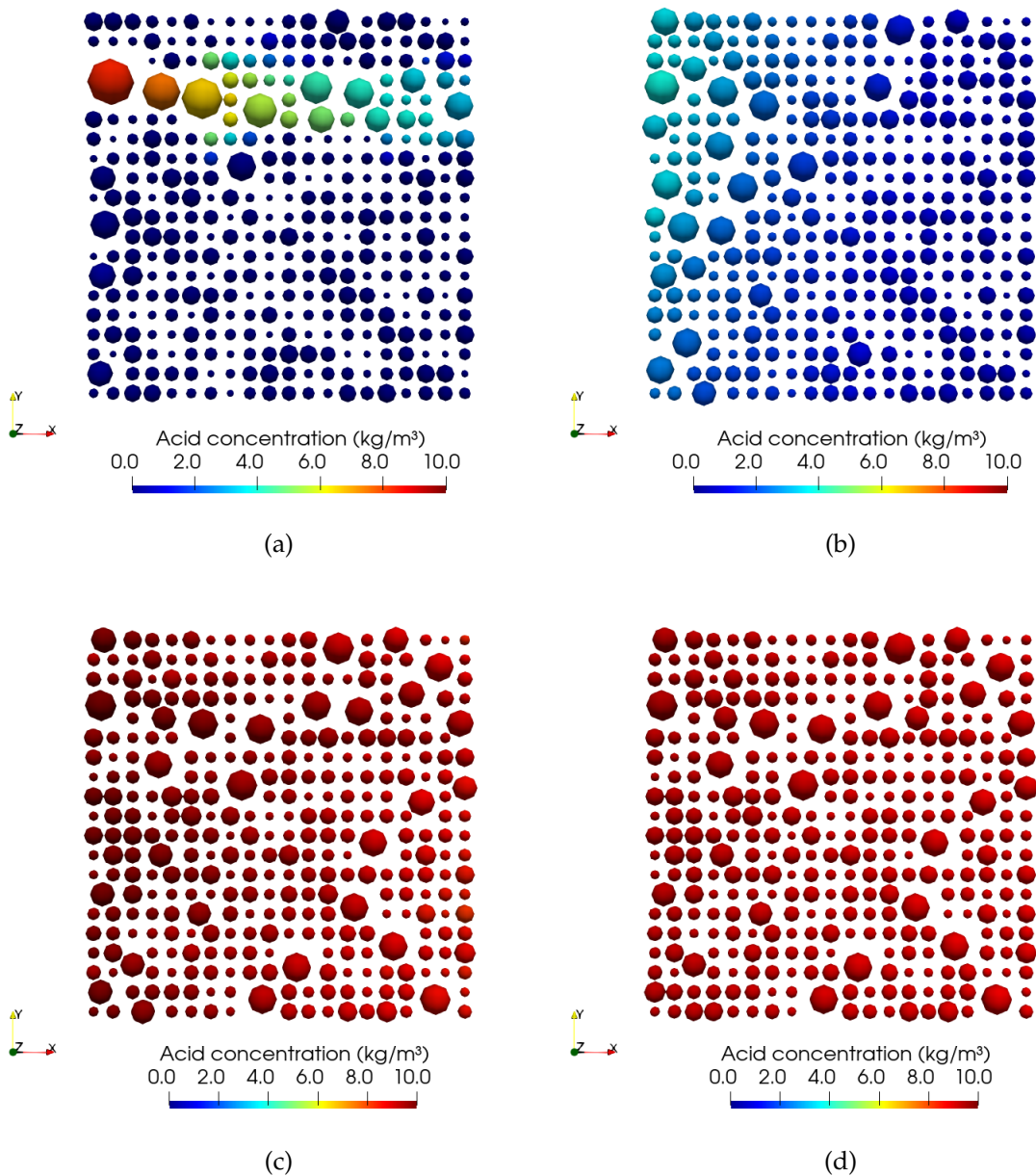


Figure 4.15: Acid concentration profile at the end of simulation for the 20x20 network. (a) Condition 1, characterized by a preferential pathways regime, after 88 PVI. (b) Condition 2, characterized by a surface dissolution regime, after 88 PVI. (c) Condition 3, characterized by a uniform dissolution regime, after 876 PVI. (d) Condition 4, characterized by a uniform dissolution regime, after 876 PVI.

Figure 4.16 presents the flow rate profile for Condition 1, characterized by a preferential pathways regime, after 88 PVI in the 20x20 network. The path with the greatest flow rates in the network corroborates the location of the preferential pathways formed during the simulation of Condition 1.

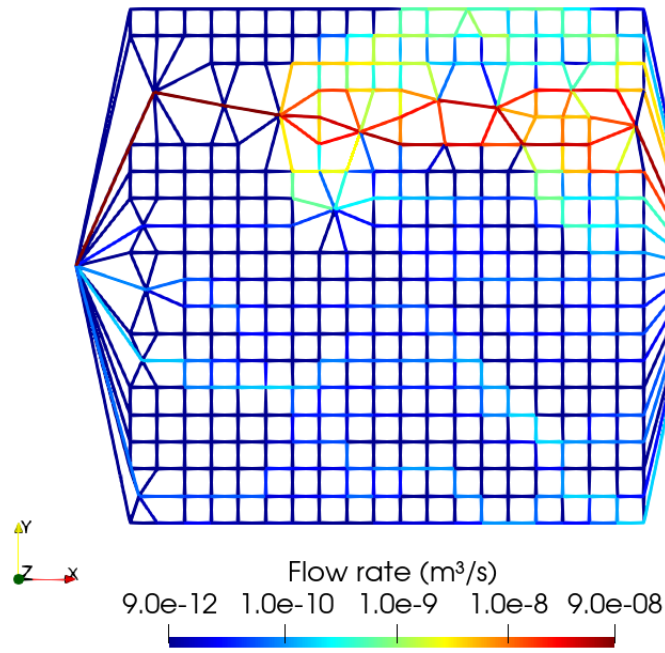


Figure 4.16: Flow rate profile for Condition 1, characterized by a preferential pathways regime, after 88 PVI in the 20x20 network.

Figure 4.17 presents the permeability versus porosity curves obtained for simulations in the 20x20 network, reproducing the behaviors described for simulation in the 10x10 network.

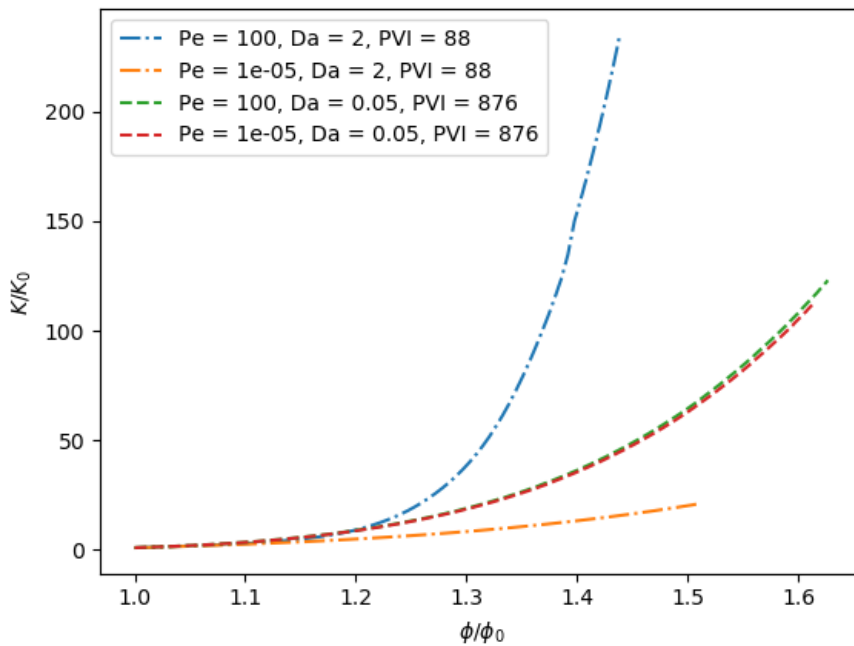


Figure 4.17: Permeability versus porosity curves obtained for simulations in the 20x20 network.

Finally, Figure 4.18 presents the acid concentration profile at the end of simulations in the 40x40 network. The expected behavior for each simulation case is reproduced for the 40x40 network.

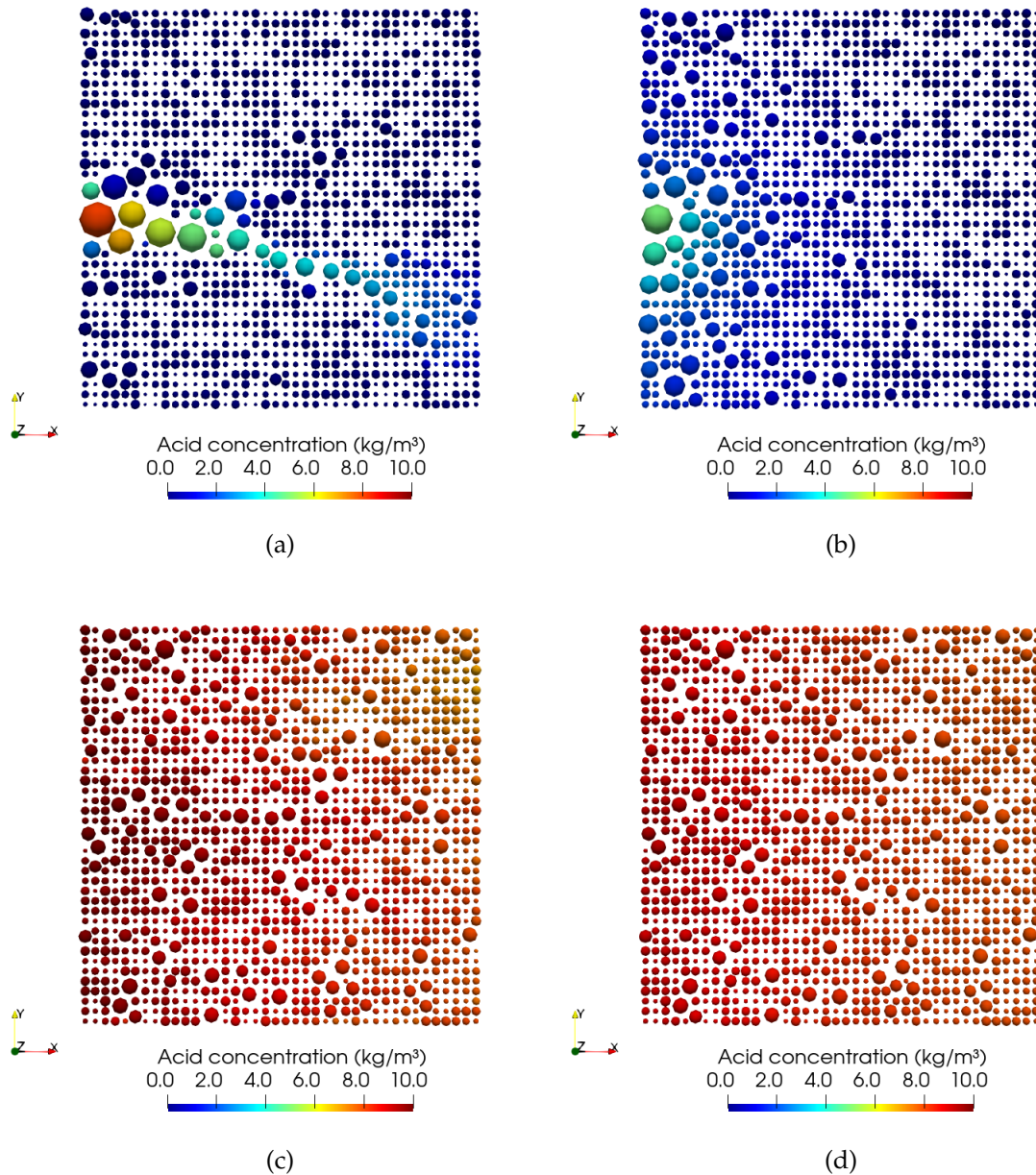


Figure 4.18: Acid concentration profile at the end of simulation for the 40x40 network. (a) Case 1, characterized by a preferential pathways regime, after 94 PVI. (b) Condition 2, characterized by a surface dissolution regime, after 94 PVI. (c) Conditions 3, characterized by a uniform dissolution regime, after 450 PVI. (d) Condition 4, characterized by a uniform dissolution regime, after 450 PVI.

Figure 4.19 illustrates the complex flow rate profile for Condition 1, characterized by a preferential pathways regime, after 94 PVI in the 40x40 network.

Ramifications of the wormhole are clearly seen.

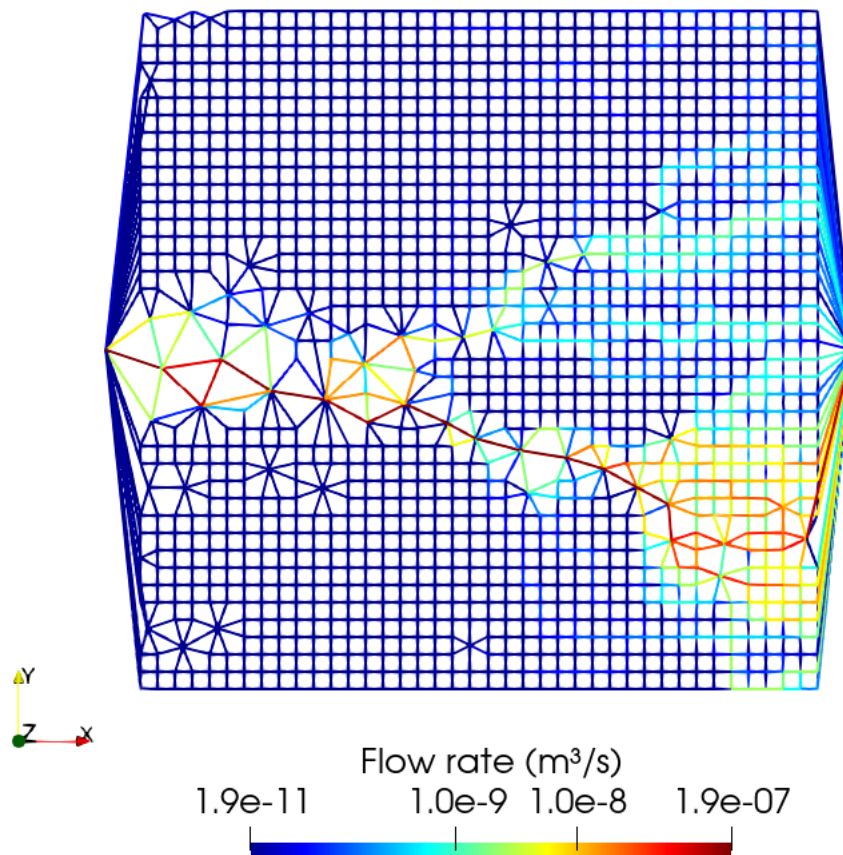


Figure 4.19: Flow rate profile for Condition 1, characterized by a preferential pathways regime, after 94 PVI in the 40x40 network.

Figure 4.20 presents the permeability versus porosity curves obtained for simulations in the 40x40 network, reproducing similar behaviors described for simulations in the 10x10 and 20x20 network. Here, otherwise, it is possible to see that the curve of preferential pathways dissolution regime needs more porosity increase than the uniform dissolution curves to reach the largest permeability increase. This fact demonstrates the possible differences in behaviors for networks with different characteristics lengths and the importance to take into account the heterogeneity of the porous medium when discussing observed results.

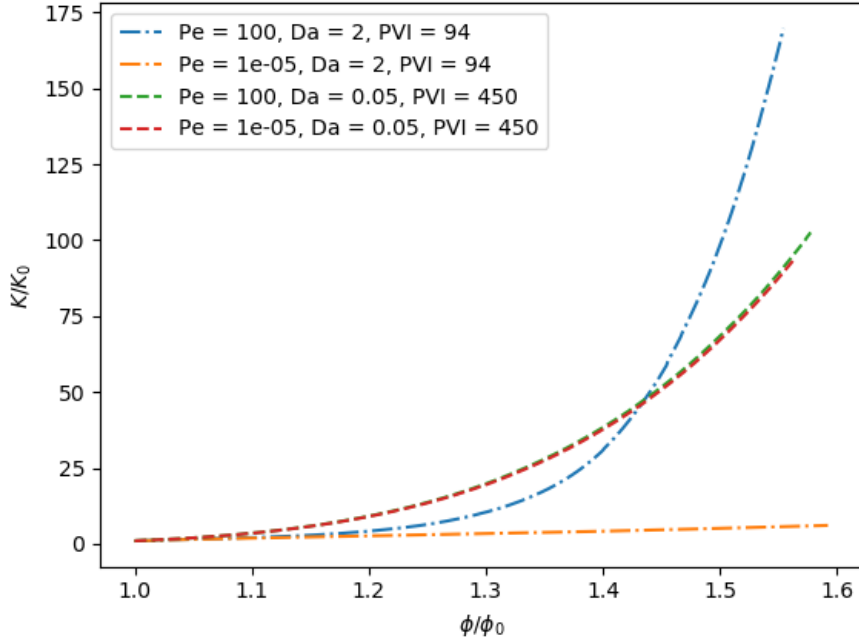


Figure 4.20: Permeability versus porosity curves obtained for simulations in the 40x40 network.

A power-law form is generally used to represent the relationship between the logarithmic of the K/K_0 and the logarithmic of ϕ/ϕ_0 . Table 4.3 presents the power-law exponents and coefficients of determination (R^2) obtained for the simulations in the two-dimensional networks.

Table 4.3: Power-law exponents and coefficients of determination (R^2) obtained for the simulations in the two-dimensional networks.

Network		10x10	20x20	40x40
Case	Observed regime	Exponent (R^2)	Exponent (R^2)	Exponent (R^2)
1	Preferential pathways	12.9 (0.996)	14.1 (0.978)	10.3 (0.953)
2	Surface dissolution	9.8 (0.982)	7.9 (0.972)	4.3 (0.902)
3	Uniform dissolution	10.6 (0.984)	10.6 (0.980)	10.8 (0.981)
4	Uniform dissolution	10.5 (0.985)	10.5 (0.981)	10.8 (0.982)

The surface dissolution regime is identified by the smallest power-law expo-

nents. This means that the increase of permeability is limited for a limited porosity variation. Note that in this regime most of the changes in volume happens around the inlet area where most of the acid is already consumed. Moreover, it is possible to see that the exponent values decrease as the network work size increases.

The formation of preferential pathways leads to sharp increases of the permeability for a limited porosity variation and, consequently, is identified by the largest values of the power-law coefficients. The simulation results in the 40x40 network present an exception to this conclusion, and the uniform dissolution cases present the largest values of the exponents. This can be explained by low values of the R^2 that shows that the power-law form can not be the best form to represent the behavior of the permeability versus permeability curves.

The uniform dissolution regime, in general, presents intermediate behavior of the curves compared to the preferential pathways regime and the the surface dissolution regime.

4.3.2.1 Demonstration of the evolution of the correction factors

This section presents the final profile of the correction factors simulating Condition 1 in the 20x20 and 40x40 networks. The objective here is to show the the magnitude of the values necessary to correct the deformation of the pore spaces and conserve the main important properties for the reactive transport and mineral dissolution simulations.

Figure 4.21 presents the final profile of the correction factor for the effective surface area of pores (ψ_i) considering Case 1, characterized by a preferential pathways dissolution regime, simulated in the 20x20 (Fig. 4.21a) and 40x40 (Fig. 4.21b) networks. It is possible to see that the correction factors that were modified are located around the preferential pathway and the pore spaces that suffered a merging process. Note that the maximum values of ψ_i are approximately twice the original values.

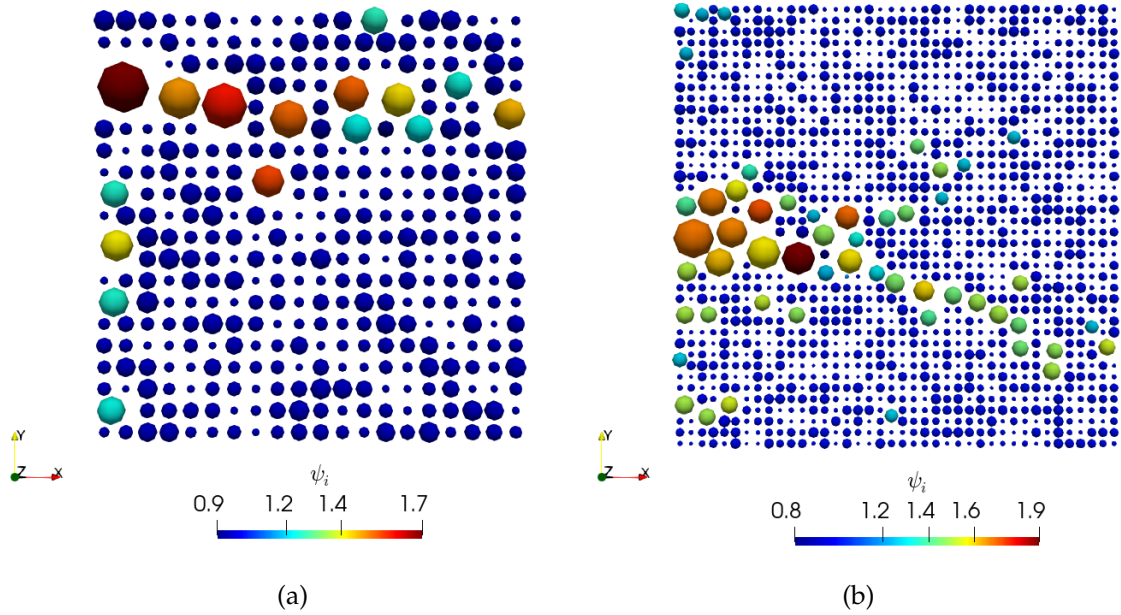


Figure 4.21: Final profile of the correction factor for the effective surface area of pores (ψ_i) considering Case 1, characterized by a preferential pathways dissolution regime. (a) Simulation in the 20x20 network after 111 PVI. (b) Simulation in the 40x40 network after 88 PVI.

Figure 4.22 presents the final profile of the correction factor for the effective surface area of throats (ψ_{ij}) considering Case 1, characterized by a preferential pathways dissolution regime, simulated in the 20x20 (Fig. 4.22a) and 40x40 (Fig. 4.22b) networks. It is possible to see that the correction factors that were modified are located around the preferential pathway and the pore spaces that suffered a merging process. The values of ψ_{ij} are approximately in the $[0.1, 3.2]$ range.

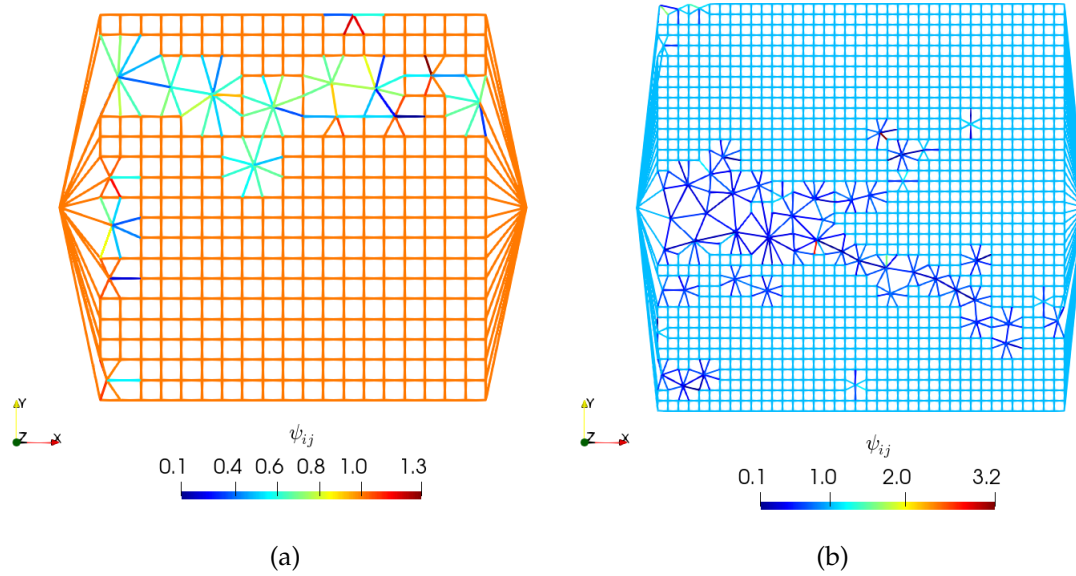


Figure 4.22: Final profile of the correction factor for the effective surface area of throats (ψ_{ij}) considering Condition 1, characterized by a preferential pathways dissolution regime. (a) Simulation in the 20x20 network after 111 PVI. (b) Simulation in the 40x40 network after 88 PVI.

Figure 4.23 presents the final profile of the correction factor for the effective conductance of throats (ϵ_{ij}) considering Case 1, characterized by a preferential pathways dissolution regime, simulated in the 20x20 (Fig. 4.23a) and 40x40 (Fig. 4.23b) networks. Here, the value of ϵ_{ij} span eleven of magnitude. It can be greater than 10^8 times the original values. These results highlight the impact of the deformation of throats during the merging process, that impacts directly the permeability of the network, and the importance in considering correction factors to conserve the evolution of the conductance profile along the network.

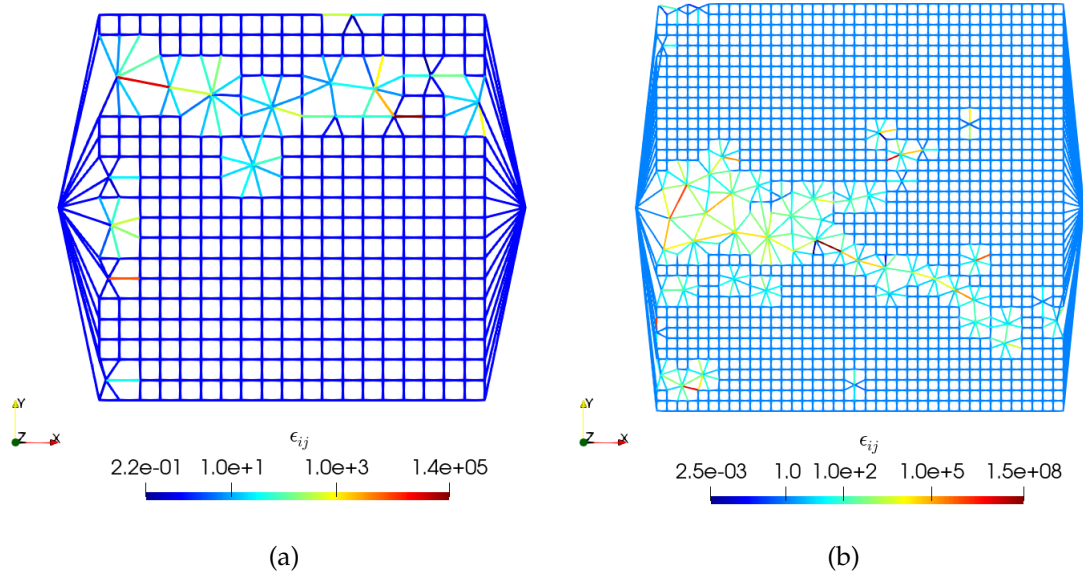


Figure 4.23: Final profile of the correction factor for the effective conductance of throats (ϵ_{ij}) considering Case 1, characterized by a preferential pathways dissolution regime. (a) Simulation in the 20x20 network after 111 PVI. (b) Simulation in the 40x40 network after 88 PVI.

4.3.3 Application in a regular three-dimensional network

This section shows the applicability of the methodology for simulations in three-dimensional networks.

Figure 4.24 presents the acid concentration profile at the end of simulations in the 10x10x10 network. The expected dissolution regime for each simulation case is observed. Preferential pathways are observed in the middle region of the network for Condition 1 (see Fig. 4.24a). Surface dissolution is characterized by a homogeneous high acid consumption along the network for Condition 2 (see Fig. 4.24b). The uniform dissolution regime is observed for Conditions 3 and 4 (see Figs. 4.24c and 4.24d) by a uniform and large spread of the acid throughout the entire network.

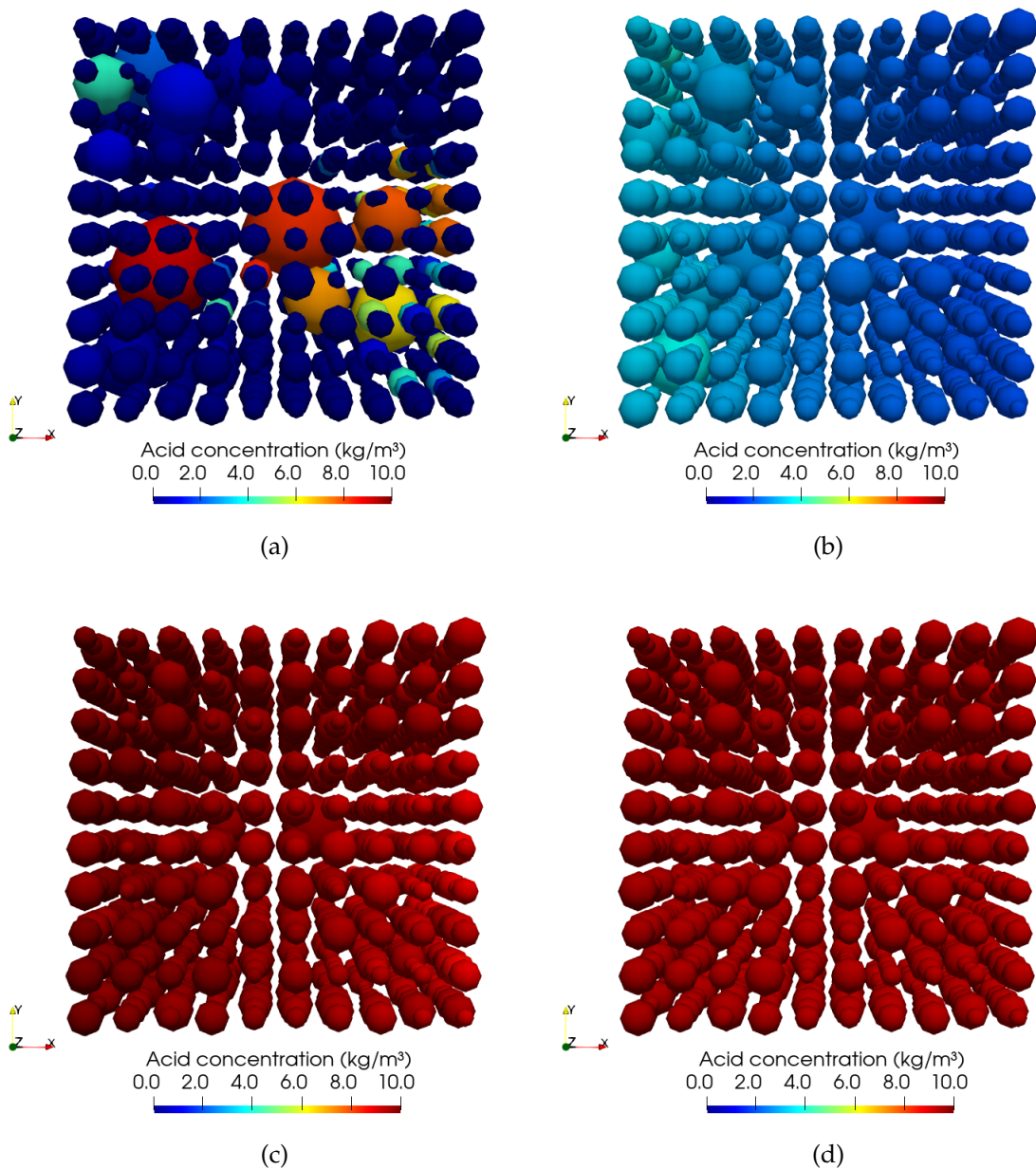


Figure 4.24: Acid concentration profile at the end of simulation for the 10x10x10 network. (a) Condition 1, characterized by a preferential pathways regime, after 111 PVI. (b) Condition 2, characterized by a surface dissolution regime, after 111 PVI. (c) Condition 3, characterized by a uniform dissolution regime, after 1037 PVI. (d) Condition 4, characterized by a uniform dissolution regime, after 1037 PVI.

Figure 4.25 presents the permeability versus porosity curves obtained for simulations in the 10x10x10 network, reproducing similar behaviors described for simulations in the two-dimensional networks. Here, it is possible to see an increase of the permeability for the preferential pathways regime that reached 600 times the initial permeability value, while for the surface dissolution regime

the increase of permeability is significantly limited.

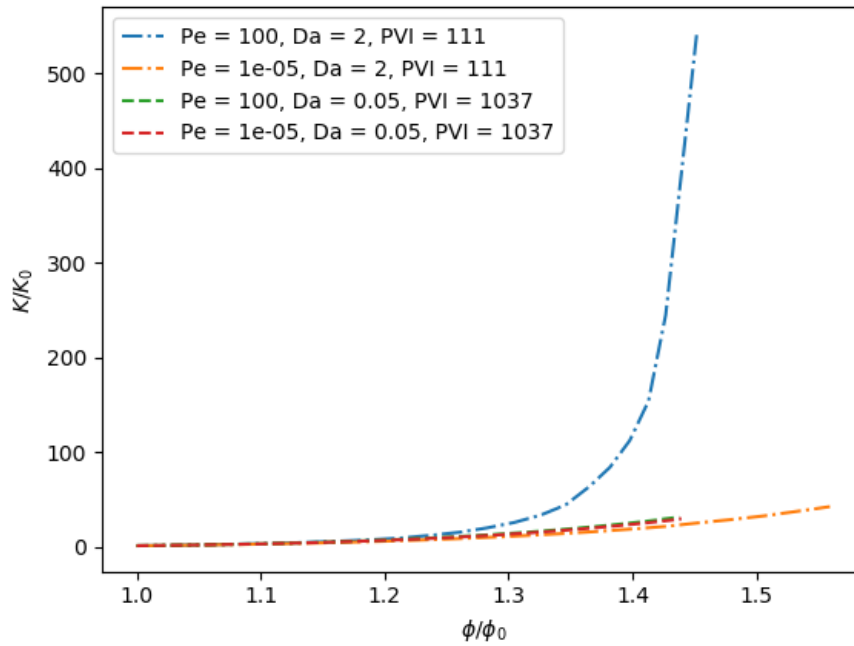


Figure 4.25: Permeability versus porosity curves obtained for simulations in the $10 \times 10 \times 10$ network.

Table 4.4 presents the power-law exponents and coefficients of determination (R^2) obtained for the simulations in the regular three-dimensional network. Surface dissolution regime is identified by the smallest power-law exponent while the formation of preferential pathways is identified by the largest value of the power-law exponent. The uniform dissolution regimes present a intermediate values of the power-law exponents.

Table 4.4: Power-law exponents and coefficients of determination (R^2) obtained for the regular three-dimensional network.

Case	Observed regime	Exponent (R^2)
1	Preferential pathways	13.9 (0.936)
2	Surface dissolution	8.8 (0.988)
3	Uniform dissolution	10.0 (0.989)
4	Uniform dissolution	9.8 (0.989)

4.3.4 Application in a random three-dimensional network

This section aims to show the applicability of the methodology for simulations in three-dimensional random networks.

Figure 4.26 presents the acid concentration profile at the end of simulations in the three-dimensional random network. The expected dissolution regime for each simulation condition is observed. Preferential pathways are observed in the upper region of the network for Condition 1 (see Fig. 4.26a). Surface dissolution is characterized by a homogeneous high acid consumption along the network for Condition 2 (see Fig. 4.26b). Uniform dissolution regime is observed for Conditions 3 and 4 (see Figs. 4.26c and 4.26d) by a uniform and large spread of the acid throughout the entire network. The pores with small acid concentration in Fig. 4.26c are in the inlet and outlet regions, and are mostly connected to pores in the same region. In this way, they are under the same pressure and as diffusion in this condition is very low, acid couldn't be transported to this specific pores.

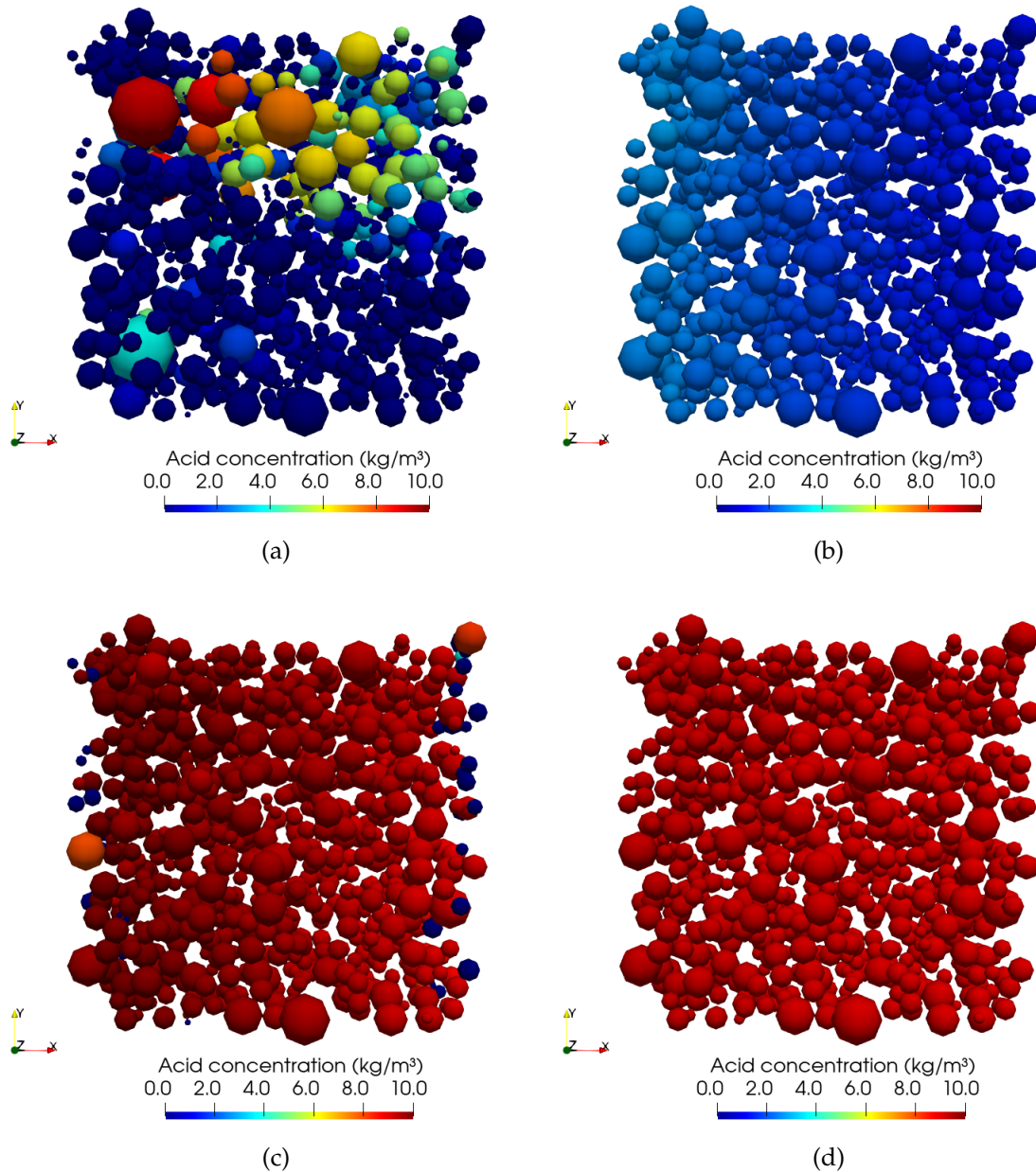


Figure 4.26: Acid concentration profile at the end of simulation for the three-dimension random network. (a) Condition 1, characterized by a preferential pathways regime, after 135 PVI. (b) Condition 2, characterized by a surface dissolution regime, after 135 PVI. (c) Condition 3, characterized by a uniform dissolution regime, after 1212 PVI. (d) Condition 4, characterized by a uniform dissolution regime, after 1212 PVI.

Figure 4.27 presents the permeability versus porosity curves obtained for simulations in the random network, reproducing similar behaviors described for simulations in the two-and-three dimensional regular networks.

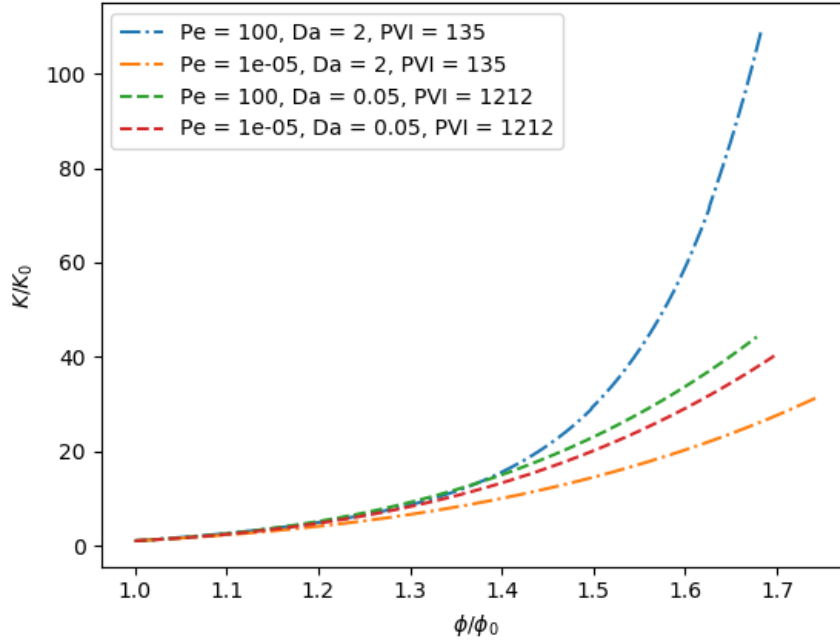


Figure 4.27: Permeability versus porosity curves obtained for simulations in the three-dimensional random network.

Table 4.5 presents the power-law exponents and coefficients of determination (R^2) obtained for the simulations in the random three-dimensional network. The surface dissolution regime is identified by the smallest power-law exponent while the formation of preferential pathways is identified by the largest value of the power-law exponent.

Table 4.5: Power-law exponents and coefficients of determination (R^2) obtained for the random three-dimensional network.

Case	Observed regime	Exponent (R^2)
1	Preferential pathways	8.5 (0.993)
2	Surface dissolution	6.6 (0.978)
3	Uniform dissolution	7.8 (0.981)
4	Uniform dissolution	7.5 (0.982)

4.3.5 Special case of a network generated using a carbonate topology

This section aims to show the possibility to use the merging methodology for very heterogeneous networks.

Figure 4.28 presents the acid concentration profile at the end of simulations in the carbonate network. The expected dissolution regime for each simulation condition is observed. Here, there is the formation of different preferential pathways due to the significant heterogeneity of the system for Condition 1 (see Fig. 4.28a). Surface dissolution is characterized by a homogeneous and large acid consumption along the network for Condition 2 (see Fig. 4.28b). Uniform dissolution regime is observed for Conditions 3 and 4 (see Figs. 4.28c and 4.28d) by a high spread of the acid throughout the entire network. There are many pores with small acid concentration in Fig. 4.28c, Condition 3, and this is a consequence of the large heterogeneity of the network, and consequently the presence of some restricted pore spaces, and a very low diffusivity that is necessary to reach high values of Peclet number.

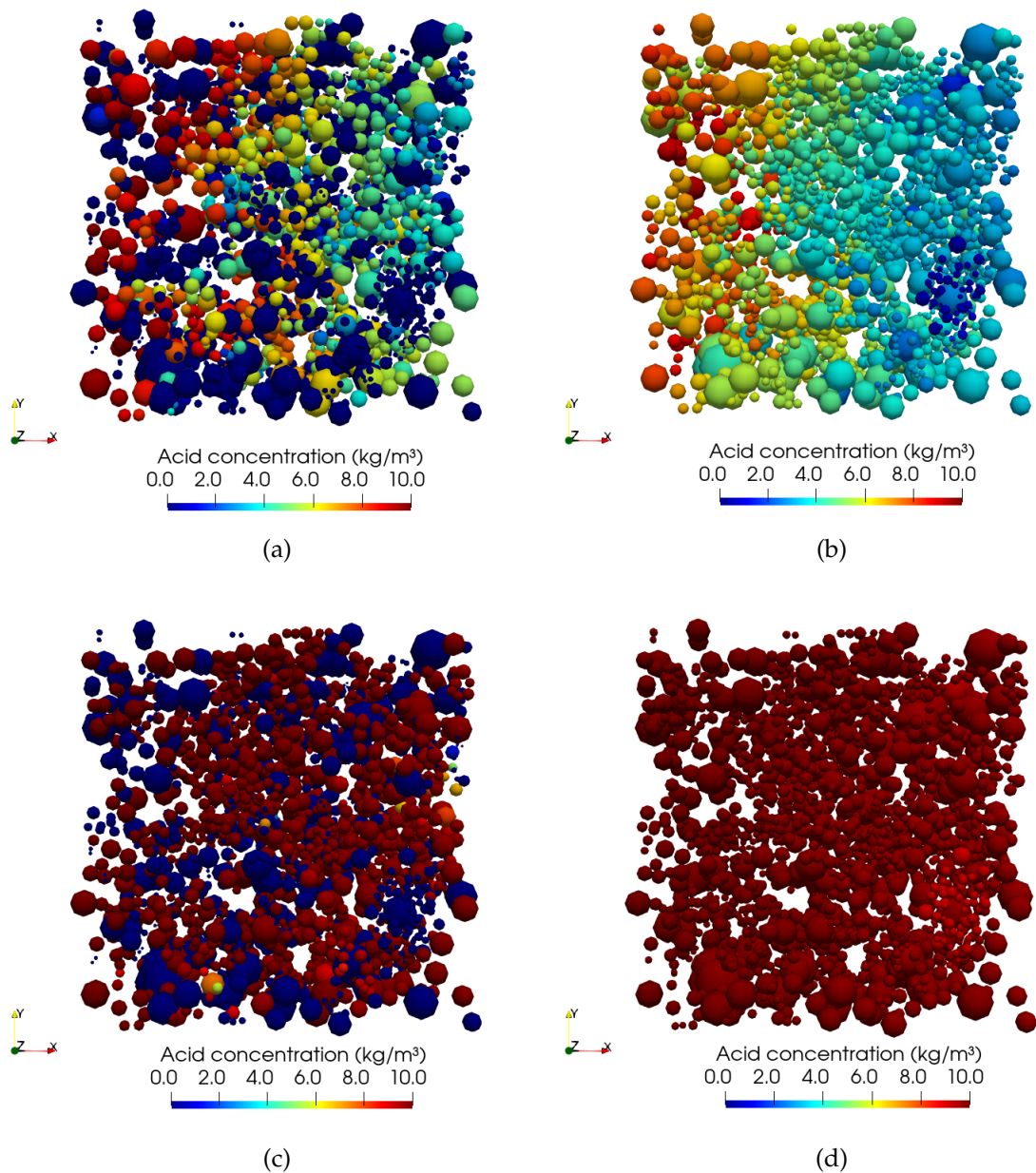


Figure 4.28: Acid concentration profile at the end of simulation for the carbonate-derives network. (a) Condition 1, characterized by a preferential pathways regime, after 186 PVI. (b) Condition 2, characterized by a surface dissolution regime, after 139 PVI. (c) Condition 3, characterized by a uniform dissolution regime, after 4182 PVI. (d) Condition 4, characterized by a uniform dissolution regime, after 2788 PVI.

Figure 4.29 presents the permeability versus porosity curves obtained for simulations in the carbonate network. The general trends are observed, although the curve of the surface dissolution regime (in orange) presents a larger slope than the curve of the uniform dissolution with the same small Peclet number (in red). This behavior is explained by the small value of permeability of this network

and its significant heterogeneity. For this case, preferential dissolution in the inlet area of the network is helping in the increase of the overall permeability of the network, considering that this area presents a significant restriction to the flow.

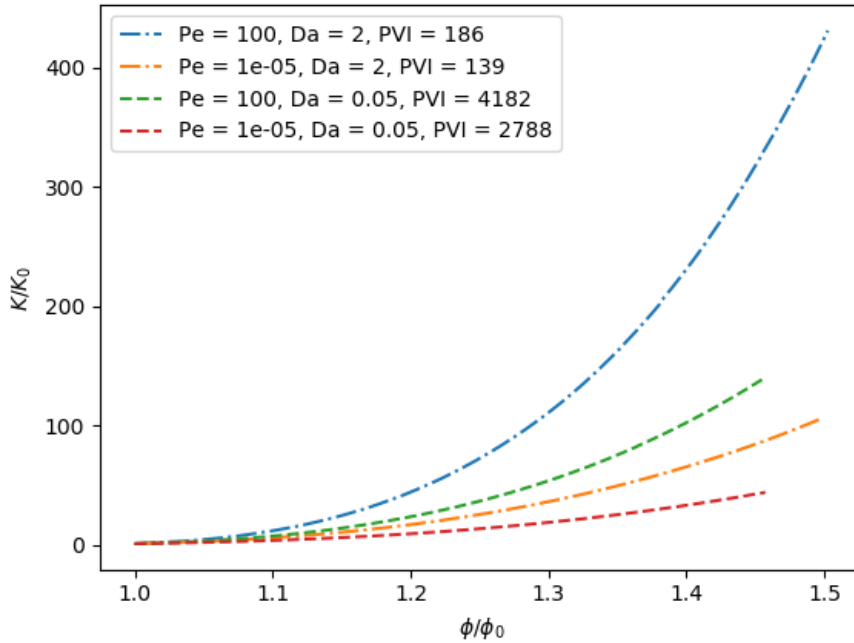


Figure 4.29: Permeability versus porosity curves obtained for simulations in the carbonate-derived network.

Table 4.6 presents the power-law exponents and coefficients of determination (R^2) obtained for the simulations in the carbonate network. The smallest power-law exponent reflects the porosity-permeability behavior for Condition 4. The largest value of the power-law exponent is related to the curve of the preferential pathways. Again, considering the poor adjustment of the curves, specially for Condition 1, the power-law seems not to be ideal for all simulation cases. This highlight the importance of using pore-scale simulations to observe better the behavior of the evolving of porosity and permeability in a porous medium.

Table 4.6: Power-law exponents and coefficients of determination (R^2) obtained for the carbonate-derived network.

Case	Observed regime	Exponent (R^2)
1	Preferential pathways	17.2 (0.874)
2	Surface dissolution	13.1 (0.911)
3	Uniform dissolution	15.1 (0.911)
4	Uniform dissolution	11.1 (0.964)

4.3.6 Statistical parameters analysis

Here, the statistical parameters obtained to identified the dissolution regimes are presented.

Table 4.7 presents the statistical parameter CV and Table 4.8 presents the statistical parameter ΔC obtained for all the reactive transport and mineral dissolution simulations. Note that the results reflect the final acid concentration profiles and that the increase of porosity observed for all simulations reached, at least, 40%.

Preferential pathways are identified by the largest values of CV and, consequently, the largest variance in the values of acid concentration within each cross section of the network. Based on the simulation results, preferential pathways are identified by a $CV > 1$.

Table 4.7: Statistical parameter CV obtained for all the simulation conditions for the six networks explored.

Condition	Observed regime	10x10	20x20	40x40	10x10x10	Random	Carbonate
1	Preferential pathways	2.433	3.904	4.732	5.449	3.165	1.081
2	Surface dissolution	0.062	0.136	0.390	0.025	0.049	0.219
3	Uniform dissolution	0.150	0.105	0.093	0.234	0.277	0.705
4	Uniform dissolution	0.001	0.003	0.006	0.001	0.001	0.008

Surface dissolution are identified by the largest values of ΔC . This means that large acid consumption and large spread of the acid throughout the network are observed. Based on the simulation results, the surface dissolution regime is identified by a $\Delta C > 1$.

Table 4.8: Statistical parameter ΔC obtained for all the simulation conditions for the six networks explored.

Condition	Observed regime	10x10	20x20	40x40	10x10x10	Random	Carbonate
1	Preferential pathways	1.66	2.45	5.83	0.56	1.95	0.95
2	Surface dissolution	3.97	12.40	94.60	4.27	6.83	1.65
3	Uniform dissolution	0.08	0.15	0.30	0.08	0.12	0.02
4	Uniform dissolution	0.08	0.14	0.28	0.08	0.12	0.03

The uniform dissolution regime is characterized by the smallest values of CV and ΔC , meaning a system where reactivity is low and acid spreads homogeneously throughout the entire network. Based on the simulation results, the uniform dissolution regime is identified by both $CV < 1$ and $\Delta C < 1$.

4.4 Summary

This study proposes and demonstrates a new pore-network modeling approach to simulate single-phase reactive transport and mineral dissolution in porous media. A new algorithm for the merging of pores and throats resulting from solid dissolution is introduced to guarantee the conservation of the main variables of interest during the merging process. Pore surface areas and throat conductances are modeled accurately using a novel application of correction factors and effective properties.

Our approach solves a coupled transport and reaction pore-network model that implements a kinetic model with a single heterogeneous chemical reaction describing the dissolution of calcite by acidic solutions. The reactive transport problem is described by the acid advection-diffusion transient equation in control volumes represented by pores and throats. The network geometry is updated based on the dissolution process happening at the mineral surface.

Pores and throats are enlarged due to mineral consumption. The merging method is performed when two connected pores reach each other. Pore spaces are relocated in the network and correction factors are updated to conserve the effective surface areas and effective conductance of throats. The fluid flow field is also updated due to these new larger sizes of pores and throats.

A wide range of pore-network models were used to study the reactive transport problem. The main results include the exploration of different dissolution regimes through porosity-permeability evolution curves, acid concentration profiles, and the use of statistical criteria to differentiate regimes. Importantly, this methodology has the ability to simulate permeability increases larger than 100-fold during the formation of preferential pathways through the network. The innovative approaches presented may be used to improve the representation of many subsurface applications where reactive transport and mineral dissolution are the fundamental phenomena at the pore-scale, including performance of acidizing for stimulation, geological storage of carbon dioxide (CO_2), and enhanced oil recovery.

Chapter 5

Conclusions

This thesis presents a pore-network modeling approach to explore reactive transport and mineral dissolution in porous media. The methodology presented here made possible the investigation of the occurrence of different dissolution regimes in a porous medium subject to various flow and reactivity conditions during single-phase flow using a simplified ball-and-stick pore-network model.

The transport problem considers pores and throats as moving control volumes that evolves as a function of the mineral consumption due to heterogeneous chemical reactions between the acid fluid and the reactive mineral walls. The fluid flow field is also updated due to these new larger sizes of pores and throats.

One of the main contributions of this work is the new algorithm for the merging of pores and throats that aims to guarantee the conservation of the main variables of interest during the merging process. Here, we introduce the novel use of correction factors and effective properties, that aims to conserve throat conductances and surface areas of pores and throats while the topology of the network evolves.

The merging method is performed when two connected pores reach each other and also when a throat diameter reaches the same value of the diameter of a connected pore. Then, pore spaces are relocated in the network and correction factors are updated to conserve the effective surface areas and effective conductance of throats.

The main dissolution regimes were mapped in behavior diagrams based on

dimensionless numbers and were explored in simple regular networks and, after the implementation of the new merging methodology, in a wide range of network heterogeneity.

The methodology developed here showed to be applicable to investigate the main dissolution regimes. The main results include the exploration of different dissolution regimes through porosity-permeability evolution curves, acid concentration profiles, and the use of statistical criteria to differentiate regimes. Importantly, this methodology has the ability to simulate permeability increases larger than 100-fold during the formation of preferential pathways through the network

Statistical parameters are introduced here as quantitative criteria to classify dissolution regimes based on the acid concentration profile within the network at the end of simulation. In this way, it is possible to identify standard dissolution patterns based on parameters obtained at the end of simulation, without depending on post-processing and qualitative analysis.

The unique contribution of this study to the literature is to present a pore-network methodology to study single-phase reactive transport and mineral dissolution that is able to explore wide ranges of reactivity and flow conditions. This methodology is not limited to a fixed topology or the simplified ball-and-stick geometry of the porous medium. Also, the use of statistical quantitative criteria brings a simple and more accurate way to identify the main dissolution regimes without only relying on qualitative criteria.

5.1 Future Work

Here, some suggestions for future work are given that could use the novel ideas and tools developed.

- Improvements to the ability of the new merging methodology.

During geometry and topology evolution due to dissolution many different conditions happens. Our algorithm contemplates some of them, but there is still space for improvements.

For example, after merging, the new merged pore is relocated in the network. Sometimes, an overlap of pore spaces happens due to the new position of the merged pore. This situation was named sequential mergings. During sequential mergings, throat conductances are lost and can generate small discrepancies in the evolution of the overall conductance of the network. This behavior could be more thoroughly explored to avoid these differences.

Another example is that our algorithm is designed to process one merging per time step, and sequential mergings as necessary. It would be interesting to handle mergings that involve a cluster of pore spaces, for example, three connected pores that in the same time step reach the merging criteria.

- Coupling with geochemistry modules.

Our approach implements a simplified kinetic model with a single heterogeneous chemical reaction describing the dissolution of calcite by acidic solutions. The coupling of our methodology and a geochemistry module, such as PHREEQC [81] and Reaktoro [82], enables the study of the complex geochemistry system involved in the injection of acidic solution in carbonate rocks.

- Coupling with large-scale simulators.

The coupling of the pore-network model with large scale simulators increases the representativeness of the input data that the pore-scale model can provide. For example, permeability versus porosity curves can be determined by pore-scale models and used as input for larger scale simulators.

- Implementation of the presence of an immobile or mobile gas phase.

CO_2 is not always dissolved in the fluid phase. A system with large reactivity might lead to the formation of a CO_2 gas phase due to the large amount

of reaction product produced. Including the formation of a gas phase considering thermodynamic equilibrium between phases is suggested as future work.

References

- [1] SOHRABI, M., KECHUT, N. I., RIAZI, M., et al. "Coreflooding Studies to Investigate the Potential of Carbonated Water Injection as an Injection Strategy for Improved Oil Recovery and CO₂ Storage", *Transport in Porous Media*, v. 91, n. 1, pp. 101–121, 2012. doi: 10.1007/s11242-011-9835-5.
- [2] WOLTERBEEK, T. K., RAOOF, A. "Meter-Scale Reactive Transport Modeling of CO₂-Rich Fluid Flow along Debonded Wellbore Casing-Cement Interfaces", *Environmental Science and Technology*, v. 52, n. 6, pp. 3786–3795, 2018. doi: 10.1021/acs.est.7b05358.
- [3] MENKE, H. P., REYNOLDS, C. A., ANDREW, M. G., et al. "4D multi-scale imaging of reactive flow in carbonates: Assessing the impact of heterogeneity on dissolution regimes using streamlines at multiple length scales", *Chemical Geology*, v. 481, n. January, pp. 27–37, 2018. doi: 10.1016/j.chemgeo.2018.01.016.
- [4] GHARBI, O., BIJELJIC, B., BOEK, E., et al. "Changes in pore structure and connectivity induced by CO₂ injection in carbonates: A combined pore-scale approach", *Energy Procedia*, v. 37, n. 0, pp. 5367–5378, 2013. doi: 10.1016/j.egypro.2013.06.455.
- [5] ALGIVE, L., BEKRI, S., VIZIKA, O. "Pore-Network Modeling Dedicated to the Determination of the Petrophysical-Property Changes in the Presence of Reactive Fluid", *SPE Journal*, v. 15, n. 03, pp. 618–633, 2010. doi: 10.2118/124305-PA.
- [6] SOULAINÉ, C., ROMAN, S., KOVSCEK, A., et al. "Mineral dissolution and wormholing from a pore-scale perspective", *Journal of Fluid Mechanics*, v. 827, pp. 457–483, 2017. ISSN: 14697645. doi: 10.1017/jfm.2017.499.
- [7] GOLFIER, F., ZARCONE, C., BAZIN, B., et al. "On the ability of a Darcy-scale model to capture wormhole formation during the dissolution

of a porous medium”, *Journal of Fluid Mechanics*, v. 457, pp. 213–254, 2002. doi: 10.1017/S0022112002007735.

- [8] RATHNAWEERA, T. D., RANJITH, P. G., PERERA, M. S. “Experimental investigation of geochemical and mineralogical effects of CO₂ sequestration on flow characteristics of reservoir rock in deep saline aquifers”, *Scientific Reports*, v. 6, n. September 2015, pp. 1–12, 2016. doi: 10.1038/srep19362.
- [9] BEMER, E., LOMBARD, J. M. “From Injectivity to Integrity Studies of CO₂ Geological Storage”, *Oil and Gas Science and Technology*, v. 65, n. 3, pp. 445–459, 2010. doi: 10.2516/ogst/2009028.
- [10] FREDD, C. N., DOWELL, S. “Advances in Understanding and Predicting Wormhole Formation”. In: *Reservoir Stimulation*, 3 ed., cap. A16, Wiley, 2000.
- [11] EGERMANN, P., BEKRI, S., VIZIKA, O. “An integrated approach to assess the petrophysical properties of rocks altered by rock-fluid interactions (CO₂ Injection)”, *Petrophysics*, v. 51, n. 1, pp. 32–40, 2010.
- [12] OTT, H., OEDAI, S. “Wormhole formation and compact dissolution in single- and two-phase CO₂-brine injections”, *Geophysical Research Letters*, v. 42, n. 7, pp. 2270–2276, 2015. doi: 10.1002/2015GL063582.
- [13] HILL, A. D., SCHECHTER, R. S. “Fundamentals of Acid Stimulation”. In: Economides, M. J., Nolte, K. G. (Eds.), *Reservoir Stimulation*, 3 ed., cap. 16, Wiley, 2000.
- [14] FREDD, C. N., FOGLER, H. “Optimum Conditions for Wormhole Formation in Carbonate Porous Media: Influence of Transport and Reaction”, *SPE Journal*, v. 4, n. 03, 1999. doi: 10.2118/56995-PA.
- [15] STEEFEL, C. I., MÄHER, K. “Fluid-rock interaction: A reactive transport approach”, *Reviews in Mineralogy and Geochemistry*, v. 70, n. 1988, pp. 485–532, 2009. doi: 10.2138/rmg.2009.70.11.
- [16] BÉKRI, S., THOVERT, J. F., ADLER, P. M. “Dissolution of porous media”, *Chemical Engineering Science*, v. 50, n. 17, pp. 2765–2791, 1995. doi: 10.1016/0009-2509(95)00121-K.
- [17] DACCORD, G., LIÉTARD, O., LENORMAND, R. “Chemical dissolution of a porous medium by a reactive fluid-II. Convection vs reaction,

- behavior diagram”, *Chemical Engineering Science*, v. 48, n. 1, pp. 179–186, 1993. doi: 10.1016/0009-2509(93)80294-Z.
- [18] LIU, M., MOSTAGHIMI, P. “Characterisation of reactive transport in pore-scale correlated porous media”, *Chemical Engineering Science*, v. 173, pp. 121–130, 2017. doi: 10.1016/j.ces.2017.06.044.
- [19] SONG, W., OGUNBANWO, F., STEINSBØ, M., et al. “Mechanisms of multiphase reactive flow using biogenically calcite-functionalized micromodels”, *Lab on a Chip*, v. 18, n. 24, pp. 3881–3891, 2018. doi: 10.1039/C8LC00793D.
- [20] OLIVEIRA, T. D., BLUNT, M. J., BIJELJIC, B. “Modelling of multi-species reactive transport on pore-space images”, *Advances in Water Resources*, v. 127, n. August 2018, pp. 192–208, 2019. doi: 10.1016/j.advwatres.2019.03.012.
- [21] TARTAKOVSKY, A. M., TRASK, N., PAN, K., et al. “Smoothed particle hydrodynamics and its applications for multiphase flow and reactive transport in porous media”, *Computational Geosciences*, v. 20, n. 4, pp. 807–834, 2016. doi: 10.1007/s10596-015-9468-9.
- [22] FATT, I. “The Network Model of Porous Media”, *Petroleum Transactions, AIME*, v. 207, pp. 144–181, 1956.
- [23] LI, L., PETERS, C. A., CELIA, M. A. “Upscaling geochemical reaction rates using pore-scale network modeling”, *Advances in Water Resources*, v. 29, n. 9, pp. 1351–1370, 2006. doi: 10.1016/j.advwatres.2005.10.011.
- [24] RAOOF, A., NICK, H. M., WOLTERBEEK, T. K., et al. “Pore-scale modeling of reactive transport in wellbore cement under CO₂ storage conditions”, *International Journal of Greenhouse Gas Control*, v. 11, n. SUPPL, pp. 67–77, 2012. doi: 10.1016/j.ijggc.2012.09.012.
- [25] TANSEY, J., BALHOFF, M. T. “Pore Network Modeling of Reactive Transport and Dissolution in Porous Media”, *Transport in Porous Media*, v. 113, n. 2, pp. 303–327, 2016. doi: 10.1007/s11242-016-0695-x.
- [26] MEHMANI, Y., BALHOFF, M. T. “Mesoscale and Hybrid Models of Fluid Flow and Solute Transport”, *Reviews in Mineralogy and Geochemistry*, v. 80, n. 1, pp. 433–459, 2015. doi: 10.2138/rmg.2015.80.13.

- [27] YANG, X., MEHMANI, Y., PERKINS, W. A., et al. “Intercomparison of 3D pore-scale flow and solute transport simulation methods”, *Advances in Water Resources*, v. 95, pp. 176–189, 2016. doi: 10.1016/j.advwatres.2015.09.015.
- [28] RAOOF, A. *Reactive/Adsorptive Transport in (Partially-) Saturated Porous Media*. PhD Thesis, Utrecht University, 2011.
- [29] ESTEVES, B. F., LAGE, P. L., COUTO, P., et al. “Pore-network modeling of single-phase reactive transport and dissolution pattern evaluation”, *Advances in Water Resources*, v. 145, pp. 103741, 2020. doi: 10.1016/j.advwatres.2020.103741.
- [30] IEA - INTERNATIONAL ENERGY AGENCY. “World Energy Outlook 2018: Highlights”, *International Energy Agency*, 2018.
- [31] IEA. “EIA Energy Outlook 2020”, *International Energy Agency*, 2020.
- [32] FASSIHI, M. R., KOVSCEK, A. R. *Low Energy Processes for Unconventional Oil Recovery*. Monograph Series Society of Petroleum Engineers, 2017.
- [33] GUNTER, W. D., BACHU, S., BENSON, S. “The role of hydrogeological and geochemical trapping in sedimentary basins for secure geological storage of carbon dioxide”, *Geological Society Special Publication*, v. 233, pp. 129–145, 2004. doi: 10.1144/GSL.SP.2004.233.01.09.
- [34] FREDD, C. N., FOGLER, H. “Influence of transport and reaction on wormhole formation in porous media”, *AIChE Journal*, v. 44, n. 9, pp. 1933–1949, 1998. doi: 10.1002/aic.690440902.
- [35] KANG, Q., CHEN, L., VALOCCHI, A. J., et al. “Pore-scale study of dissolution-induced changes in permeability and porosity of porous media”, *Journal of Hydrology*, v. 517, pp. 1049–1055, 2014. doi: 10.1016/j.jhydrol.2014.06.045.
- [36] BHAT, S. K., KOVSCEK, A. R. “Permeability modification of diatomite during hot fluid injection”, *Proceedings - SPE Annual Western Regional Meeting*, 1998. doi: 10.2118/0998-0098-jpt.
- [37] ALGIVE, L., BEKRI, S., ROBIN, M., et al. “Reactive Transport: Experiments and Pore-Network Modelling”, *International Symposium of the Society of Core Analysts*, , n. 1969, pp. 1–13, 2007.

- [38] VARLOTEAUX, C., BÉKRI, S., ADLER, P. M. “Pore network modelling to determine the transport properties in presence of a reactive fluid: From pore to reservoir scale”, *Advances in Water Resources*, v. 53, pp. 87–100, 2013. doi: 10.1016/j.advwatres.2012.10.004.
- [39] BEKRI, S., RENARD, S., DELPRAT-JANNAUD, F. “Pore to Core Scale Simulation of the Mass Transfer with Mineral Reaction in Porous Media”, *Oil & Gas Science and Technology – Revue d’IFP Energies nouvelles*, v. 70, n. 4, pp. 681–693, 2015. doi: 10.2516/ogst/2014046.
- [40] MEAKIN, P., TARTAKOVSKY, A. M. “Modeling and simulation of pore-scale multiphase fluid flow and reactive transport in fractured and porous media”, *Reviews of Geophysics*, v. 47, n. 3, pp. 1–47, 2009. doi: 10.1029/2008RG000263.
- [41] XIONG, Q., BAYCHEV, T. G., JIVKOV, A. P. “Review of pore network modelling of porous media: Experimental characterisations, network constructions and applications to reactive transport”, *Journal of Contaminant Hydrology*, v. 192, pp. 101–117, 2016. doi: 10.1016/j.jconhyd.2016.07.002.
- [42] OOSTROM, M., MEHMANI, Y., ROMERO-GOMEZ, P., et al. “Pore-scale and continuum simulations of solute transport micromodel benchmark experiments”, *Computational Geosciences*, v. 20, n. 4, pp. 857–879, 2016. doi: 10.1007/s10596-014-9424-0.
- [43] TARTAKOVSKY, A. M., MEAKIN, P., SCHEIBE, T. D., et al. “Simulations of reactive transport and precipitation with smoothed particle hydrodynamics”, *Journal of Computational Physics*, v. 222, n. 2, pp. 654–672, 2007. doi: 10.1016/j.jcp.2006.08.013.
- [44] KOVSCEK, A. R., WONG, H., RADKE, C. J. “A pore-level scenario for the development of mixed wettability in oil reservoirs”, *AIChE Journal*, v. 39, pp. 1072–1085, 1993. doi: 10.1002/aic.690390616.
- [45] BLUNT, M. J. “Flow in porous media - pore-network models and multiphase flow”, *Current Opinion in Colloid & Interface Science*, v. 6, n. 3, pp. 197–207, 2001.
- [46] GHARBI, O., BLUNT, M. J. “The impact of wettability and connectivity on relative permeability in carbonates: A pore network modeling analysis”, *Water Resources Research*, v. 48, n. 12, pp. 1–14, 2012. doi: 10.1029/2012WR011877.

- [47] GÜNDOĞAR, S. A. *Multiscale pore structure characterization and pore network modeling of Middle East carbonates*. PhD Thesis, Middle East Technical University, 2017.
- [48] FENWICK, D. H., BLUNT, M. J. “Three-dimensional modeling of three phase imbibition and drainage”, *Advances in Water Resources*, v. 21, pp. 121–143, 1998. doi: 10.1016/S0309-1708(96)00037-1.
- [49] HUI, M. H., BLUNT, M. J. “Effects of wettability on three-phase flow in porous media”, *Journal of Physical Chemistry B*, v. 104, pp. 3833–3845, 2000. doi: 10.1021/jp9933222.
- [50] PEÇANHA, A. S. R. *Simulation of Multiphase Flow in Porous Media (in portuguese)*. PhD Thesis, Universidade Federal do Rio de Janeiro, 2014.
- [51] QIN, C. Z., HASSANIZADEH, S. M. “Pore-Network Modeling of Solute Transport and Biofilm Growth in Porous Media”, *Transport in Porous Media*, v. 110, n. 3, pp. 345–367, 2015. doi: 10.1007/s11242-015-0546-1.
- [52] RAOOF, A., HASSANIZADEH, S. M., LEIJNSE, A. “Upscaling Transport of Adsorbing Solutes in Porous Media: Pore-Network Modeling”, *Vadose Zone Journal*, v. 9, n. 3, pp. 624, 2010. doi: 10.2136/vzj2010.0026.
- [53] FAZELI, M., HINEBAUGH, J., BAZYLAK, A. “Incorporating Embedded Microporous Layers into Topologically Equivalent Pore Network Models for Oxygen Diffusivity Calculations in Polymer Electrolyte Membrane Fuel Cell Gas Diffusion Layers”, *Electrochimica Acta*, v. 216, pp. 364–375, 2016. doi: 10.1016/j.electacta.2016.08.126.
- [54] AGHIGHI, M., GOSTICK, J. “Pore network modeling of phase change in PEM fuel cell fibrous cathode”, *Journal of Applied Electrochemistry*, v. 47, pp. 1323–1338, 2017. doi: 10.1007/s10800-017-1126-6.
- [55] BLUNT, M. J., BIJELJIC, B., DONG, H., et al. “Pore-scale imaging and modelling”, *Advances in Water Resources*, v. 51, pp. 197–216, 2013. doi: 10.1016/j.advwatres.2012.03.003.
- [56] ØREN, P. E., BAKKE, S., ARNTZEN, O. J. “Extending Predictive Capabilities to Network Models”, *SPE Journal*, v. 3, pp. 324–335, 1998. ISSN: 1086055X. doi: 10.2118/52052-pa.
- [57] VALVATNE, P. H., BLUNT, M. J. “Predictive pore-scale modeling of two-phase flow in mixed wet media”, *Water Resources Research*, v. 40, pp. 1–21, 2004. doi: 10.1029/2003WR002627.

- [58] BLUNT, M. J., JACKSON, M. D., PIRI, M., et al. "Detailed physics , predictive capabilities and upscaling for pore-scale models of multiphase flow", *Advances in Water Resources*, v. 25, pp. 1069–1089, 2001.
- [59] KIM, D., LINDQUIST, W. B. "Effects of network dissolution changes on pore-to-core upscaled reaction rates for kaolinite and anorthite reactions under acidic conditions", *Water Resources Research*, v. 49, n. 11, pp. 7575–7586, 2013. doi: 10.1002/2013WR013667.
- [60] LINDQUIST, W. B., LEE, S. M., COKER, D. A., et al. "Medial axis analysis of void structure in three-dimensional tomographic images of porous media", *Journal of Geophysical Research B: Solid Earth*, v. 101, pp. 8297–8310, 1996. doi: 10.1029/95jb03039.
- [61] SILIN, D., PATZEK, T. "Robust Determination of the Pore-Space Morphology in Sedimentary Rocks", *Annual Technical Conference and Exhibition*, 2003. doi: 10.2523/84296-MS.
- [62] AL-KHARUSI, A. S., BLUNT, M. J. "Network extraction from sandstone and carbonate pore space images", *Journal of Petroleum Science and Engineering*, v. 56, pp. 219–231, 2007. doi: 10.1016/j.petrol.2006.09.003.
- [63] GOSTICK, J. T. "Versatile and efficient pore network extraction method using marker-based watershed segmentation", *Physical Review E*, v. 96, pp. 1–15, 2017. doi: 10.1103/PhysRevE.96.023307.
- [64] HOEFNER, M. L., FOGLER, H. S. "Pore evolution and channel formation during flow and reaction in porous media", *AIChE Journal*, v. 34, n. 1, pp. 45–54, 1988. doi: 10.1002/aic.690340107.
- [65] BUDEK, A., SZYMCZAK, P. "Network models of dissolution of porous media", *Physical Review E - Statistical, Nonlinear, and Soft Matter Physics*, v. 86, n. 5, pp. 1–16, 2012. doi: 10.1103/PhysRevE.86.056318.
- [66] LI, L., PETERS, C. A., CELIA, M. A. "Effects of mineral spatial distribution on reaction rates in porous media", *Water Resources Research*, v. 43, n. 1, pp. 1–17, 2007. doi: 10.1029/2005WR004848.
- [67] KIM, D., PETERS, C. A., LINDQUIST, W. B. "Upscaling geochemical reaction rates accompanying acidic CO₂-saturated brine flow in sandstone aquifers", *Water Resources Research*, v. 47, pp. 1–16, 2011. doi: 10.1029/2010WR009472.

- [68] NOGUES, J. P., FITTS, J. P., CELIA, M. A., et al. “Permeability evolution due to dissolution and precipitation of carbonates using reactive transport modeling in pore networks”, *Water Resources Research*, v. 49, n. 9, pp. 6006–6021, 2013. doi: 10.1002/wrcr.20486.
- [69] RAOOF, A., NICK, H. M., HASSANIZADEH, S. M., et al. “PoreFlow: A complex pore-network model for simulation of reactive transport in variably saturated porous media”, *Computers and Geosciences*, v. 61, pp. 160–174, 2013. doi: 10.1016/j.cageo.2013.08.005.
- [70] REGNIER, P., O’KANE, J., STEEFEL, C., et al. “Modeling complex multi-component reactive-transport systems: towards a simulation environment based on the concept of a Knowledge Base”, *Applied Mathematical Modelling*, v. 26, pp. 913–927, 2002. doi: 10.1016/S0307-904X(02)00047-1.
- [71] RAOOF, A., MAJID HASSANIZADEH, S. “A new method for generating pore-network models of porous media”, *Transport in Porous Media*, v. 81, pp. 391–407, 2010. doi: 10.1007/s11242-009-9412-3.
- [72] DASHTIAN, H., BAKHSHIAN, S., HAJIREZAIE, S., et al. “Convection-diffusion-reaction of CO₂-enriched brine in porous media: A pore-scale study”, *Computers and Geosciences*, v. 125, pp. 19–29, 2019. doi: 10.1016/j.cageo.2019.01.009.
- [73] LONDON, I. C. “Imperial College London. PERM - Petroleum Engineering & Rock Mechanics Group. Pore-Scale Modelling and Imaging.” 2020. Accessed: 2020-04-13.
- [74] GOSTICK, J., AGHIGHI, M., HINEBAUGH, J., et al. “OpenPNM: A Pore Network Modeling Package”, *Computing in Science Engineering*, v. 18, n. 4, pp. 60–74, July 2016.
- [75] BIRD, R., STEWARD, W., LIGHTFOOT, E. *Fenomenos de Transporte*. Rio de Janeiro, LTC, 2011.
- [76] JONES, E., OLIPHANT, T., PETERSON, P., et al. “SciPy: Open source scientific tools for Python”. 2001–. Available at: <<http://www.scipy.org/>>. Accessed: 2020-05-05.
- [77] SONG, W., DE HAAS, T. W., FADAEI, H., et al. “Chip-off-the-old-rock: The study of reservoir-relevant geological processes with real-rock micromodels”, *Lab on a Chip*, v. 14, n. 22, pp. 4382–4390, 2014. doi: 10.1039/c4lc00608a.

- [78] DACCORD, G., LENORMAND, R., LIÉTARD, O. "Chemical dissolution of a porous medium by a reactive fluid-I. Model for the "wormholing" phenomenon", *Nature*, v. 325, pp. 41–43, 1987. doi: 10.1038/325041a0.
- [79] DACCORD, G., LENORMAND, R., LIÉTARD, O. "Chemical dissolution of a porous medium by a reactive fluid-I. Model for the "wormholing" phenomenon", *Chemical Engineering Science*, v. 48, n. 1, pp. 169–178, 1993. doi: 10.1016/0009-2509(93)80293-Y.
- [80] HEUMANN, C., SCHOMAKER, M. *Introduction to Statistics and Data Analysis*. Switzerland, Springer, 2016. doi: 10.1007/978-3-319-46162-5.
- [81] PARKHURST, D. L., APPELO, C. "Description of Input and Examples for PHREEQC Version 3 — A Computer Program for Speciation , Batch-Reaction , One-Dimensional Transport , and Inverse Geochemical Calculations", *U.S. Geological Survey Techniques and Methods, book 6, chapter A43*, 2013.
- [82] LEAL, A. "Reaktoro". 2021. Available at: <https://github.com/reaktoro/reaktoro>. Accessed: 2021-02-07.
- [83] HAUKE, G. *An Introduction to Fluid Mechanics and Transport Phenomena*. Zaragoza, Springer, 2008.

Appendix A

Mass balance derivations

The reactive transport and dissolution problem is described by the mass balance in all available pore spaces, pores, and throats, and is deduced from the mass conservation equations of the chemical species [75]. Here, derivation of the mass balance equation for pores and throats are described.

A.1 Mass balance for pores

Reactive flow processes are described by the continuity equation for a multi-component mixture, as

$$\frac{\partial C_\alpha}{\partial t} + \nabla \cdot (C_\alpha \mathbf{v}) = -\nabla \cdot (\mathbf{J}_\alpha) + s_\alpha \quad (\text{A.1})$$

where C_α is the mass concentration of specie α , t is the time, \mathbf{v} is the average mass velocity of the mixture, \mathbf{J}_α is the mass diffusive flux and s_α is the source term [75].

Volume integration of Eq. (A.1) results in

$$\int_{V_{(t)}} \frac{\partial C_\alpha}{\partial t} dV + \int_{V_{(t)}} \nabla \cdot (C_\alpha \mathbf{v} + \mathbf{J}_\alpha) dV = \int_{V_{(t)}} s_\alpha dV \quad (\text{A.2})$$

where $V_{(t)}$ is the control volume at instant t .

The dissolution process is characterized by the expansion of the control vol-

ume. That means that the control volume is variable with time. Theorem 5.1 from [83] describes this phenomenon considering an arbitrary volume $V_{(t)}$ with boundary $A_{(t)}$ that moves at the velocity \mathbf{v}_c and has $\hat{\mathbf{n}}$ as an exterior normal to the boundary, as

$$\frac{d}{dt} \int_{V_{(t)}} C_\alpha dV = \int_{V_{(t)}} \frac{\partial C_\alpha}{\partial t} dV + \int_{A_{(t)}} C_\alpha \mathbf{v}_c \cdot \hat{\mathbf{n}} dA. \quad (\text{A.3})$$

The Gauss divergence theorem is used to relate the outward flux through a closed surface to the integral of the volume of this surface, as follows

$$\int_{V_{(t)}} \nabla \cdot (C_\alpha \mathbf{v} + \mathbf{J}_\alpha) dV = \int_{A_{(t)}} (C_\alpha \mathbf{v} + \mathbf{J}_\alpha) \cdot \hat{\mathbf{n}} dA. \quad (\text{A.4})$$

Substituting Eqs. (A.3) and (A.4) into Eq. (A.1), the following equation is obtained

$$\frac{d}{dt}(C_\alpha V) - \int_{A_{(t)}} C_\alpha \mathbf{v}_c \cdot \hat{\mathbf{n}} dA + \int_{A_{(t)}} (C_\alpha \mathbf{v} + \mathbf{J}_\alpha) \cdot \hat{\mathbf{n}} dA = S_\alpha. \quad (\text{A.5})$$

The control volume is divided in three regions: inlet and outlet zones (A_{in} and A_{out}), and the reactive surface area (A_r), where heterogeneous chemical reactions occur. The union of these three regions represents all control volume surfaces, as

$$A_{(t)} = A_{in} \cup A_{out} \cup A_r. \quad (\text{A.6})$$

The substitution of Eq. (A.6) into Eq. (A.5) results in

$$\begin{aligned} \frac{d}{dt}(C_\alpha V) + \int_{A_{in}} [C_\alpha(\mathbf{v} - \mathbf{v}_c) + \mathbf{J}_\alpha] \cdot \hat{\mathbf{n}} dA + \int_{A_{out}} [C_\alpha(\mathbf{v} - \mathbf{v}_c) + \mathbf{J}_\alpha] \cdot \hat{\mathbf{n}} dA \\ + \int_{A_r} [C_\alpha(\mathbf{v} - \mathbf{v}_c) + \mathbf{J}_\alpha] \cdot \hat{\mathbf{n}} dA = S_\alpha, \end{aligned} \quad (\text{A.7})$$

that represents the base equation for reactive transport in multidimensional systems.

For pores, with spherical geometry and with a homogeneous concentration inside the control volume, the advective terms at inlet and outlet zones take into account advective mass inflow rates, represented by the mass that arrives in pore i from connected throats ij , and advective mass outflow rate, represented by the mass that leaves pore i through throats ij , as presented below

$$\int_{A_{in} \cup A_{out}} [C_\alpha (\mathbf{v} - \mathbf{v}_c) \cdot \hat{\mathbf{n}}] dA \cong - \left(+ \sum_{ij, in} C_{\alpha, ij} q_{ij} - C_{\alpha, i} \sum_{ij, out} q_{ij} \right) \quad (\text{A.8})$$

where $C_{\alpha, ij}$ is the mass concentration of species α that arrives into pore i by throat ij that has q_{ji} as the volumetric flow rate, $C_{\alpha, i}$ is the mass concentration of species α that leaves pore i by throat ij .

The rate of change of mass due to diffusion between pore i and all connected throats ij through inlet and outlet zones is represented by Fick's Law, as follows

$$\mathbf{J}_\alpha = -\mathcal{D}_\alpha \nabla C_\alpha \rightarrow \mathbf{J}_\alpha \cdot \hat{\mathbf{n}} = -\mathcal{D}_\alpha (\hat{\mathbf{n}} \cdot \nabla C_\alpha) \cong -\mathcal{D}_\alpha \left(\frac{C_{\alpha, ij} - C_{\alpha, i}}{0.5l_{ij} + r_i} \right), \quad (\text{A.9})$$

$$\int_{A_{in} \cup A_{out}} \mathbf{J}_\alpha \cdot \hat{\mathbf{n}} dA \cong - \sum_{ij} A_{ij} \mathcal{D}_{\alpha, ij} \left(\frac{C_{\alpha, ij} - C_{\alpha, i}}{0.5l_{ij} + r_i} \right), \quad (\text{A.10})$$

where \mathcal{D}_α is the diffusion coefficient of species α , $C_{\alpha, ij}$ is the mass concentration of species α in throat ij connected to pore i , l_{ij} is the length of throat ij , and A_{ij} is the cross-section area of throat ij .

The mass change through the pore reactive surface area is due to heterogeneous chemical reaction that occurs in the available reactive surface area of pore i , as follows

$$\int_{A_r} [C_\alpha (\mathbf{v} - \mathbf{v}_c) + \mathbf{J}_\alpha] \cdot \hat{\mathbf{n}} dA \cong R_{\alpha, i} A_{r, i} = C_{\alpha, i} k_r A_{r, i}, \quad (\text{A.11})$$

where $R_{\alpha,i}$ is the heterogeneous chemical reaction rate of species α , assuming a first order reaction, $A_{r,i}$ is the reactive surface area of pore i , and k_r is the linear reaction rate coefficient.

The source term is zero in our approach because we are not considering any homogeneous chemical reactions in our system. Finally, substituting Eqs. (A.8), (A.10) and (A.11) into Eq. (A.7), the reactive transport equation for pore i is

$$\frac{d}{dt}(C_{\alpha,i}V_i) = \sum_{ij,in} C_{\alpha,ij} q_{ij} - C_{\alpha,i} \sum_{ij,out} q_{ij} + \sum_{ij} A_{ij} \mathcal{D}_\alpha \left(\frac{C_{\alpha,ij} - C_{\alpha,i}}{0.5l_{ij} + r_i} \right) - R_{\alpha,i} A_{r,i}. \quad (\text{A.12})$$

A.2 Mass balance for throats

Considering Eq. (A.7), mass change due to advection between the inlet and at outlet zones of throat ij is described by the mass of chemical species α that arrives in throat ij from the connected pore i and by the mass of α that leaves throat ij in the direction of pore j , $C_{\alpha,i}$ and $C_{\alpha,ij}$, respectively, as follows

$$\int_{A_{in} \cup A_{out}} [C_\alpha (\mathbf{v} - \mathbf{v}_c) \cdot \hat{\mathbf{n}}] dA \cong - [(C_{\alpha,i} - C_{\alpha,ij}) q_{ij}]. \quad (\text{A.13})$$

The mass change due to diffusive transport is represented by considering Fick's Law and the concentration difference between throat ij and the two connected pores i and j , as follows

$$\int_{A_{in} \cup A_{out}} \mathbf{J}_\alpha \cdot \hat{\mathbf{n}} dA \cong - \left[+A_{ij} \mathcal{D}_\alpha \left(\frac{C_{\alpha,i} - C_{\alpha,ij}}{0.5l_{ij} + r_i} \right) + A_{ij} \mathcal{D}_\alpha \left(\frac{C_{\alpha,j} - C_{\alpha,ij}}{0.5l_{ij} + r_j} \right) \right]. \quad (\text{A.14})$$

Transport through the available reactive surface is represented by heterogeneous chemical reactions between species α and the reactive mineral present in the surface wall, as

$$\int_{A_r} [C_\alpha(\mathbf{v} - \mathbf{v}_c) + \mathbf{J}_\alpha] \cdot \hat{\mathbf{n}} dA \cong R_{\alpha,ij} A_{r,ij} = C_{\alpha,ij} k_r A_{r,ij}, \quad (\text{A.15})$$

where $R_{\alpha,ij}$ is the heterogeneous chemical reaction rate of specie α and $A_{r,ij}$ is the reactive surface area of throat ij . The source term is described by the homogeneous chemical reactions of specie α . We are not considering any homogeneous chemical reactions in our system, in this way, this term is equal to zero in our approach.

Finally, the mass balance equation for species α in throat ij is

$$\begin{aligned} \frac{d}{dt}(C_{\alpha,ij} V_{ij}) = (C_{\alpha,i} - C_{\alpha,ij}) q_{ij} + A_{ij} \mathcal{D}_\alpha \left(\frac{C_{\alpha,i} - C_{\alpha,ij}}{0.5l_{ij} + r_i} \right) + A_{ij} \mathcal{D}_\alpha \left(\frac{C_{\alpha,j} - C_{\alpha,ij}}{0.5l_{ij} + r_j} \right) \\ - R_{\alpha,ij} A_{r,ij} \end{aligned} \quad (\text{A.16})$$

Appendix B

Mass balance errors

The mass balance errors are estimated based on the relative difference between the accumulation term and the sum of the terms related to inlet, outlet, and consumption of mass of acid at each time step for the entire simulation, as described below

$$MB_{error} = \frac{accumulation - (inlet - outlet - consumption)}{accumulation} \quad (B.1)$$

Table B.1 presents the mass balance errors for the four simulation conditions explored using the three pore-network models explored in this study. The error is present in percentage.

Table B.1: Mass balance error (%) obtained in the simulations.

Network	Condition 1	Condition 2	Condition 3	Condition 4
10x10	0.0003	0.0003	0.0012	0.0013
20x20	0.0008	0.0010	0.0015	0.0016
40x40	0.0065	0.0083	0.0058	0.0062
10x10x10	0.0023	0.0019	0.0058	0.0060
Random	0.0014	0.0014	0.0038	0.0038
Carbonate	0.0007	0.0005	0.0148	0.0082

Tables B.2 and B.3 present, respectively, the time-step sizes and number of time steps used in the simulations.

Table B.2: Time-step sizes (in seconds) used in the simulations.

Network	Condition 1	Condition 2	Condition 3	Condition 4
10x10	1.0×10^{-4}	1.0×10^{-4}	2.0×10^{-4}	2.0×10^{-4}
20x20	2.0×10^{-4}	2.0×10^{-4}	5.0×10^{-4}	5.0×10^{-4}
40x40	2.0×10^{-4}	2.0×10^{-4}	5.0×10^{-4}	5.0×10^{-4}
10x10x10	1.0×10^{-4}	1.0×10^{-4}	4.0×10^{-4}	4.0×10^{-4}
Random	1.0×10^{-4}	1.0×10^{-4}	3.0×10^{-4}	3.0×10^{-4}
Carbonate	1.0×10^{-6}	1.0×10^{-6}	1.5×10^{-5}	1.5×10^{-5}

Table B.3: Number of time steps used in the simulations.

Network	Condition 1	Condition 2	Condition 3	Condition 4
10x10	$1.5 \times 10^{+4}$	$1.5 \times 10^{+4}$	$9.0 \times 10^{+4}$	$1.8 \times 10^{+5}$
20x20	$1.0 \times 10^{+4}$	$1.0 \times 10^{+4}$	$4.0 \times 10^{+4}$	$4.0 \times 10^{+4}$
40x40	$2.1 \times 10^{+4}$	$2.1 \times 10^{+4}$	$4.0 \times 10^{+4}$	$4.0 \times 10^{+4}$
10x10x10	$1.5 \times 10^{+4}$	$1.5 \times 10^{+4}$	$3.5 \times 10^{+4}$	$3.5 \times 10^{+4}$
Random	$1.0 \times 10^{+4}$	$1.0 \times 10^{+4}$	$3.0 \times 10^{+4}$	$3.0 \times 10^{+4}$
Carbonate	$4.0 \times 10^{+4}$	$3.0 \times 10^{+4}$	$4.0 \times 10^{+4}$	$4.0 \times 10^{+4}$